Argonne NATIONAL LABORATORY

ANL-GenIV-071

Prioritization of VHTR System Modeling Needs Based on Phenomena Identification, Ranking and Sensitivity Studies

Nuclear Engineering Division

ANL-GenIV-071

Prioritization of VHTR System Modleing Needs Based on Phenomena Identification, Ranking and Sensitivity Studies

by
R.B. Vilim, W.D. Pointer, T.Y.C. Wei
Nuclear Engineering Division, Argonne National Laboratory

April 2006

work sponsored by

U. S. Department of Energy,
Office of Nuclear Energy, Science and Technology

UChicago ▶ Argonne LLC

Office of Science
U.S. DEPARTMENT OF ENERGY

A U.S. Department of Energy laboratory managed by UChicago Argonne, LLC

About Argonne National Laboratory

Argonne is a U.S. Department of Energy laboratory managed by UChicago Argonne, LLC under contract DE-AC02-06CH11357. The Laboratory's main facility is outside Chicago, at 9700 South Cass Avenue, Argonne, Illinois 60439. For information about Argonne, see www.anl.gov.

Availability of This Report

This report is available, at no cost, at http://www.osti.gov/bridge. It is also available on paper to the U.S. Department of Energy and its contractors, for a processing fee, from:

U.S. Department of Energy
Office of Scientific and Technical Information
P.O. Box 62
Oak Ridge, TN 37831-0062
phone (865) 576-8401
fax (865) 576-5728
reports@adonis.osti.gov

Disclaimer

This report was prepared as an account of work sponsored by an agency of the United States Government. Neither the United States Government nor any agency thereof, nor UChicago Argonne, LLC, nor any of their employees or officers, makes any warranty, express or implied, or assumes any legal liability or responsibility for the accuracy, completeness, or usefulness of any information, apparatus, product, or process disclosed, or represents that its use would not infringe privately owned rights. Reference herein to any specific commercial product, process, or service by trade name, trademark, manufacturer, or otherwise, does not necessarily constitute or imply its endorsement, recommendation, or favoring by the United States Government or any agency thereof. The views and opinions of document authors expressed herein do not necessarily state or reflect those of the United States Government or any agency thereof, Argonne National Laboratory, or UChicago Argonne, LLC.

Acknowledgement

A major debt of gratitude is owed to Dr. Won-Jae Lee of the Korea Atomic Energy Research Institute (KAERI) and his KAERI colleagues for the very productive collaboration on the companion I-NERI project. The insights, results and ideas conveyed through discussions, presentations, and documentation during the course of the companion I-NERI project "Screening of Gas-Cooled Reactor Thermal Hydraulic and Safety Analysis Tools and Experimental Database" has been very beneficial. We convey our thanks in this acknowledgement.

Appreciations are also due to Dick Schultz of INL and Syd Ball of ORNL for the valuable interactions during the course of this project. They are gratefully acknowledged.

Table of Contents

List of Figures

List of Tables

1.0 Introduction

1.1 Objective

Quantification of uncertainty is a key requirement for the design of a nuclear power plant and the assurance of its safety. Historically the procedure has been to perform the required uncertainty assessment through comparison of the analytical predictions with experimental simulations. The issue with this historical approach has always been that the simulations through experiments could not be at full scale for the practical reasons of cost and scheduling. Invariably, only parts of the system were tested separately or if integral testing was performed for the complete system, the size or scale of the experimental apparatus was significantly smaller than the actual plant configuration.

In the U.S. and in the rest of the world, selection of facility scaling was a large topic during the resolution of the ECCS issue for the current fleet of GEN II LWRs in the 1980s. Whether or not the experimental data which was produced by and phenomena which occurred during the tests performed in each facility were representative of those which would actually occur in the operating plants, which typically are of much large size scale, was a subject of much discussion. As a consequence of this effort on LWR ECCS performance and best-estimate code predictions, the USNRC developed a systematic methodology termed Code Scaling, Applicability and Uncertainty (CSAU) methodology, which was to resolve the question of the appropriateness of utilizing scaled-down test facilities to provide the data to assess the uncertainty in the predictions of the best-estimate design and safety tools. Unquestionably, code applicability and the uncertainty evaluation are of equal importance with the issue of scaling. The CSAU methodology therefore is comprised of a number of steps which are summarized here.

1. Specification of the transient scenario and the selection of plant for which the uncertainty assessment is to be performed.
2. Identification of the phenomena which occur during the transient scenario and the ranking of the importance of the phenomena with respect to the primary safety criteria. The Phenomena Identification and Ranking Tables (PIRTs) are the product of this step.
3. Determination of the code applicability for the analysis of the selected scenario by relating the modeling in the code to the modeling requirements specified in the PIRTs.
4. Assessment of the parameter predictions by establishing an assessment matrix of test cases consistent with the finding of the PIRTs, determining the effect of scale and carrying out the comparison of the data from the tests cases with the results from calculations performed with the applicable codes selected in Step (3). This produces the uncertainty assessments of the tools which is the goal of this CSAU process.

These steps can be further detailed but in the main, the major points have been outlined here. The objective of the work in this GEN IV VHTR task is to support the VHTR Design Methods Development and Validation R&D program plan by focusing on

steps (1) and (2) of the CSAU methodology. This would prepare the basis for step (4) where the actual validation calculations with the selected codes are performed and the standard problem/experiments for the assessment are planned and carried out.

Delineation of plant accidents, transient scenarios and steady state conditions is essential to defining the modeling needs for the design and safety tools required for designing the various reactor and plant components and evaluating the safety case. This is Step (1) of the CSAU methodology. Once a duty cycle range has been established, then the phenomena which occur during these scenarios for the different conditions can be identified. Identification of the phenomena will enable the determination of the models necessary to be implemented in the design and safety tools. This is Step (2) of the CSAU methodology. Prioritization of these modeling needs will allow a systematic R&D program planning approach to the development of the tools and the construction of the accompanying experiments. The tools could take the form of 1-D integrated system analysis codes or 3-D Computational Fluid Dynamics codes. It is anticipated that with the continuation of the VHTR/NGNP project into the licensing stage, the work performed here would form the starting basis for the interaction with the NRC licensing process.

This report documents the work performed in FY06 on steps (1) and (2). Chapter 2 provides a description of the generic Pebble Bed Reactor (PBR) and Prismatic Modular Reactor (PMR) designs which were used in this study. The selection of accident sequences for the generation of the PIRTs is discussed in Chapter 3. The appropriate PIRTs are presented in Chapter 4. The sensitivity calculations which were performed to provide input for the prioritizing of the phenomena in the PIRTs are presented in Chapter 5. Conclusions regarding specific model development needs based on the PIRTs and the sensitivity calculations are documented in Chapter 6. The focus is on core flow distribution modeling.

1.2 Scope

The GIF VHTR Computational Methods Validation and Benchmark (CMV) Project Management Board (PMB) is composed of members from all the international partners participating in the GIF VHTR System Research Plan. This PMB is collaborating on coordination of the international effort in this area. Board discussions are underway on assuming the role of the Standards Problem Committee for the VHTR CFD tools. PMB participants could therefore have the responsibility of selecting the set of standard problems/experiments that form the assessment matrix of test cases for the assessment and validation of the tools that will eventually comprise the VHTR design and safety analysis methodology. Furthermore, the VHTR/CMV PMB has decided to review the PIRTs documented by this GEN IV task and its I-NERI companion project with KAERI as a starting step in the international collaboration on the validation of the selected tools. Both the U.S. program and the international program are proceeding, and it may well be that the US VHTR (NGNP) could have elements of an international design. As elements of a design are required to define the envelope of experiments to be performed and models which need to be developed, the scope of the work documented in this report was defined to be broad enough to also include these potential designs.

Since a specific design has not yet been selected for the choice of the US VHTR (NGNP), it was decided early on to focus on a generic plant and reactor design with broadly typical features for Step (1) of the CSAU from both US and International efforts. Both a generic Pebble Bed Reactor (PBR) design and a generic Prismatic Modular Reactor (PMR) design were selected. The generic PBR design selected is a version of the 400 MWt South African PBMR design. The generic PMR design selected is a version of the 600 MWt GT-MHR. Chapter 2 provides a summary description of these two reactor plant design types, and some details are given for some of the more relevant features. These are based on what is available in the open literature and were selected after a literature survey was performed. No proprietary information was made available to the work. The PIRTs that have been generated and documented in this report for the selected transient scenario (event) have been based on these generic designs. Since the PIRTs are at this stage also high-level "generic" PIRTs, this approach should be a consistent one. Where differences between the two designs have affected the PIRTs, these have been duly noted. However it should also be noted, that it has been assumed in this report that the Reactor Cavity Cooling System (RCCS) for the PBR is an air-cooled one and not the water cooled version. Also of significance, it should be recognized that the indirect cycle PMR design has been designated for later consideration as only the direct cycle option has been considered here for both the PMR and the PBR transient scenarios of interest. Prioritization of modeling needs for the thermal-fluid design and safety analysis tools based on these generic design assumptions should be appropriate for this stage of the VHTR R&D plan.

1.3 Background

In the previous year's work, the transient scenarios selected for the PIRT exercise included the two that are considered to be among the most limiting for the safety criteria and are generally considered to be well beyond the off-normal spectrum of events and into the Beyond Design Basis Accident (BDBA) space. These are the High Pressure Conduction Cooling (HPCC) and the Low Pressure Conduction Cooling (LPCC) scenarios. An event sequence that would lead to the HPCC transient scenario is the station blackout with scram event. This is where loss of all electric power occurs but the reactor trips and scram rods are inserted to shutdown the critical nuclear reaction. Similarly, the same sequence type of the blackout but accompanied by a leak or break would lead to LPCC. Core conduction cooling by radiation to the vessel and beyond is the means of decay heat removal for both transient scenarios. The Reactor Cavity Cooling Systems (RCCS) is the ultimate passive heat sink system for this decay heat removal. The HPCC and LPCC are essentially decay heat removal accidents. In addition to the LPCC and HPCC, a Load Change (LC) event was also included as an example of a normal operational transient that should be considered as part of the plant duty cycle and should be part of the capability of the analysis tools. PIRTs were generated in FY05 for these three transient scenarios and were documented in [1.1]. The collaboration between ANL, INL and KAERI on the companion I-NERI project #2004-001-K "Screening of Gas-Cooled Reactor Thermal-Hydraulic and Safety Analysis Tools and Experiment Database" was in part focused also on the generation of consensus high-level PIRTs for these three events. The results reported in [1.1] and the companion I-NERI effort

provided the basis for the consensus PIRTs between the three participating organizations documented in [1.2].

In this year's work, an additional three transient scenarios, were selected for the generation of PIRTs. These are the Water Ingress Accident Intermediate Heat Exchanger (IHX)/Hydrogen plant side upsets and a rod withdrawal Anticipated Transient Without Scram (ATWS). Details of the scenarios can be found in Chapter 3. In essence, the Water Ingress Accident is one that occurs when there is a tube leak or break that occurs in one of the water-cooled heat exchangers utilized in the primary system. This leads to liquid water or steam ingress into the primary system. The IHX/Hydrogen plant side upsets are initiated by malfunctions in the hydrogen plant or the buffer loop and associated IHXs. This could lead to imbalances in the heat removal rate or perhaps even secondary coolant inventory entering into the primary system. The rod withdrawal ATWS results from the occurrence of a malfunction in the control rod drive systems or the integrated plant control system that leads to the inadvertent withdrawal of a control rod from the reactor core. This results in positive reactivity insertion, a transient overpower and normally a reactor trip with scram by the plant protection system (PPS). However in the case of an ATWS, a further system malfunction is assumed wherein the PPS fails to scram the shutdown rods, and the reactor remains critical. Chapter 4 details the identification of these transient scenario phenomena and the ranking process for the PIRTs. As in FY05, ANL, INL and KAERI have collaborated in the on-going companion I-NERI project and are producing consensus high-level PIRTs. Comments on the PIRTs were also received from ORNL [1.3].

Reactor cavity heat transfer from the vessel surface to the RCCS has previously been identified as an important phenomenon [1.4]. Progress on definition of modeling and experimental needs for the relevant phenomena is summarized in [1.4] and [1.5]. Maintaining vessel, support structure and concrete integrity during the limiting accidents is essential to maintaining coolable geometry for the core in the safety case.

In FY05 and FY06, for all the events which have been screened to date, the phenomenon of core flow distribution has been identified as a phenomenon with high rank in importance for the safety criteria. The steady-state core flow and the bypass at normal operation sets the core initial peaking conditions for the accidents and transient scenarios. Uncertainty in the initial flow conditions of the core would not only effect the fuel margins at the steady-state but would also propagate into the uncertainties on the safety criteria for other events in the plant duty cycle. In the case of the PMR with the interblock gaps, radial and axial manufacturing and refueling tolerances for the graphite blocks, irradiation swelling and cracking and the distribution of the thermal expansion past experience and expertise indicates that the core bypass flow could be a significant proportion of the total core flow. Similarly in the case of the PBR, with the random pebble and coolant void distribution, edge effects at the center and side reflectors and the sideways leakage through the "loose-fitting" graphite pieces that form these reflectors, a similar consensus has been reached that the flow bypassing the core central regions could be a significant proportion of the total core flow. Modeling of this flow is an important need. To further explore the modeling needs for this phenomenon and proceed further

with the CSAU process, it was decided to proceed to the step of identifying underlying phenomena ("subphenomena") and performing sensitivity calculations to evaluate the relative importance of these subphenomena to the safety criteria. Eventually these sensitivity studies will be utilized in the scaling analysis to filter out non-dimensionless groups of lesser importance and also in the weighting of the contribution to the uncertainty assessment by each phenomenon. Chapter 5 details this work and its results for both the generic PMR option and the generic PBR option.

In addition to the identification of the core-bypass flow as an important phenomenon, the PIRT screening effort has also identified cooling mixing/stratification in the plena of the vessel and graphite oxidation of the core and the structures as important phenomena that need to be modeled in the thermo-fluid design and safety analyses tools. Plena temperature stratification with streaking and jetting implications has consequences for the reactor structure, both under normal operation steady-state and accident transient conditions. Poor mixing of the core outlet jets could lead to spatial and temporal temperature variations in the coolant flow exiting the lower plenum. These variations in flow conditions impinging upon the turbine inlet structure and blades could lead to thermal cycling and fatigue, which is not optimum for structural integrity. Similarly during pressurized accident conditions, streaking of hot plumes into the top inlet plenum could also have unintended consequences for the top structures. Identification of important subphenomena consequence and modeling and experimental needs for plena mixing are being carried out at INL. The phenomena of exothermic graphite oxidation leads to the introduction of an additional heat source separate from the decay heat generated by the fission products, which would lead to further primary system degradation. This would increase the fission product source from additional high temperature fuel particle failures and transport of fission products from the core to the external environment. Loss of structural strength due to the hasher conditions could lead to degradation of the coolable geometry. Further detail regarding this graphite oxidation phenomenon can be obtained in the ORNL reference [1.6]. This ANL report for the GEN IV Design & Evaluation Methods task focuses on and documents the work on the phenomena of the core flow distribution and the generation of the PIRTs in FY06. A summary of the conclusions to support the VHTR Design Methods Development and Validation R&D Program [1.7] is given in Chapter 6. Proposals for future work are discussed.

References

1.1 R. B Vilim, E. E. Feldman, W. D. Pointer and T.Y.C. Wei, "Initial VHTR Accident Scenarios Classification: Models and Data", ANL-GENIV-057, Argonne National Laboratory Report, September 2005.

1.2 W. J. Lee, et. al, "Generation of a Preliminary PIRT (Phenomena Identification and Ranking Table) for Very High Temperature Gas-Cooled Reactors", KAERI/TR-3050/2005, Korea Atomic Energy Research Institute Report, September 2005.

1.3 S. Ball, personal communication, March 2006.

1.4 R. B. Vilim, et. al., "Initial VHTR Accident Scenario Classification: Models and Data Status Report", Argonne National Laboratory Report, September 2004.
1.5 M. R. Farmer, et. al., "Natural Convection Shutdown Heat Removal Test Facility (NSTF) Evaluation for Generating Additional Reactor Cavity Cooling System (RCCS) Data", ANL-GENIV-058, Argonne National Laboratory Report, September 2005.
1.6 S. J. Ball, "NGNP Depressurized Loss of Forced Circulation (D-LOFC) Accidents with Air Ingress", Oak Ridge National Laboratory Report, ORNL/Gen4/LTR-06-026, September 2006.
1.7 R. R. Schultz, et. al., "Very High Temperature Reactor Design Methods Development and Validation Research and Development Program Plan", Idaho National Laboratory Report, INEEL/EXT-04-02293, Rev. 2, September 2005.

2.0 VHTR Design Description

Generic VHTR candidate design descriptions [2.1] that were used for the generation of the PIRTs documented in this report, are given in this chapter. The candidate VHTR designs are an extension of the earlier designs of the Gas Turbine-Modular High Temperature Reactor (GT-MHR) and the Pebble Bed Modular Reactor (PBMR). The GT-MHR is a 600MWth direct cycle gas reactor with a prismatic core. Reactor operating pressure is 70 bars and outlet temperature is 850°C. The reference PBMR is a 400MWth direct cycle gas reactor with a pebble core. Reactor operating pressure is 90 bars and outlet temperature is 900°C. Table 2.1 shows the main design conditions. The VHTR differs from these designs mainly in that the target reactor outlet temperature will probably be higher, although a specific target has not been defined, and the VHTR is to produce hydrogen in addition to electricity. Both designs are assumed to have confinements. That is, the reactor cavity is vented to atmosphere if the cavity is over pressurized. However, the vent (pressure relief valve) is fitted with a filter to minimize the release of harmful material to the environment, and the pressure relief will close once the confinement pressure is reduced to an acceptable value. The two reactor system designs differ mainly in the core configuration, that is, prismatic or pebble form for the reactor fuel. This has implications in the layout of the vessel and its internals particularly from the functional viewpoint of fueling and defueling.

2.1 Prismatic Modular Reactor (PMR)

The prismatic core consists of an inner reflector region surrounded by an annulus of fuel blocks that is in turn surrounded by an annulus of outer reflector elements. The fuel blocks are composed of hexagonal columns of graphite with circular holes that run the length of the column. The fueled holes contain fuel compact that contains TRISO particles, while the coolant holes align axially to form coolant channels. Figure 2.1 shows the PMR fuel and core plane layout.

Some important parameters and conditions related to the core are given in Table 2.1.

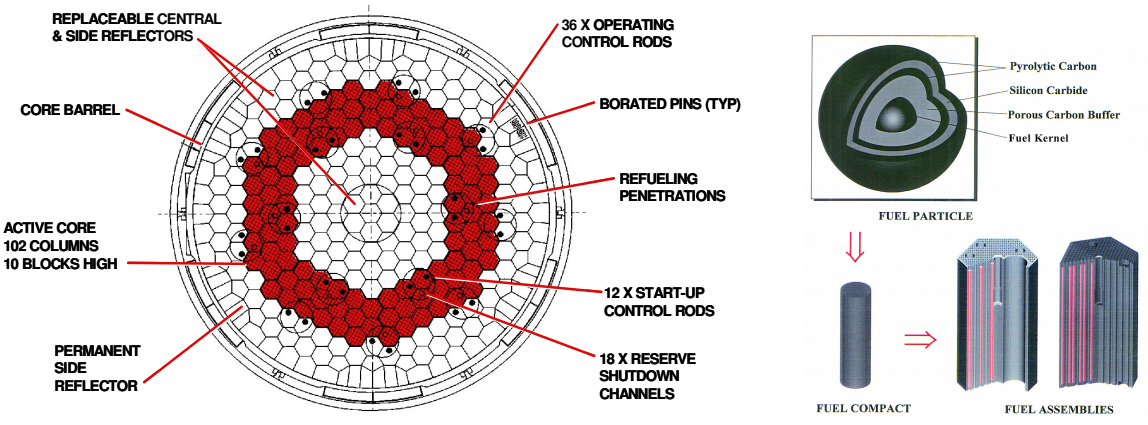

Fig. 2.1 PMR Core and Fuel

Table 2.1. Core Parameters and Full Power Operating Conditions

Parameter	GT-MHR	PBMR
Reactor Power, Q (Mwt)	600	400
T_{in}/T_{out} (^{o}C)	491/850	500/900
Reactor Pressure (bars)	70	90
Power Density (W/cc)	~ 5	~ 6.6
Reactor Mass Flowrate , W (kg/s)	320	147
Effective Core Height (m)	7.93	~ 11
Core Diameter (m)	2.96 ID/4.83 OD	2 ID/3.7 OD
Number of Fuel Blocks/Pebbles	1020	~ 450,000
Bypass Flow Fraction (%)	10 ~ 15	-

For the prismatic core, the helium coolant within the hexagonal blocks follows well defined one-dimensional flow paths described by the coolant channels. However, an undefined quantity of bypass flow, ranging from ~10% to ~25% of the total coolant, moves between the blocks. The bypass flow varies according to the quality of the block construction, the movement of the graphite as a function of irradiation and temperature and the core design and stacking procedures. Contact heat transfer between the blocks plays an important role in transmitting core afterheat during accidents. The moderator in the PMR, as in the PBR, is graphite. Moreover the fuel temperature limits rely on forced flow, provided by blowers, of the helium coolant during operation. The helium coolant flow distribution in the core is governed by the differential pressure between the upper and lower plena, the friction in the respective flow paths and the local power generation.

The configuration of the PMR primary vessel flow is discussed briefly from the perspective of Fig. 2.2. As with the PBR, the working fluid is helium for the PMR. The helium enters the vessel through an annular pipe near the bottom of the vessel in a direction that is at right angles to the axis of the reactor vessel. In the prismatic design, helium flow from the loop is mixed and redistributed in the inlet plenum and flows upward through six square riser ducts between the core barrel and the vessel wall. This is a 90-degree turn upward and is distributed into riser channels that lead upward to a top plenum that is located over the core. It is collected in the hemispheric top plenum and then flow into the core. The flow is directed downward from the top plenum into the core. It moves from the core into a outlet plenum and is directed to a circular cross-section pipe (the hot duct) that is mounted at a right angle to the reactor vessel centerline. As the helium transits the core, the gas temperature increases (400 ~ 500 °C). Finally the flow enters the power conversion vessel and is directed to the turbine inlet. In order to prevent overheating at the vessel, thermal insulation is provided at the inner side of the vessel head. The helium jets discharged from the core are collected and mixed in the outlet plenum and then flows out off the vessel to the PCU. However, considering the expected increase in vessel outlet temperature of the VHTR design, the current riser design of the prismatic vessel option may not be adequate to meet the design limit of the vessel wall temperature. There may have to be a modification of the vessel internal flow path design in order to lower the vessel wall temperature. One of the options is to have

the riser flow channel through the permanent outlet reflector similar to the pebble bed reactor design.

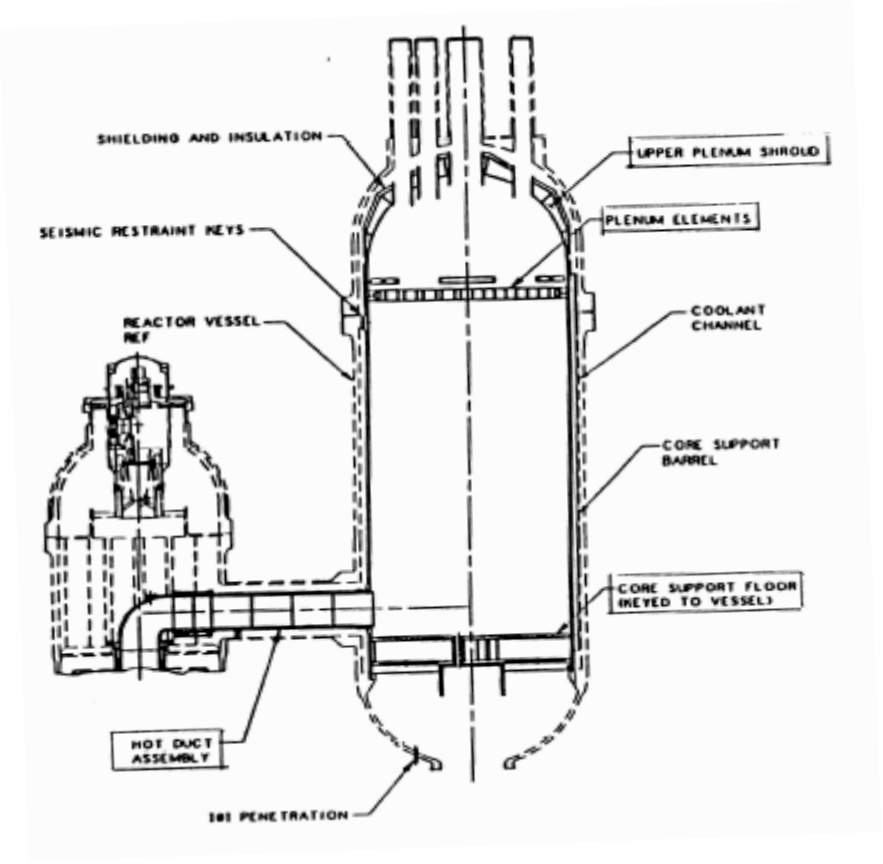

(a) Vessel Internal Structures

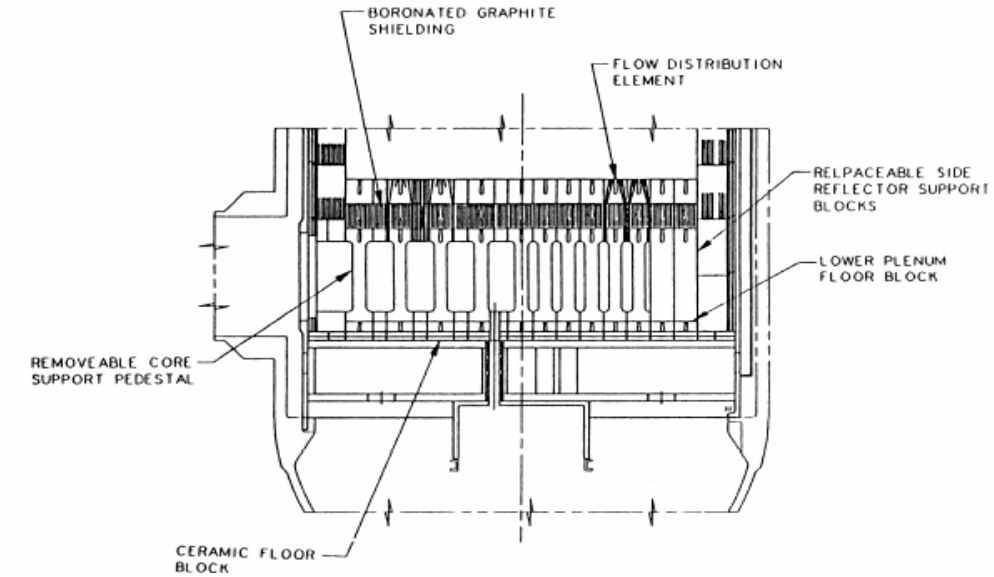

(b) Vessel Outlet Plenum

Fig. 2.2 PMR Vessel Internals

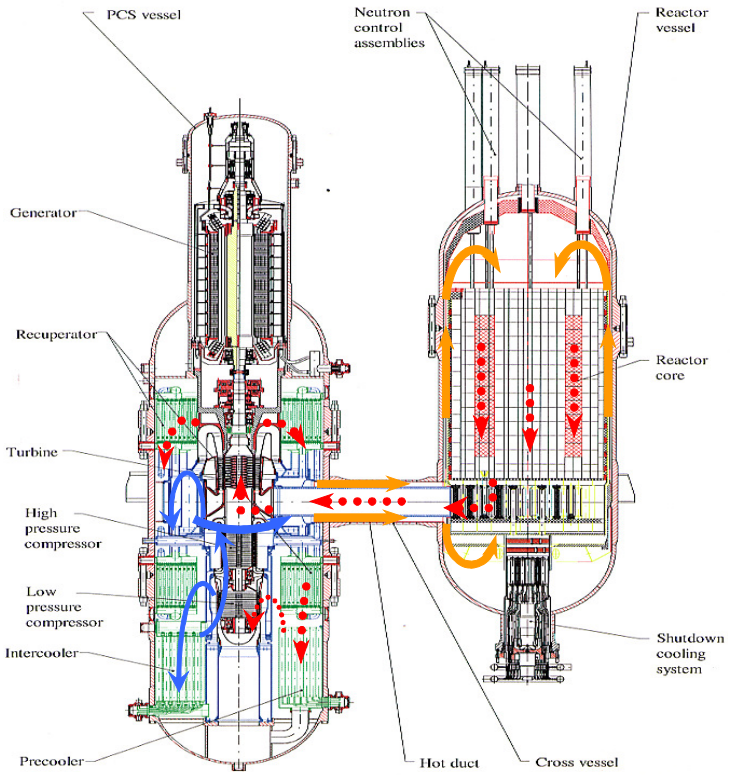

Fig. 2.3 PMR Plant Configuration

The basic concept of the system layout is the same for both designs as far as the components of the balance of plant (BOP) is concerned. The variation of the Brayton cycle utilized is similar for both plants. However, the GT-MHR design adopts an integral power conversion unit (PCU) in a vessel and a concentric hot/cold duct that connects the reactor system vessel and the PCU system vessel. This is shown in Fig. 2.3. Both designs rely on passive cooling during any loss-of-power scenario or loss-of-coolant scenarios. The ultimate heat sink is the environment, and all excess heat can be transported to the environment without natural circulation cooling inside the vessel via heat conduction and radiation to the vessel walls. From the vessel wall, the heat is transported to the environment via a combination of radiation and natural circulation transport using some form of RCCS. Air is present in the confinement such that if the reactor depressurizes due to a leak in a pipe, air will ultimately ingress into the vessel by diffusion.

There can be major differences in the RCCS designs. The GT-MHR design uses an air-cooled RCCS, while it appears that the AREVA-ANTARES design may be a water-cooled RCCS. A water-cooled RCCS was chosen for the PBMR. An air-cooled RCCS was used as the reference in this study for both the PMR and PBR designs since not much information is available regarding the ANTARES or PBMR RCCS. In the air-cooled RCCS design, heat is radiated from the exterior of the reactor vessel wall to a series of heat exchangers that are oriented vertically and arranged in a circle around the exterior of the reactor vessel. Air flowing within these heat exchangers (ducts) transports

the heat to the exterior of the confinement. The air is ducted in from outside the containment to these heat exchangers and then outside the confinement. The heat exchangers are rectangular ducts with a large aspect ratio and arranged so that one of the short sides faces the reactor vessel. This requires that the flow exiting the heat exchangers be ducted to chimneys leading to the outside to induce a sufficient natural draft. The walls of the heat exchangers and the ducts that connect to them provide a barrier that separates the coolant flowing through the heat exchangers from the atmosphere inside the reactor/silo confinement. The air-cooled RCCS system is designed to be totally passive under all operating condition and has no blowers to power the air flow through the heat exchangers. There are 292 risers, each a 5 by 25.4 cm rectangular duct. There is a 5 cm gap between adjacent risers and the short sides of each riser face the reactor vessel or the downcomer. The full power thermal-hydraulic conditions are given in Table 2.2 and Fig. 2.4 is a schematic of the RCCS.

Table 2.2 RCCS Duct Dimensions and Operating Conditions

Parameter	Air-cooled RCCS
RCCS Power (MWth)	3.3
RCCS Air Flowrate (kg/s)	14.3
Number of Ducts	292
Average Duct Air Flowrate (kg/s)	0.049
Duct Dimensions (m)	0.05 x 0.25
Hydraulic Diameter (m)	0.083
Length of Active Core Region (m)	7.93

2.2. Pebble Bed Reactor (PBR)

The 400 MWth pebble core consists of approximately 450,000 fuel pebbles that are stacked in a graphite reflector structure. Pebbles are continuously refueled during plant operation. Figure 2.5 shows the axial core layout and fuel for the PBR. The central reflector pebbles have been replaced by central graphite reflector column in the recent design. The helium coolant moving through the pebble-bed core follows multi-dimensional flow paths defined by the pebble-void fraction, which varies as a function of core radius, and the individual contact points described by the pebble column. During accidents, radiation and contact heat transfer between pebbles plays an important role in transmitting core afterheat to the reactor vessel wall. The core axial power distribution in the pebble core is more apt to be top-skewed than in the prismatic core due to the on-line refueling of fresh pebbles from the top. Even though the underlying design characteristics of both VHTR candidates are common and similar, the detailed designs of the reactor vessel internals are different in the two cases. In the pebble bed reactor design (see Fig. 2.6), helium flow from the loop is distributed in the donut-like inlet plenum and flows upward through the riser consisting of 36 circular channels inside the outer reflector. It passes through the slots at the top of the riser and collects in the cylindrical top plenum inside the upper graphite structure. It then flows downward to the core.

Helium that exits from the core is collected and mixed in the outlet plenum and then flows out of the vessel to the PCU. The helium enters the vessel through a circular cross-section pipe near the bottom of the vessel at a right angle to the vessel axis. The pebble-bed core slowly moves downward while the prismatic core is stationary. The cycle time through the core for an individual pebble is approximately 80 days. The transit distance is ~9.5 m. The reactor kinetics and burnup characteristics are functions of the fuel and moderator geometry, the fuel enrichment and the refueling characteristics of the respective designs. Because the pebble-bed core is continuously being replenished as spent pebbles are removed from the system (each pebble is cycled through the core approximately 9 times), the pebble-bed core generally has a wider spectrum of depletion during operation than the prismatic reactor.

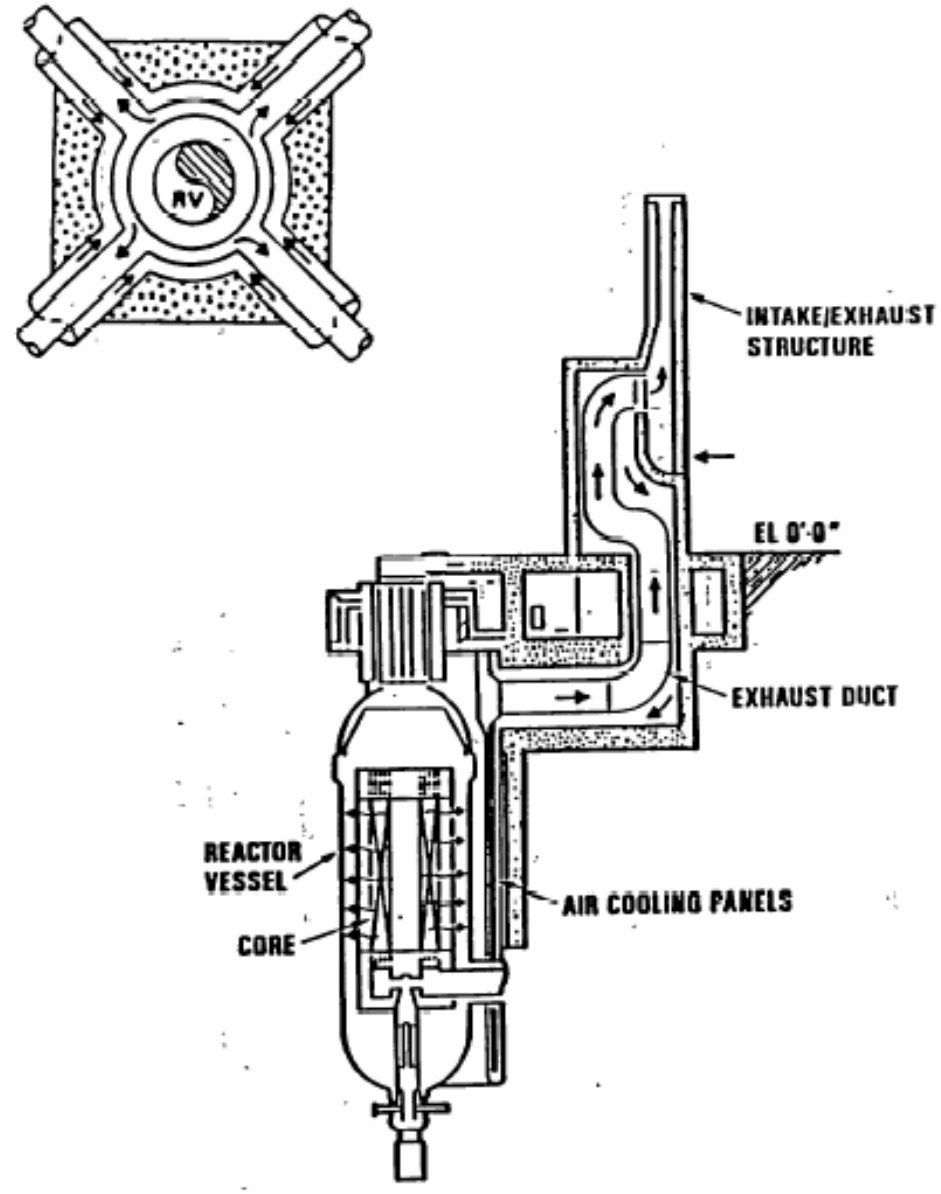

Fig. 2.4 Schematics of Air-Cooled RCCS

Figure 2.7 shows the plant configuration for the PBR. The PBMR design adopts distributed PCU components and separated hot and cold ducts. This leads to a larger footprint for the BOP with major lengths of ducting. Thermal stratification in the ducting may be quite different. This is an example of event phenomena differences which the differences in the design may lead to and which will be detailed in the PIRTs.

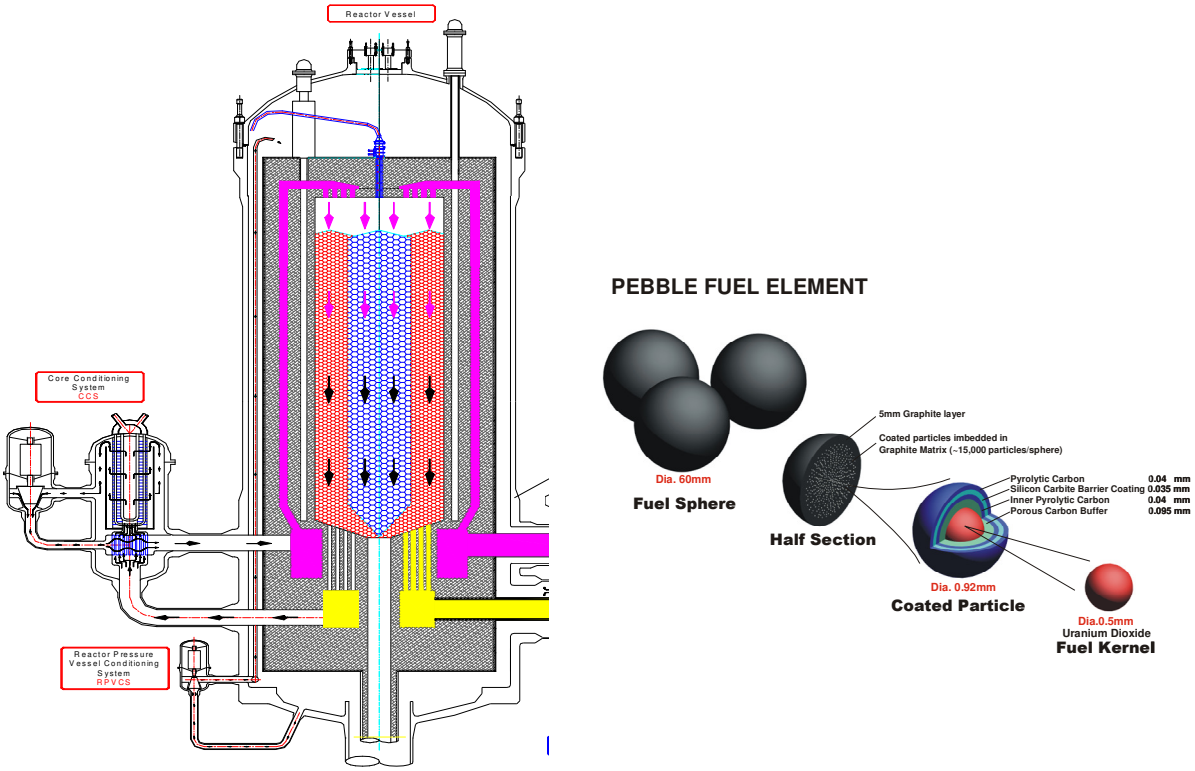

Fig. 2.5 PBR Core and Fuel

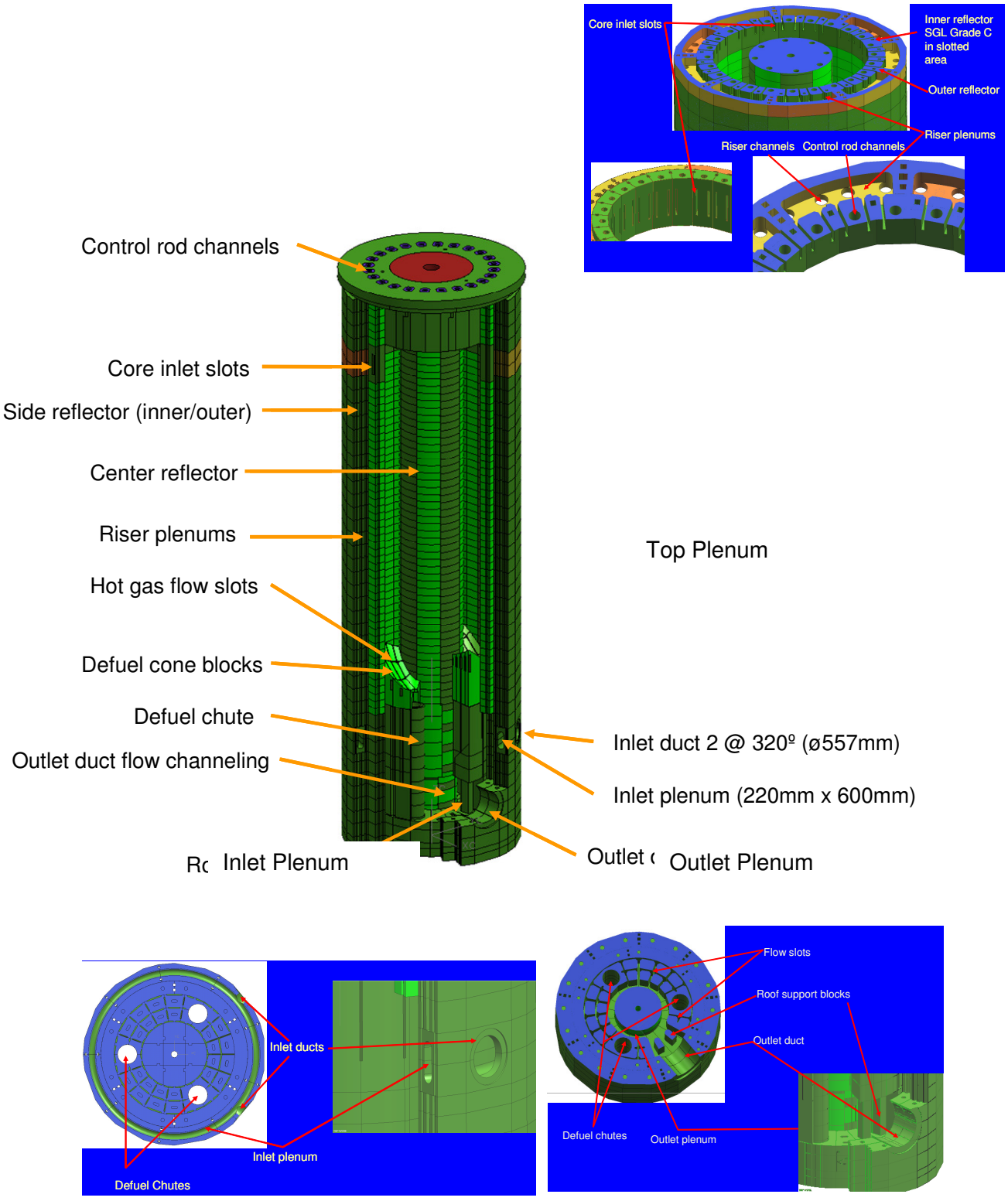

Fig 2.6 Pebble Reactor Vessel Internals

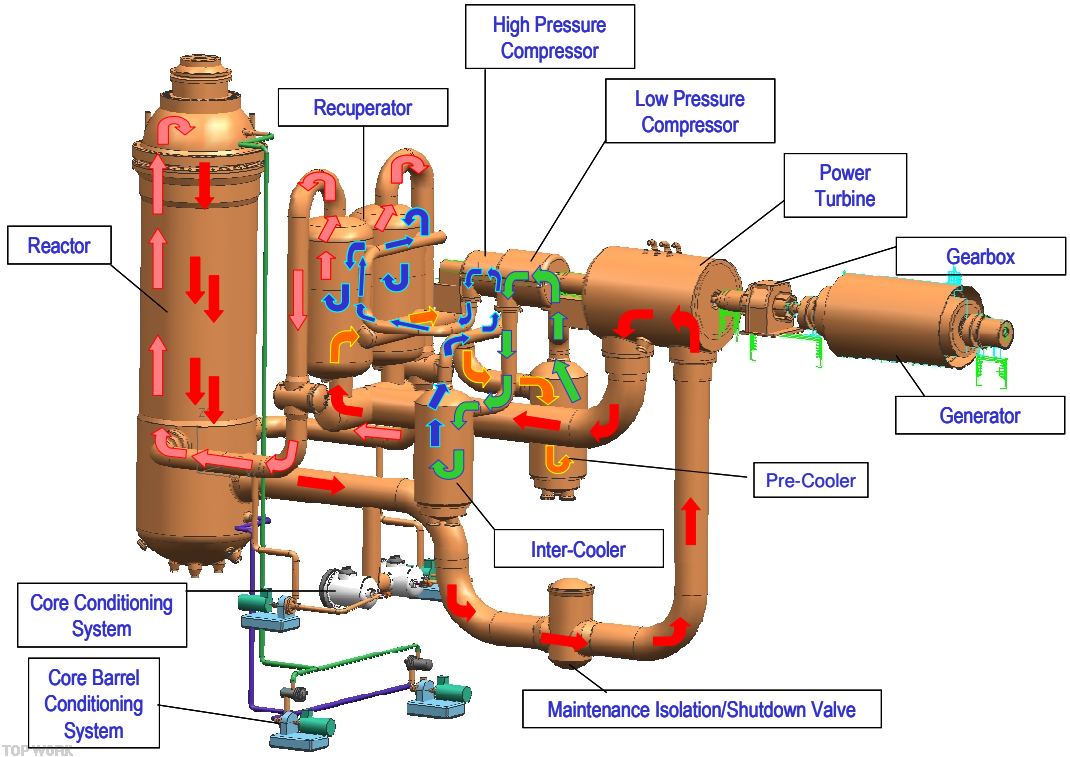

Fig. 2.7 PBR Plant Configuration

References

2.1 W. J. Lee, et. al., "Generation of Preliminary PIRT (Phenomena Identification and Ranking Table) for Very High Temperature Gas-Cooled Reactors", KAERI/TR-3050/2005, Korea Atomic Energy Research Institute Report, September 2005.

3.0 Selection of Accident Sequence

3.1 Background on Sequences

A design plant duty cycle, which lists the types of events and sequences which the systems and components must be designed to accommodate, will eventually need to be developed for the VHTR/NGNP. The plant duty cycle includes the modes of operation and the plant operational transients as well as the accidents and safety transients that should be considered in evaluating the structural design of the systems and components of the NSSS. The spectrum of events that are to be considered range from normal operational occurrences (startup, change of load), anticipated operational occurrences (AOO) (e.g., a loss of electrical load resulting from a line fault), off-design transients and postulated accidents of low probability (e.g., the sudden loss of integrity of a major component) to design basis events (DBE) and beyond. This spectrum of events dictates the requirements for the models of the design and safety analysis tools that are needed. Protection of the public requires an assessment of the consequences and frequencies of potential fuel failure scenarios. Figure 3.1 taken from the draft pre-application Safety Evaluation Report for the Modular High-Temperature Gas-Cooled Reactor (MHTGR) [3.1] shows the estimated frequencies/consequences developed by DOE for the General Atomics (GA) steam cycle MHTGR. It shows the ranges for the AOOs and DBEs which were presented during the licensing discussions with the NRC. The Fort St. Vrain plant, which could be considered as a predecessor to the MHTGR, was licensed before the establishment of the NRC. Figure 3.1 and the interactions with the NRC over the accompanying safety case for the MHTGR was built largely on the LWR experience. At the level of the safety goals and the categorization of the events according to the expected frequency of occurrence, the experience could be translated to a certain extent. However, when translating the FSAR Chapter 15 transient and accident classification developed for the LWRs, the correspondence is not necessarily one to one. Table 3.1 shows the Reg Guide 1.70 [3.2] categorization.

Table 3.1 FSAR Chapter 15 Accident Categories

1.	Increase in heat removal by the secondary system
2.	Decrease in heat removal by the secondary system
3.	Decrease in reactor coolant system flow rate
4.	Reactivity and power distribution anomalies
5.	Increase in reactor coolant inventory
6.	Decrease in reactor coolant inventory
7.	Radioactive release from a subsystem or component
8.	Anticipated transients without scram

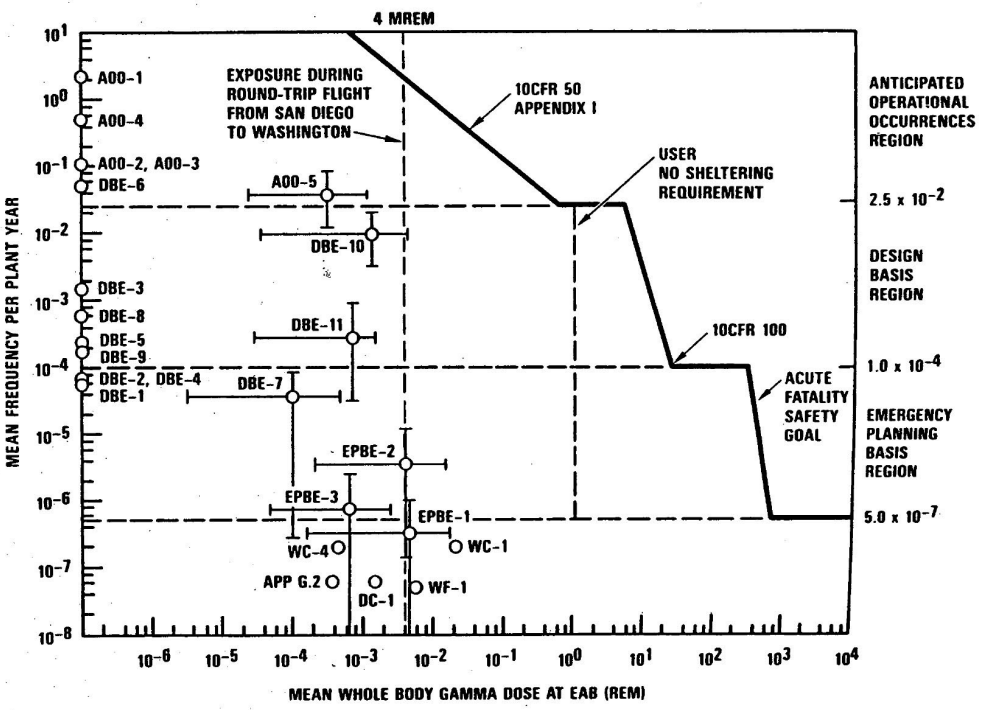

Fig. 3.1 Assignment of Top-Level Regulatory Criteria and Results of Safety Analysis Source: DOE, 1986-3 [3.1]

This is to be compared with Table 3.2 which is based on Section IV (Safety Analysis) from the Fort St. Vrain FSAR [3.3].

Table 3.2 Fort St. Vrain Chapter 14 [3.3]

1.	Environmental Disturbances
2.	Reactivity Accidents
3.	Incidents 3.1 Reactor Core 3.2 Primary Coolant System 3.3 Control and Instrumentation System 3.4 PCRV 3.5 Secondary Coolant and PCS 3.6 Electrical System 3.7 Helium Purification System 3.8 Helium Storage System 3.9 Nitrogen System
4.	Loss of Normal Shutdown Cooling
5.	Secondary Coolant System Leakage
6.	Auxiliary System Leakage
7.	Primary Coolant Leakage
8.	Maximum Credible Accident
9.	Maximum Hypothetical Accident
10.	DBA No. 1 “Permanent Loss of Forced Circulation”
11.	DBA No. 2 “Rapid Depressurization/Blowdown”

The differences between the LWR table and the HTGR table are evident.

Subsequent to Fort St. Vrain, the next U.S. gas reactor project was the GA MHTGR sponsored by DOE. Table 3.3 taken from [3.1] shows MHTGR occurrences and events.

Table 3.3 GA MHTGR Occurrences/Events

		Occurrence/Event
Anticipated Operational Occurrences (A00s)	A00-1	Main-loop transient with forced core cooling
	A00-2	Loss of main and shutdown cooling loops
	A00-3	Control-rod-group withdrawal with control rod trip
	A00-4	Small steam generator leak
	A00-5	Small primary-coolant leak
Design-Basis Events (DBEs)	DBE-1	Loss of heat transport system (HTS) and shutdown cooling system (SCS) cooling
	DBE-2	HTS transient without control rod trip
	DBE-3	Control-rod withdrawal without HTS cooling
	DBE-4	Control-rod withdrawal without HTS and SCS cooling
	DBE-5	Earthquake
	DBE-6	Moisture inleakage
	DBE-7	Moisture inleakage without SCS cooling
	DBE-8	Moisture inleakage with moisture-monitor failure
	DBE-9	Moisture inleakage with steam-generator-dump failure
	DBE-10	Primary-coolant leak
	DBE-11	Primary-coolant leak without HTS and SCS cooling
Emergency-Planning-Basis Events (EPBEs)	EPBE-1	Moisture inleakage with delayed steam generator isolation and without forced cooling
	EPBE-2	Moisture inleakage with delayed steam generator isolation
	EPBE-3	Primary-coolant leak in all four modules with neither forced cooling nor helium purification system pumpdown

This is a cross-section of specific plant occurrences and events selected by DOE for analysis. This was utilized in the licensing interaction with NRC to demonstrate compliance with 10 CFR. Irrespective of whether the Reg Guide 1.70 Chapter 15 accident categorization or the Fort. St. Vrain Chapter 14 categorization is used, this set of occurrences/events was judged to be representative of the plant duty cycle spectrum and also limiting.

The term "licensing-basis events (LBEs)" was used by DOE to include events within the "design-basis" region; that is, events with frequencies ranging from 2 x 10^{-2} down to 10^{-4} per plant-year. Reference [3.1] discusses two types of events in this category. The first type, identified as design-basis events (DBEs), permits some availability and performance of normally operating or standby equipment regardless of its quality rating. These DBEs are listed in Table 3.3. The first five events are known as "pressurized-conduction-cooldown events" that would have the following initiators: (1) loss of all ac power, (2) loss of main heat transport system (HTS) cooling followed by failure to trip (an anticipated transient without scram [ATWS] event), (3) control-rod-group withdrawal followed by the loss of the HTS, (4) rod-group withdrawal with the loss of both the HTS and the shutdown cooling system (SCS), and (5) safe-shutdown earthquake with loss of both the HTS and the SCS. Events 6 through 11 are "depressurized conduction cooldowns" and, since the primary coolant boundary is violated, some DBEs result in small offsite doses based on circulating radioactivity and the liftoff of plated-out fission products in the primary system. In the case of the MHTGR with its steam cycle, events 6 through 9 describe various cases of steam generator tube leaks and equipment failures. Events 10 and 11 pertain to primary-system leaks from the steam generator vessel and reactor vessel, respectively. Event 10 analyzes a leak area corresponding to a rupture of the primary system pressure relief line. Event 11 corresponds to a ruptured instrument line.

Table 3.4 shows the MHTGR bounding events selected by the NRC for analysis [3.1]. Essentially all these events are judged to fall below or within the region entitled by DOE as "emergency planning basis" in terms of frequency.

Table 3.4 Bounding Events (BEs) for the MHTGR [3.1]

Number	Event
BE-1	Inadvertent withdrawal of all control rods, without reactor trip for 36 hours (one module): (1) Reactor system pressurized, with forced cooling available (2) Reactor system pressurized, with reactor cavity cooling system (RCCS) cooling only (3) Reactor system depressurized, with RCCS cooling only
BE-2	Station blackout (all modules) for 36 hours: (1) Reactor system pressurized (2) Reactor system depressurized
BE-3	Loss of forced cooling plus RCCS cooling for 36 hours (one module):
BE-4	Rupture of justifiable number of steam generator tubes with failure to isolate or dump steam generator: (1) Reactor system pressurized, RCCS 25 percent unblocked after 36 hours (2) Reactor system depressurized, RCCS 25 percent unblocked after 36 hours
BE-5	Rapid depressurization (one module). Double-ended guillotine break of crossduct with failure to trip (assume RCCS failed for 36 hours and 25 percent unblocked thereafter). Partial control-rod insertion after 36 hours.
BE-6	Severe external events consistent with those imposed on light-water reactors.

In part due to the MHTGR experience, GA in the follow-on GT-MHR design project defined four event categories for the GT-MHR plant safety assessment. This is shown in Table 3.5 [3.4].

Table 3.5 GT MHR Event Categories [3.4]

Conduction Cooldown
Turbomachinery Failure Modes
Heat Exchanger Failure Modes
Reactivity Excursion

The conduction cooldown category encompass the MHTGR pressurized and depressurized conduction cooldown events and are core heatup events that require residual heat removal. Turbomachinery failures are a new class due entirely to the novelty of utilizing gas turbines in the power conversion cycle. Heat exchanger failures are primarily water ingress events, while reactivity excursions are a well known class though there may now be different types of initiators. Air ingress would need to be considered in this scheme, as part of one of the four categories of events.

Since at this point there does not appear to be an accident categorization system officially approved by the NRC for advanced gas-cooled reactors, the collective experience provided by the Fort St. Vrain plant, the MHTGR and the GT-MHR has been relied upon for the selection of sequences performed in this report.

3.2 FY06 Sequences

In FY05, two design basis events thought to result in the maximum fuel and vessel temperatures were selected for PIRT generation. The Pressurized Conduction Cooldown (PCC) event is initiated by a loss of the main heat transport system coolers followed by a reactor trip and the failure of the Shutdown cooling System to start. The Depressurized Conduction Cooldown (DCC) event is initiated by a double-guillotine break of the coaxial hot-cold pipe that connects the reactor vessel to the Power Conversion Vessel. The reactor trips and the Shutdown Cooling System fail to start. Both the PCC and DCC appear in the lists in Tables 3.3 - 3.5. There are other events in Table 3.4 that result in more severe conditions, e.g., the events that result in depressurized condition with heat removal by conduction cooling and neutronic power generation. However, the simultaneous occurrence of initiating failures of these events is most unlikely and places the events in the beyond-design-basis category. These events are not treated in a licensing safety analysis and so there should be no need for a PIRT. The main safety criteria are 1) the maximum fuel temperature should not exceed 1600°C and 2) the maximum vessel temperature should not exceed 425°C for the PCC and 530°C for the DCC. These criteria are based on material properties. In addition for the DCC, there is a limit on the radiation release to the environment during blowdown. The main source of radioactivity will be graphite dust that is dislodged during depressurization. The PIRT should identify those phenomena and components that are important to remaining within these limits. A third event thought to result in a local hot spot was

selected for PIRT generation. The Load Change is an operational transient initiated by a reduction in plant power from full power to a new steady state. The main concern is the relocation of a structure hot spot during the transient and the thermal stresses generated. The temperature field at the turbine inlet piping has been suggested as an area for concern. [3.5]

In FY06, the focus is on (i) Water Ingress, (ii) Rod Runout, and (iii) Hydrogen Plant Upset. The selection of a scenario for PIRT generation is guided by the criterion for probability of occurrence and consequence of outcome. The approach is to identify candidate scenarios and evaluate them with respect to the criterion.

3.2.1 Water Ingress

Water Ingress candidate scenarios have the following components: a potential pathway under which water can enter the primary system, the initial plant condition, an initiating event, subsequent failures and any protection system actions that stabilize the event. Once scenarios have been listed, they are ranked according to probability of occurrence and outcome and the scenario that best meets the criterion is selected for PIRT generation. This approach is taken below and the results appear in Table 3.6.

The GT-MHR has four water-based cooling systems for which there is a potential *pathway* to the primary coolant circuit. They are the Intercooler, the Precooler, the Shutdown Cooler and the Generator Cooling Systems. [3.4]

Heat exchanger tube failure is a primary *initiating event* for water ingress. It has a frequency of occurrence of approximately 0.01/reactor/year placing it in the anticipated upset category. With proper functioning of cooling loop isolation equipment the water inventory entering the primary system will be small and not of significant safety consequence. If, however, the leak is not isolated, the event becomes one of high consequence and of interest to safety analyses and, therefore, PIRT generation.

The *initial plant conditions* are at-power and shutdown. At full power, the pressure in the four water-based cooling circuits is less than the pressure in the primary circuit [3.4] and so a leak in one of these heat exchangers would result in flow, at least initially, out of the primary system into the water circuit. However, at partial power and assuming inventory control, the pressure in the primary system will drop below that of the Shutdown Cooling System [3.4]. In that case, water would flow into the primary system. The progression would depend on *subsequent failures* and on *protective system actions*.

Several combinations of the preceding italicized scenario components were examined to identify a scenario with the requisite probability and safety consequence for PIRT generation. Engineering judgment played a role in the selection of these scenarios. They are shown in Table 3.6. The first scenario assumes shutdown, either for refueling and maintenance, and, hence, the primary system is depressurized. A potential pressure differential for driving water into the primary system through a leak in any of these four

water-based systems would be small, possibly gravity driven. It is assumed the leak is safely isolated. During refueling the control rod drivelines are disconnected from the rods making it all but impossible for the rods to be removed by human or active system failure. Because coolant loop isolation is achieved, only a limited amount of water enters the primary system. It is assumed heat removal at decay power levels is provided by the RCCS. The fuel temperatures should remain safe. This event does not satisfy the small probability/high consequence criterion for PIRT generation.

The second scenario in Table 3.6 assumes the plant is at power and that a leak develops in a heat exchanger but that it is isolated so water ingress into the primary system is limited. Isolating the leak additionally closes the pathway between the primary system and the cooling circuit preventing primary coolant from flowing into the cooling circuit. The reactor is scrammed and decay heat is removed by the RCCS. Again this event does not satisfy the small probability/high consequence criterion for PIRT generation.

The third scenario in Table 3.6 assumes again that the plant is at power and that a leak develops in a heat exchanger tube, but this time it is not isolated. Of the four cooling circuits, the positive driving force required for water to enter the primary system can exist only for the Shutdown Cooling System and only at reduced power. During normal operation the SCS coolant enters the reactor vessel and reaches temperatures that require it to be pressurized. By contrast the Precooler, Intercooler, and Generator Cooler all operate at low temperature (<150 C) so they are near atmospheric pressure. With inventory control at less than 70 percent full power the pressure in the reactor vessel drops below the pressure in the SCS so a positive driving force exists for water ingress. In summary, the third scenario in Table 3.6 assumes water enters the primary circuit through a SCS heat exchanger leak, the SCS is not isolated, and that the primary system remains pressurized since the SCS is also a pressurized system. The reactor is scrammed and decay heat is removed by the RCCS. Hydrolysis of core graphite would occur. The water inventory in the SCS is an important factor in this scenario. At this time, we do not know the inventory. The probability of this scenario is the product of the probability of a heat exchanger leak (10^{-2}/year) times the probability of failure to isolate (10^{-3}/year). This places the scenario in the Design Basis category. In combination with the possibility for significant fuel erosion through hydrolysis, this scenario appears to fit the criterion for requiring a safety analysis.

The fourth scenario in Table 3.6 takes in the possibility of significant water entering the reactor vessel at the depressurized condition. At the depressurized condition sufficient driving head through gravity alone might exist for water to enter through a heat exchanger tube leak in the Intercooler, Precooler, Shutdown Cooling, or Generator Cooling circuits. The scenario assumes the reactor is initially at power, there is a small leak in the reactor pressure boundary without isolation (10^{-4}/year) followed by a tube leak in one of the four cooling circuits (10^{-2}/year) but with failure to isolate (10^{-3}/year). The probability of this scenario is exceedingly small making it inappropriate for a first round PIRT. However, if the initial plant condition is shutdown for refueling/maintenance then

the combined probability of a tube leak and failure to isolate is 10^{-5}/year making this a candidate for a first round PIRT.

Table 3.6 Scenarios for Water Ingress with Probability and Outcome

Pathways for Water Ingress	Sequence				Safety Analysis	
	Initial Plant Condition	Initiating Event	Subsequent Failures	Terminal Condition	Probability (/year)	Outcome
SCS Precooler Intercooler Generator Cooler	Shutdown for Refueling/ Maintenance	Tube leak in water-circuit HX followed by isolation.	-	Pressurized, scrammed, and heat removal by RCCS.	Anticipated (10^{-2})	Safe
SCS Precooler Intercooler Generator Cooler	At Power	Tube leak in water-circuit HX followed by isolation.	-	Pressurized, scrammed, and heat removal by RCCS.	Anticipated (10^{-2})	Safe
SCS Precooler Intercooler Generator Cooler	At Power	Tube leak in a water-circuit HX.	Failure to isolate HX.	Pressurized, scrammed, and heat removal by RCCS.	Design Basis ($10^{-2}*10^{-3}$)	Function of water inventory entering core.
SCS Precooler Intercooler Generator Cooler	At Power	Small leak in pressure boundary without isolation (result is DCC).	Tube leak in a water-circuit HX. Failure to isolate leak.	Depressurized, scrammed, and heat removal by RCCS.	Beyond Design Basis ($10^{-4}*10^{-2}*10^{-3}$)	Function of water inventory entering core.

It was also instructive to examine a water ingress scenario treated in the licensing of the MHTGR for its applicability to the GT-MHR. [3.6] The reactor is at full power when there is a rapid (of the order 10 seconds) ingress of large amounts of water such that the core helium is completely displaced by high temperature water vapor and the two independent reactivity shutdown systems fail to act. The source of high pressure water was a steam generator. In the GT-MHR there are water inventories in the Precooler and Intercooler Systems greater than in the MHTGR. At normal operation however, the pressure is significantly less than the primary system since the highest temperature in the coolers is less than 130 C, and, hence, there is not a physical means for transferring the cooler water to the primary system. The SCS is the only water-cooled heat removal system where the driving pressure during at-power operation appears sufficient to introduce inleakage into the primary coolant circuit. A SCS leak appears to be analogous to a steam generator leak in the MHTGR. In the GT-MHR at less than 70 percent power, there is a positive driving force for inleakage from the SCS, which is located in the reactor vessel directly downstream of the core. Presently, It is not clear that the SCS would have near the water inventory found in the steam generator of the MHTR since the heat removal capability is only a few percent of full power. Since the scenario just described consists of four failures, the probability of occurrence is vanishingly small so a first round PIRT is not warranted.

The accident scenario selected for PIRT generation is the third case in Table 3.6 with the assumption that the water ingress is from a leak in the Shutdown Cooling System and not from a leak in the Precooler, Intercooler, or Generator Cooling Systems for reasons described earlier. The third case of Table 3.5 meets the probability/outcome criterion described earlier.

3.2.2 Rod Runout

There are two scenarios for rod runout. One is runout of all control rods with the reactor shutdown for maintenance or refueling. The vessel is depressurized and heat removal is by the Shutdown Cooling System. The other is rod runout while at power. Safety analysis required for the VHTR will likely include simulation of both scenarios. As a consequence, PIRTs, will be needed to ensure all important phenomena have been included in the simulation. The present work, however, is to develop PIRTs for those accidents that present the most complex and off-normal behavior but still fall within the realm of possibility. The rod runout at power scenario includes thermal-hydraulic phenomena that are not present in the shutdown case. These involve primarily the thermal hydraulics related to operation of the balance of plant. The rod runout while at power is, therefore, selected for PIRT generation.

3.2.3 Hydrogen Plant Upset

For the Hydrogen Plant upset scenario, several factors are considered in the selection and definition of the scenario. The reactor protection system is assumed to perform its function by scramming the reactor when limiting safety settings are exceeded. The scenario that involves an intermediate loop leak cannot be addressed at this time. In

this scenario, coolant can leak into containment or into the primary system, but since at this time the intermediate coolant is not known, the phenomena associated with the fluid behavior inside containment or the primary system cannot be identified. The other scenario identified the unscheduled change in the heat load posed by the hydrogen plant at the interface is selected for PIRT generation. According to our earlier criterion (high consequence and low probability) this event is not a prime candidate for PIRT analysis. This is because the probability of core damage is much less than 10^{-4} per reactor year, and the probability of a significant radiation release is much less than 10^{-6} per reactor year since the reactor is successfully scrammed. However, precedence for performing a PIRT exists since the primary system energy balance upset caused by an event in the hydrogen plant parallels events that appear in the Fort Saint Vrain Reactor safety analysis report. These are an increase in cooling due to steam line break and a decrease in cooling due to loss of feedwater flow event.

The selection of a scenario is reduced to one of two choices: protected overcooling and protected undercooling of the primary system. For overcooling, the hydrogen plant is limited in its capacity to overcool the reactor. Heat transfer mechanisms and surface areas typically do not support increases in heat removal rates of beyond a few tens of a percent above normal. The exception is a large break in a heat transfer component that has a large pressurized liquid inventory with two-phase heat transfer occurring on depressurization. At this time, there is insufficient design information for the hydrogen plant to identify such a component. For under-cooling by the hydrogen plant, there are a number of perceived mechanisms by which the heat removal rate could fall to near zero. These include closure of a valve, stoppage of pumps on loss of electrical power or shutdown of the chemical process for safety reasons. The scenario selected for PIRT analysis then is an upset in the hydrogen plant that leads to a loss of cooling at the interface between the reactor and hydrogen plant.

References

3.1 P. M. Williams, T. L. King and J. N. Wilson “Draft Safety Evaluation Report for the Modular High-Temperature Gas-Cooled Reactor”, NUREG-1338, NRC Report (March 1989).

3.2 NRC Staff, “Standard Format and Content of Safety Analysis Reports for Nuclear Power Plants”, Regulatory Guide 1.70 Revision 3, NRC (November 1978).

3.3 Public Service Company of Colorado, Docket Number 267.

3.4 Gas Turbine-Modular Helium Reactor (GT-MHR) Conceptual Design Description Report, 910720, Revision 1, GA Project No. 7658, General Atomics, July 1996.

3.5 R. B. Vilim, et. al., “Initial VHTR Accident – Scenario Classification: Models and Data,” ANL-GENIV-057, Argonne National Laboratory Report, September 2005.

3.6 P. B. Kroeger, “Bounding Core Temperature Transients for Severe and Rapid Water Ingress Scenarios in Modular High Temperature Gas-Cooled Reactors,” Sixth Proceeding of Nuclear Thermal Hydraulics, American Nuclear Society, 1990, p. 263-273.

4.0 Phenomena Identification and Ranking Tables (PIRTs)

As discussed in Chapter 3, it was determined early in FY06 that PIRTs would be generated for three events that are likely to require safety analyses based on prior licensing of gas reactor designs. The *water ingress event* was an important accident case for the MHTGR.[4.1] One objective is to determine how the water ingress event in the VHTR might differ from the MHTGR. This includes examining differences in how water could enter the primary system. The rod reactivity insertion event is an anticipated event, and when followed by a failure to scram has important safety consequences. The current regulatory requirement for considering failure to scram arose in part from such an incident in the Fort Saint Vrain gas reactor.[4.2] The second event then is *rod withdrawal with failure to scram*. The third event is an *upset in the hydrogen plant*, an event not previously analyzed for HTGR since hydrogen production was not previously considered. The upset, however, results in an imbalance between reactor heat generation and removal making it similar to the overcooling and undercooling examined in safety studies of earlier gas reactors.

For each of these events, Chapter 3.0 identified the scenario that has the requisite level of probability and consequence. This is taken as the level that would precipitate the need for a safety analysis. Generally a safety analysis is required for those events where the probability of core damage is greater than 10^{-4} per reactor year and the probability of a significant radiation release is greater than 10^{-6} per reactor year. PIRT generation for these events is to support validation of the models in the computer code that is to be used in the safety analysis. This is the procedure followed for the large break LOCA safety studies performed for light-water reactors in the 1980s. Similarly, the work of this Gen IV VHTR task uses this procedure for accidents in the VHTR beginning with the conduction cooldown events for which PIRTS were generated in FY05.

There are presently three competing VHTR gas reactor designs – Antares by AREVA, the Westinghouse/South African PBMR design, and the GT-MHR by General Atomics. Consistent with our prior work [4.3], the study is mainly limited to the GT-MHR, and then, modifications are made according to generic design perturbations. With this approach to design differences, the aggregated PIRTs for the 3 events discussed on this chapter are presented at the end of the chapter. The main body of the chapter presents a discussion by event, of phenomena which occur in the various affected plant component at each phase of the event.

4.1 Water Ingress PIRT

Water ingress into the primary coolant system gives rise to new phenomena compared to those present at normal operation and thus is of interest from a safety standpoint. A sudden introduction of water into the core can change the neutronic characteristics of the core resulting in positive reactivity with a resulting increase in power. [4.4] If the power increase is large enough and the reactor fails to scram, fuel temperature safety limits will be exceeded followed by fuel microsphere failure. Water that enters the hot regions of the primary circuit will vaporize resulting in an increase in

the primary system pressure. This same coolant may condense at the coolers and enter the compressors as entrained liquid causing erosion and vibration. In addition, the hydrolysis of graphite in the core by water [4.5] can weaken the microsphere fission product barrier resulting in leakage of fission products into the primary system coolant. For this to happen however, the water must first permeate the outer graphite shell in the case of fuel balls and the graphite matrix in the case of the fuel blocks. A leak that introduces water into the primary system can lead to vessel over pressure causing the pressure vessel relief valves to lift and fission products to escape the primary system boundary. Finally, in those designs that employ a draft air RCCS for off-normal heat removal, water vapor and hydrolysis products (CO and H_2) escaping the primary vessel may enter the gap between the reactor vessel exterior and RCCS wall. Radiation heat transfer across this gap is an important means for removing residual heat in cooling accidents, and the presence of these gases may impede heat transfer. [4.6] This phenomena also applies to those designs which employ the alternative water cooled RCCS.

4.1.1 Scenario and Safety Criteria

It is assumed that the reactor is operating at less than 70 percent thermal power, and, hence, the pressure of the water in the SCS heat exchanger is greater than the primary system pressure. A breach in the SCS heat exchanger develops, and water flows into the primary system. It is assumed the SCS loop cannot be isolated so the water continues to flow into the reactor vessel. While this water may initially collect at the bottom of the reactor vessel, it will eventually vaporize leading to an increase in primary system pressure. Depending on how quickly it vaporizes, a reactor trip signal will be generated on either overpressure, or as the vapor is transported through the primary system, a trip will be generated on moisture detection. It is assumed that the reactor does scram, and that the turbomachine also trips. Depending on the neutronic characteristics of the core, before scram the vapor may add positive reactivity causing power to increase and generate a reactor trip signal on overpower. If vapor is transported to the power conversion vessel it will condense in the coolers. The condensate might be entrained in the helium and be transported to the compressors where an acoustic signal might be generated. The presence of water in the helium coolant could be expected to alter the performance characteristics of the turbomachine. On scramming of the reactor, the shutdown cooling system will start automatically and provide cooling. In the presence of a SCS heat exchanger tube leak, the SCS cannot necessarily be relied upon to provide heat removal. Either way, since the SCS is a safety system, the SCS circulator will continue to run. The SCS heat exchangers are located above the SCS check valve, which will be closed until the SCS circulator turns on. Water that does not vaporize will collect above the check valve until the circulator operates.

Upon scramming of the reactor, the turbomachine will trip and coast down. During this time the coolers will become less effective in removing heat so heat removal by the RCCS becomes more significant. There will be some cooling of the core by vaporization of the SCS water. Hydrolysis of graphite in the fuel elements may weaken the fission product barriers permitting fission products to enter the primary system coolant. If the pressure relief valves open on overpressure, some of these fission products

may enter the confinement. Opening of the pressure relief valve will remove energy from the primary system. The power of the core before scram will depend on the net reactivity which depends on the core temperature which depends on the imbalance between heat generation and heat removal. The reactivity will also depend on the effect of the water vapor on the fission process.

The relevant safety criteria depend on the progression of the accident. The peak fuel temperature is expected to increase as is the peak vessel temperature since cooling is provided by only the RCCS. The reactor vessel pressure relief system would prevent primary pressure boundary pressure limit from being exceeded but could result in fission products entering confinement. Thus, peak fuel temperature, peak vessel temperature, and confinement radiation limits are the relevant safety criteria.

4.1.2 Components

The components participating are the same components as in PCC event, and additionally the Shutdown Cooling System, the Lower Head, and the Pressure Boundary. A list is given in Table 4.1.

Table 4.1 Components Participating in Water Ingress Scenario

Systems	**Components**
Reactor Vessel	Inlet Plenum
	Riser
	Top Plenum and Components
	Core & Reflectors (Includes Bypass)
	Outlet Plenum and Components
	Lower Head
	Pressure Boundary
Reactor Coolant Loop	Hot/Cold Pipe
	Compressor (Direct) or Circulator (Indirect)
RCCS	Reactor Cavity (Confinement)
	RCCS Tube (Air Duct)
	RCCS Piping and Chimney
Shutdown Cooling System (SCS)	Heat Exchanger and Pump

4.1.3 Phases and Phenomena

4.1.3.1 Pre Turbomachine-Trip Phase

The discharge flow through the SCS heat exchanger leak into the primary system will depend on the pressure drop across the leak and the flow regime. The rate at which the leak water vaporizes depends on the flowrate through the leak, the rate at which

stored energy is removed from structures that interact with the liquid water, and the contact area of the water with structures and helium. The water that does not vaporize will collect on top of the SCS check valve, which lies below the SCS heat exchangers. The concentration of water vapor in the core depends on not only the preceding but also on the relative flowrate of helium to water vapor and the rate at which vapor is circulated to the coolers. It will condense and perhaps collect at the bottom of the coolers which effectively removes it from circulation. The presence of water vapor in the primary coolant will alter the performance characteristics of the turbomachine. Until the check valve opens there is not a mechanism to transport two-phase water through the system.

The core reactivity will be a function of usual reactivity components when at power but, additionally, the concentration of water vapor in the core. The water vapor will act to soften the spectrum, which will add reactivity if the core is undermoderated. The vapor combined with increased pressure will increase neutron scattering, which will reduce leakage and result in added reactivity. Reduced flux at the core periphery will reduce the worth of external control rods or poisons adding reactivity. Increased neutron absorption by the water will reduce reactivity. The net reactivity effect of all these processes will be core design and vapor concentration dependent. Prior to scram, the temperature of the core will tend toward a value that gives a net reactivity of zero.

4.1.3.2 Post Turbomachine-Trip Phase

When the turbomachine is tripped and coasts down, the primary means for heat removal changes. The RCCS will remove heat from the primary system, while additional energy will be removed if the primary system pressure relief valves open. The SCS will automatically activate, but the presence of a leak in the heat exchanger makes the heat removal capability uncertain. The SCS blower will run which will cause the check valve to open and water to be blown into the reactor inlet plenum. Since the blower is driving convection in the primary circuit, heat transfer and pressure drop are in the forced convection regime rather than mixed convection regime. There may be a maldistribution of water vapor entering the top plenum as a consequence of an asymmetry in the location of the water leak and/or the point where the water enters the inlet plenum. Hydrolysis of graphite will occur and possibly release fission products into the primary system.

4.2. Rod Withdrawal Anticipated Transient without Scram PIRT

Withdrawal of a control rod while the reactor is critical combined with a failure to scram will give rise to phenomena not present at normal operation. The PIRT provides an importance ranking of these phenomena and a basis for ensuring they are adequately represented in a safety analysis. In the rod withdrawal event, it is assumed that all control systems operate normally with the exception of the reactor power control system. This system is assumed to fail such that all rods except the withdrawn rod remain fixed in position. Then the only means for compensating for the reactivity insertion associated with the withdrawn rod is through passive reactivity feedback.

From an earlier discussion, an accident is a good candidate for PIRT generation if the probability of core damage is greater than 10^{-4} per reactor year and the probability of a significant radiation release is greater than 10^{-6} per reactor year. Recall these criteria are derived from the light water reactor industry. The probability of an uncontrolled rod runout is less than unity per reactor year and the failure to scram all three shutdown systems, i.e. control and safety rods and the reserve shutdown system, is much less than 10^{-6} per reactor year (the value used in LMR and LWR safety analyses is 10^{-6} per reactor year based on two independent shutdown systems). So the probability of radiation release will be significantly below 10^{-6} per reactor year. How much below is in part dependent on the phenomena and their role in limiting fuel temperature.

As an aside, conditions unique to the VHTR could alter the above assumed probability for failure to scram. One mechanism that may need to be considered in establishing this probability involves the chemical corrosion of steels exposed to water at high temperature. In the Fort Saint Vrain reactor, corrosion products from the reaction of water vapor with carbon steel components in the control rod drive system interfered with gravity feed insertion of the rods during a scram event.[4.8] The presence of water cooling circuits that interface with the primary system in the VHTR and the significantly higher operating temperatures may result in an increased probability of corrosion and, hence, failure to scram compared to an Liquid Metal Reactor (LMR). This risk might be minimized through the use of high-quality corrosion-resistant steels. A second mechanism that may alter the probability of failure to scram is suggested in [4.9]. There is a possibility that surface conditions on stainless steels in a dry helium environment with some oxygen present may result in sticking between sliding surfaces in control rod drivelines.

4.2.1 Scenario and Safety Criteria

The scenario begins with withdrawal of a control rod without active reactivity compensation. The core power rises in response causing fuel and reactor outlet temperature and system pressure to increase resulting in an automatic trip of the turbomachine and a scram signal. The reactor fails to scram. The coastdown of the turbomachine and consequent reduction of reactor cooling may cause fuel and reactor outlet temperature to increase further. Reactor power begins to decrease as negative reactivity associated with fuel temperature increase is introduced. The plant control system operates to run back the power. The cooler power is successfully reduced but the rods remain fixed in position. The SCS automatically starts up to provide active cooling of the core. The RCCS will cool the reactor vessel by virtue of the draft air circuit always being in place. As neutronic power decreases the removal of xenon no longer proceeds at a rate in equilibrium with its generation. The reactor eventually goes subcritical on xenon poisoning. As the xenon inventory decays criticality re-occurs. The reactor may oscillate in and out of criticality. The reactor continues to cooldown until an equilibrium zero-power critical state is reached.

The key response of the reactor is an initial increase in power which leads to an increase in temperatures in the core, the upper reflector, and the top of the reactor

pressure vessel. The important safety limits are peak fuel temperature and vessel wall temperature.

4.2.2 Components

The plant components participating in this event are listed in Table 4.2.

Table 4.2 Components Participating in Rod Withdrawal ATWS Scenario

Systems	Components
Reactor Vessel	Inlet Plenum
	Riser
	Top Plenum and Components
	Core & Reflectors (Includes Bypass)
	Outlet Plenum and Components
Reactor Coolant Loop	Hot/Cold Pipe
	Compressor (Direct) or Circulator (Indirect)
Shutdown Cooling System	Heat Exchanger and Pump
RCCS	Reactor Cavity (Confinement)
	RCCS Tube (Air Duct)
	RCCS Piping, Air Cooler and Chimney

4.2.3 Phases and Phenomena

4.2.3.1 Pre Turbomachine-Trip Phase

The time history of the reactivity addition resulting from the uncompensated rod withdrawal is a function of the rod worth gradient and the rod withdrawal rate. The total rod worth will be a function of the excess reactivity built into the core. In the PBR, this is maintained small by continual refueling. In the PMR, a burnable poison is used to limit the excess reactivity. The ratio of fuel to graphite in the core results in a neutron spectrum that is thermal rather than fast. Since the core dimensions are large compared to the mean free path of a thermal neutron, the reactor power response has a spatial dependence that requires space-time kinetics for precise prediction. Control rods closest to the core center will have greater worth than those at the periphery. There will be local flux peaking in the vicinity of the withdrawn rod. As the core power increases, the plant control system will attempt to maintain constant power removal via the generator. The reactor system temperature will increase as a result of the imbalance between heating and cooling and as a result reactor pressure will increase. The turbomachine will trip on either reactor outlet temperature, power, or primary system pressure.

4.2.3.2 Coastdown Phase

Upon the loss of the generator as an energy sink, the plant control system will attempt to reduce the heat generation and heat removal rates to bring the plant to a

shutdown state. The turbomachine will coastdown as the cooler powers are reduced, and the bypass valve is opened. The reactor temperature will continue to increase until sufficient negative reactivity due to Doppler feedback is developed to bring neutronic power production into equilibrium with heat removal rate. The rate of core temperature increase will be a function of the core heat capacity. The increase in reactor temperature caused by the heat from decay products minus the heat removed through the Shutdown Cooling System and the Reactor Cavity Cooling System. The reactor may eventually go subcritical as temperatures rise above those that produce neutronic equilibrium.

4.2.3.3 Post Turbomachine-Trip Equilibrium Phase

As decay power decreases over time, temperatures will eventually begin to drop reaching values for which net reactivity exclusive of xenon reactivity is zero. Then, if it were not for xenon poisoning, the neutronic power would assume a value in equilibrium with heat removal rate. Further out in time, sufficient xenon will have decayed and core temperatures will have decreased on reduced decay heating that recriticality occurs. Power oscillations are possible as temperature feedbacks, xenon generation, and heat removal processes interact in a dynamic manner. With increased viscosity in hotter channels coupled with potential overcooling of cooler channels by SCS flow there may be the potential for selective undercooling.[4.10]

4.3 Hydrogen Plant Upset PIRT

The VHTR has the capability to generate both electricity and hydrogen. In the U.S., the DOE plans are for generation of both products, while KAERI plans are to generate hydrogen only. The schematic of the U.S. concept in Fig. 4.1 shows two parallel heat transfer paths from the reactor, one for electricity production and one for hydrogen production. In the KAERI concept, shown in Fig. 4.2, a single heat transfer path from the reactor delivers process heat to the chemical plant. In both design concepts the heat transfer path to the chemical plant is composed of a series of intermediate process heat loops. The thermal power delivered to the hydrogen plant in the U.S. concept is less than 50 MWt which is modest when compared to the reactor thermal power of 600 MWt. In the KAERI version of the VHTR, the entire reactor thermal output is delivered to the chemical plant.

An upset in the hydrogen plant will propagate through the series of intermediate heat transfer loops that couple the hydrogen plant to the reactor. The result will be an imbalance between energy production in the primary system and energy removal from the primary system. Because a PIRT is directed at reactor systems computer code qualification, the focus of the PIRT is on the resulting phenomena in the reactor plant and how they depend on the boundary conditions at the interface between the hydrogen and nuclear plants. Thus, it is not necessary to represent the specifics of an upset in the hydrogen plant, just the net result from a heat transfer standpoint as seen at the interface. An energy imbalance in the primary system can arise from either an unscheduled change in the heat load posed by the hydrogen plant as seen at the interface (either overcooling or undercooling) or as a change in heat load seen at the interface as the result of a leak of coolant in one of the intermediate loops and subsequent loss of heat transfer capability.

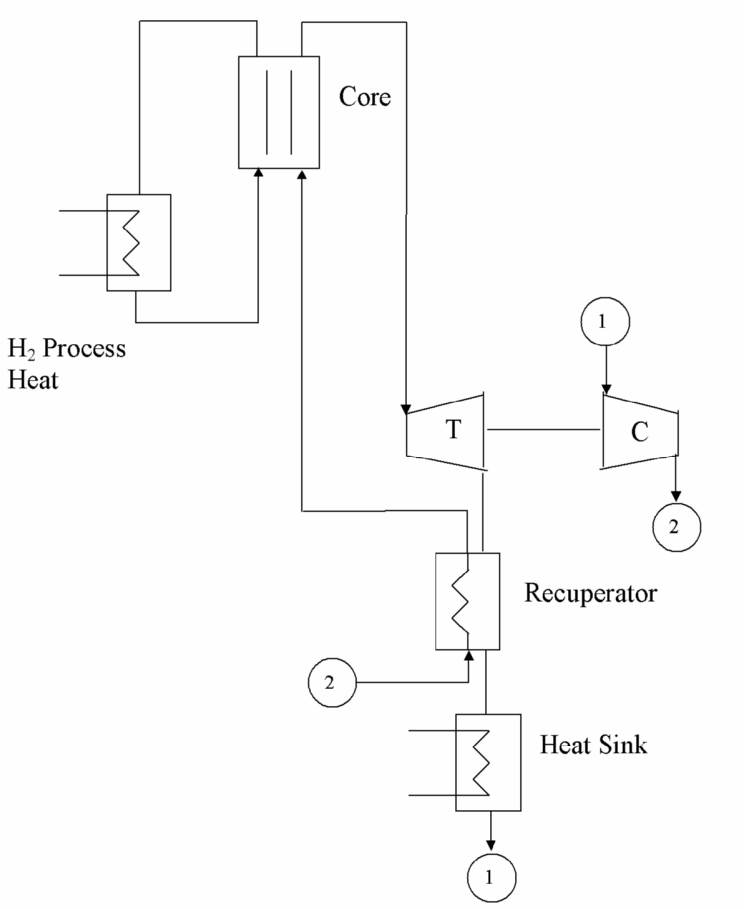

Fig. 4.1 Schematic of Equipment Layout for VHTR Co-Generation Plant

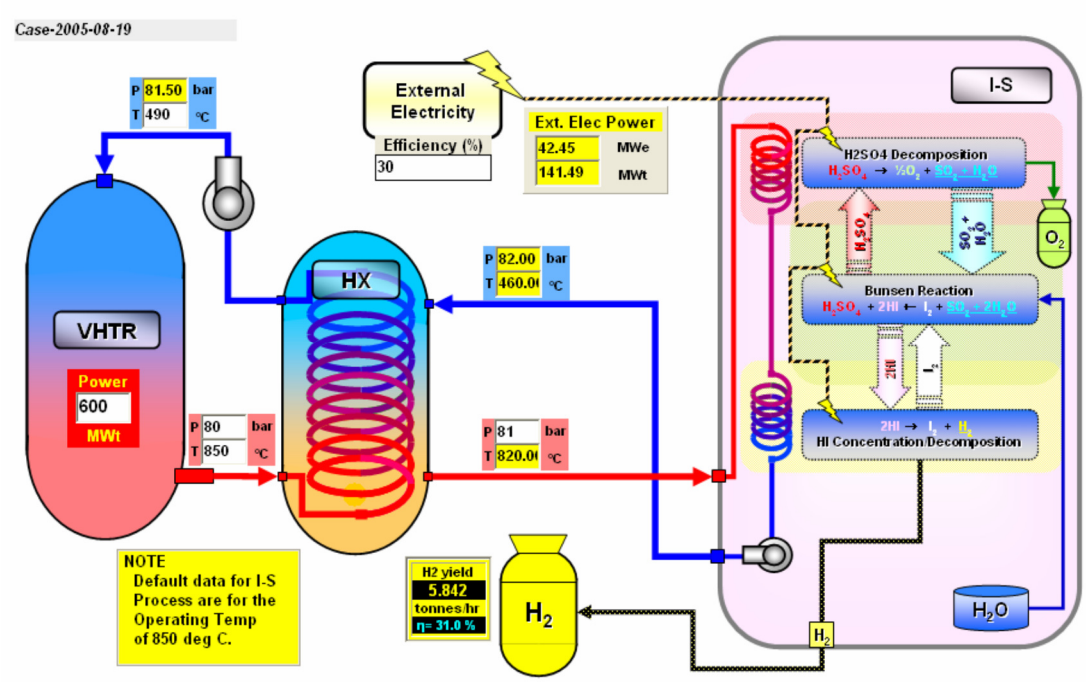

Fig. 4.2 Schematic of Equipment Layout for VHTR Hydrogen-Only Plant (from KAERI)

An upset in the hydrogen plant may also result in a change in generator electrical load if the hydrogen plant is a significant consumer of electricity as in the case of High Temperature Steam Electrolysis (HTSE).

4.3.1 Scenario and Safety Criteria

The specific set of events that gives rise to a reduction in heat utilization in the hydrogen plant is unimportant for PIRT generation. Rather, the focus is on the loss of cooling of the primary system that is communicated through the intermediate system that interfaces to the hydrogen plant. The phenomena in the primary system that determine the response are the focus of the PIRT. Over cooling events will be evaluated in the future since an overcooling initiator could also eventually lead to a trip of the hydrogen plant and thereby an undercooling event.

A loss of cooling creates an imbalance between the heat production and heat removal rates in the primary system. If the plant control system does not act to reduce core power, then the energy in the primary system will increase leading to primary system temperature increase and an increase in the pressure of the coolant. In the US design, the hydrogen plant represents a heat load of 50 MWt out of a total load of 600MWt so management of this event might be achieved through control system action alone with the plant reaching a new equilibrium condition before a reactor scram signal is generated. On the other hand in the KAERI design, loss of cooling by the hydrogen plant would result in a complete loss of heat sink and so the reactor would trip on over-temperature at the core outlet. The primary system circulator and the intermediate system circulators would also trip to prevent thermal shock in hot structures.

The key response of the reactor is an increase in temperature and pressure. The important safety limits are core outlet temperature and vessel pressure.

4.3.2 Components

The plant components participating in this event are listed in Table 4.3.

Table 4.3 Components Participating in Hydrogen Plant Upset

Systems	Components
Reactor Vessel	Inlet Plenum
	Riser
	Top Plenum and Components
	Core & Reflectors (Includes Bypass)
	Outlet Plenum and Components
Reactor Coolant Loop	Hot/Cold Pipe
	Compressor (Direct) or Circulator (Indirect)
	Intermediate Heat Exchange and Circulator
	Mixing Junction (US VHTR)
Shutdown Cooling System	Heat Exchanger and Pump

4.3.3 Phases and Phenomena

4.3.3.2 Pre Protection-System Trip Phase

The loss of heat removal by the hydrogen plant results in the hot intermediate system coolant which enters the hydrogen plant heat exchanger being returned un-cooled to the cold leg of the intermediate system. This temperature front then enters the heat exchanger that interfaces to the primary system with the result that heat removal from this heat exchanger is reduced. The temperature of the primary side coolant leaving this heat exchanger increases and in the U.S. design mixes with cooler coolant from the power conversion unit before or upon entering the reactor vessel depending on where the mixing tee is located. The mixing may cause thermal striping at the point of mixing. In the KAERI design, there is no mixing tee and the primary side coolant leaving the primary system heat exchanger enters the reactor. The reduction in primary system cooling results in reactor inlet temperature increase and negative reactivity insertion. The core power decreases and the core outlet may be temporarily overcooled. The average temperature in the high pressure side of the primary system increases as energy accumulates resulting in an increase in pressure. If the plant control system is not able to bring reactor power into balance with heat removal rate before primary system operating limits are exceeded, then the reactor will trip followed by the various circulators to avoid thermal shocking of hot structures.

4.3.3.2 Post Protection-System Trip Phase

The turbomachine and intermediate system circulators will coastdown. As normal cooling by the coolers is lost, the Shutdown Cooling System will come on-line. The upset will transition into normal plant shutdown.

The PIRTs for these three sequences follow in Tables 4.4(a) to 4.4(i). Each table is for the plant component which participates in the sequence. The ranking system used is H=high, M=medium, and a blank entry indicates low or no effect. The columns for each sequence represent the transient phases of the particular sequence.

Table 4.4 (a) PIRT for Inlet Plenum[+]

Phenomena	Water Ingress		Rod Withdrawal ATWS			H_2 Plant Upset	
	1	2	1	2	3	1	2
Flow Distribution		H	H	H		H	H
Heat Transfer (Forced Convection)		M	M	M			M
Heat Transfer (Mixed and Free Convection)							
Pressure Drop (Forced Convection)		M	H	H		H	H
Pressure Drop (Mixed and Free Convection)							
Thermal Mixing and Stratification		H					
Pressure Waves							
Thermal Shock						H	H
Two-Phase Flow		H					
Hydrolysis							

Table 4.4 (b) PIRT for Riser

Phenomena	Water Ingress		Rod Withdrawal ATWS			H_2 Plant Upset	
	1	2	1	2	3	1	2
Flow Distribution		M	M	M	M		H
Heat Transfer (Forced Convection)		M			M		M
Heat Transfer (Mixed and Free Convection)							
Pressure Drop (Forced Convection)		M	H	H	M	H	H
Pressure Drop (Mixed and Free Convection)							
Radiation Heat Transfer		H		M	H		
Gas Conduction					M		
Hydrolysis of Graphite							
Two-Phase Flow		H					
Thermal Shock						H	H

[+]H = High
M = Medium
- = Low/No Effect

Table 4.4 (c) PIRT for Table for Top Plenum & Components

Phenomena	Water Ingress		Rod Withdrawal ATWS			H_2 Plant Upset	
	1	2	1	2	3	1	2
Flow Distribution		H	H	H	M	H	H
Heat Transfer (Forced Convection)				M	M		M
Heat Transfer (Mixed and Free Convection)							
Pressure Drop (Forced Convection)			H	M	M	H	M
Pressure Drop (Mixed and Free Convection)							
Thermal Mixing and Stratification					M	H	H
Hot Plumes					H		
Fluid Properties				M			
Thermal Resistance/Heat Capacity of Shroud					H		
Hydrolysis of Graphite							
Pressure Waves							
Two-Phase Flow		M					
Thermal Shock						H	H

Table 4.4 (d) PIRT for Core and Reflector (including Bypass)

Phenomena	Water		Rod Withdrawal			H_2 Plant	
	1	2	1	2	3	1	2
Flow Distribution	H	H	H	H	H	H	H
Heat Transfer (Forced Convection)	H		H	H	H	H	H
Heat Transfer (Mixed and Free Convection)							
Pressure Drop (Forced Convection)	M		H	M	H	H	M
Pressure Drop (Mixed and Free Convection)							
Initial Stored Energy				H			H
Power Distribution			H	H	H	H	H
Decay Heat (including Power Distribution)	H	H		H	H		H
Reactivity Feedback			H	H	H	H	
Xenon Concentration			H	H	H		
Control Rod Worth and Gradient			H	H	H		
Space-Time Kinetics			H	H	H		
Fuel/Reflector Conductivity	M	H	M	M	H	M	M
Fuel/Reflector Specific Heat	M	H	M	M	H	M	M
Multi-D Heat Conduction Including Contact	H	H	M	H	H	M	H
Gas Conduction (Including Gaps)		M			M		
Radiation Heat Transfer		H			H		
Hydrolysis of Graphite		H					
Fluid Properties							
Core Configuration							
Pressure Waves							
Two-Phase Flow		H					

Table 4.4 (e) PIRT for Outlet Plenum & Components

Phenomena	Water Ingress		Rod Withdrawal ATWS			H_2 Plant Upset	
	1	2	1	2	3	1	2
Flow Distribution	H		H	H	H	H	H
Heat Transfer (Forced Convection)	M		H	M	M	H	M
Heat Transfer (Mixed and Free Convection)							
Pressure Drop (Forced Convection)	M		H	M	M	H	M
Pressure Drop (Mixed and Free Convection)							
Thermal Mixing and Stratification	H				H		
Jet Discharge	M		H			H	
Thermal Striping	M		H			H	
Hydrolysis of Graphite							
Fluid Properties	M						
Pressure Waves							
Two-Phase Flow	H						

Table 4.4 (f) PIRT for Reactor Vessel Lower Head

Phenomena	Water Ingress		Rod Withdrawal ATWS			H_2 Plant Upset	
	1	2	1	2	3	1	2
Heat Capacity of Lower Head and Internals	H						
Heat Transfer	H						
Cooling by Latent Heat of Vaporization							

Table 4.4 (g) PIRT for Intermediate Heat Exchanger and Circulator

Phenomena	Water Ingress		Rod Withdrawal ATWS			H_2 Plant Upset	
	1	2	1	2	3	1	2
Heat Transfer						H	H
Pressure Drop						H	H
Circulator Characteristics						H	H

Table 4.4 (h) PIRT for Co-Generation Mixing Junction

Phenomena	Water Ingress		Rod Withdrawal ATWS			H_2 Plant Upset	
	1	2	1	2	3	1	2
Thermal Striping						H	H

Table 4.4 (i) PIRT for Pressure Boundary

Phenomena	Water Ingress		Rod Withdrawal ATWS			H_2 Plant Upset	
	1	2	1	2	3	1	2
Water Vapor Partial Pressure	H	H					
Mass and Energy Loss through Relief Valve	H	H					

Table 4.4 (j) PIRT for Hot/Cold Pipe

Phenomena	Water Ingress		Rod Withdrawal ATWS			H_2 Plant Upset	
	1	2	1	2	3	1	2
Heat Transfer (Forced Convection)	M		H	M		H	M
Heat Transfer (Mixed and Free Convection)							
Pressure Drop (Forced Convection)	M			M			M
Pressure Drop (Mixed and Free Convection)							
Pipe/Insulator Conduction							
Critical Flow							
Pressure Waves							

Table 4.4 (k) PIRT for RCCS (Reactor Cavity Cooling System) Reactor Cavity

Phenomena	Water Ingress		Rod Withdrawal ATWS			H_2 Plant Upset	
	1	2	1	2	3	1	2
Flow Distribution		H			H		
Heat Transfer (Mixed and Free Convection)		H			H		
Pressure Drop (Mixed and Free Convection)		M			M		
Radiation Heat Transfer		H			H		
Gas Conduction		H			M		
Conduction to Ground		H			M		
Dust from Core		M					
Air Purge and Gas Species Distribution		H					
Confinement Valve and Filter Characteristics		H					
Pressure Waves							

Table 4.4 (l) PIRT for RCCS Tube (Air Duct)

Phenomena	Water Ingress		Rod Withdrawal ATWS			H_2 Plant Upset	
	1	2	1	2	3	1	2
Heat Transfer (Forced Convection)		H			H		
Heat Transfer (Mixed and Free Convection)		H			H		
Pressure Drop (Forced Convection)		H			H		
Pressure Drop (Mixed and Free Convection)		H			H		
Radiation Heat Transfer		H			H		
Fluid Properties (humidity)		M			M		

Table 4.4 (m) PIRT for RCCS Piping and Chimney

Phenomena	Water Ingress		Rod Withdrawal ATWS			H_2 Plant Upset	
	1	2	1	2	3	1	2
Heat Transfer (Mixed and Free Convection)		M			M		
Pressure Drop (Mixed and Free Convection)		H			H		
Flow Mixing in Piping Plenums		M			M		
Buoyancy Flow in Chimney		H			H		
Pressure Waves		M			M		

Table 4.4 (n) PIRT for Power Conversion Unit

Phenomena	Water Ingress		Rod Withdrawal ATWS			H_2 Plant Upset	
	1	2	1	2	3	1	2
Turbine Performance	H		H	H		H	H
Turbine Valve Performance	H		H	H		H	H
Heat Conduction in Thick-Walled Structure			H				
Heat Transfer in Coolers	M		H			H	
Pressure Drop in Coolers	M		H			H	
Water Vapor Condensation in Coolers	H						
Heat Transfer in Recuperator			H			H	
Pressure Drop in Recuperator	M		H			H	
Compressor Performance	H		H	H		H	H
Pressure Waves							
Entrainment of Condensed Water	H						

Table 4.4 (o) PIRT for Shutdown Cooling System

Phenomena	Water Ingress		Rod Withdrawal ATWS			H_2 Plant Upset	
	1	2	1	2	3	1	2
Tube Leak Flow Regime	H	H					
Back Pressure in Water Cooling Circuit	H	H					
Circulator Performance	H	H		H	H		H
Heat Exchanger Performance				H	H		H

References

4.1 P.G. Kroeger, "Safety Evaluation of MHTGR Licensing Basis Accident Scenarios," NUREG/CR-5261 and BNL-NUREG-52174, April 1989.

4.2 D.A. Copinger and D.L. Moses, "Fort Saint Vrain Gas Cooled Reactor Operational Experience," ORNL/TM-2003/223, September 2003.

4.3 R.B. Vilim, E.E. Feldman, W.D. Pointer, and T.Y.C. Wei, "Initial VHTR Accident Scenario Classification: Models and Data," ANL-GenIV-057, May 2005.

4.4 P.G. Kroeger, "Bounding Core Temperature Transients for Severe and Rapid Water Ingress Scenarios in Modular High Temperature Gas-Cooled Reactors," Sixth Proceeding of Nuclear Thermal Hydraulics, American Nuclear Society, 1990, p.263-273.

4.5 O.L. Smith, "Magnitude and Reactivity Consequences of Moisture Ingress into the Modular High-Temperature Gas-Cooled Reactor Core," NUREG/CR-5947, November 1992.

4.6 M.W. Cappiello, "The Effect of Water Vapor in the Reactor Cavity in a MHTGR on the Radiation Heat Transfer," American Nuclear Society International Topical Meeting, Portland, Oregon, July 1991.

4.7 Gas Turbine-Modular Helium Reactor (GT-MHR) Conceptual Design Description Report, 910720, Revision 1, GA Project No. 7658, General Atomics, July 1996.

4.8 D.A. Copinger and D.L. Moses, "Fort Saint Vrain Gas Cooled Reactor Operational Experience," ORNL/TM-2003/223, September 2003.

4.9 S. Ball, personal communication, April 2006.

4.10 S. Ball, personal communication, December 2005.

5.0 Core Flow Modeling and Sensitivity Calculations

Long-term fuel integrity and efficient utilization of fuel thermal capability require careful control of coolant temperatures in the core. Since temperatures are a function of the distribution of coolant, uncertainty in core cooling distribution leads to uncertainty in peak fuel temperature and has as a direct consequence, either a design-based derating of the core or, potentially, an increase in the fraction of fuel microspheres that fail during upset conditions. Further, precise prediction of coolant allocation permits a more uniform core radial temperature distribution to be achieved thereby minimizing temperature-gradient induced long-term deformation of the graphite elements. Such deformation leads to coolant misallocation over life further compounding the adverse dependence of coolant viscosity on temperature and its effect on coolant distribution.

5.1 PMR Core Flow Distribution Study

One of the largest uncertainties associated with managing PMR core temperatures is that fraction of coolant that bypasses fueled regions by way of leakage paths. Basic to a proper accounting of the long-term effects of coolant leakage on core temperature distribution is the need for fundamental data and understanding of the deformation behavior of graphite in sustained temperature and neutron fields. Experimental results for graphite deformation are needed for development and calibration of models for predicting geometry change over life. These models are to provide input to thermal-hydraulics codes needed for reliable prediction and control of core coolant distribution through life. Knowing the sensitivity of flow through the various leakage paths due to local graphite deformation can serve as a guide to selection of experiments.

For the case of the PMR, the major potential parallel flows to the downward axial flow through the coolant holes in the core fuel blocks are: (a) the holes in the core blocks designed for the control rods, (b) the flow between the blocks in a column stack. Surfaces are not perfectly smooth. At BOL, there is manufacturing finish to consider, and over life, deformation due to irradiation swelling and thermal cycling. Wedge-shaped gaps between the top and bottom faces of the graphite blocks have been included in leakage studies; and (c) without appropriate design seals, the inter-column gap would also be a major bypass leakage flow path for the core coolant. For the HTTR, wedge-type seals have been considered for sealing applications at the core support structure. The leakage through these seals specifically developed by the designers to be placed in the inter-column gaps (between the columns) then constitutes the bypass flow in this gap region.

Given this flow geometry, the major factors in determining the core leakage flow are: (i) the geometry resistances to the flow through the control rod holes, (ii) design seal behavior in the column-to-column gaps at the core support interface, (iii) block-to-block stacking surface fit, and (iv) column-to-column gap history during core life. The sensitivity (perturbation) calculations presented in this section evaluate these factors.

In summary, the results of the sensitivity calculations presented in this section show that the greatest sensitivity is presented by factor (ii), the behavior of the design

seal at the core support structure. Next in importance is factor (iii) for block elements at the core periphery. The other factors are much less significant in comparison to these two. Details follow below.

5.1.1 Core Layout and Coolant Allocation

In addition to providing for the removal of the heat of fission in the active region of the core in a safe and efficient manner, provision must also be made for cooling of reflector regions and control assemblies in the core. The layout of these regions in the GT-MHR design is shown in Fig. 5.1. There are four types of elements that make up the core: the fuel element shown in Fig. 5.2, the fuel control element (reserve shutdown and startup) shown in Fig. 5.3, reflector control element shown in Fig. 5.4, and the solid reflector element. A main design task is to apportion the available coolant among these different element types in the most efficient manner, which essentially amounts to ensuring no element is overcooled. An element will be overcooled when it receives more coolant than needed to ensure structural integrity over life. At a particular lattice position the column is composed of stacked elements all of the same type.

A major design decision is to choose between orificing zones to control coolant allocation among regions or relying on power-profile management. In the former case, flow restrictions built into each column of elements throttle flow so that each column is optimally cooled. In the latter case, the flux shape is managed over time so that the local power production results in optimal temperatures in a column. The flow through the column is a function of the geometry of the element that makes up a column. To manage this flow the designer has some flexibility in choosing the number and diameter of cooling channels that run the vertical length of an element. Disadvantages associated with coolant allocation by orificing include the possibility of misplaced fuel elements, cracking of fuel elements by lateral pressure gradients, and increased loop pressure drop. The latter adversely impacts Brayton cycle efficiency in direct cycle plants. Disadvantages of power-profile management include the potential need for greater fuel element shuffling to achieve a core temperature distribution comparable to that achievable by orificing.

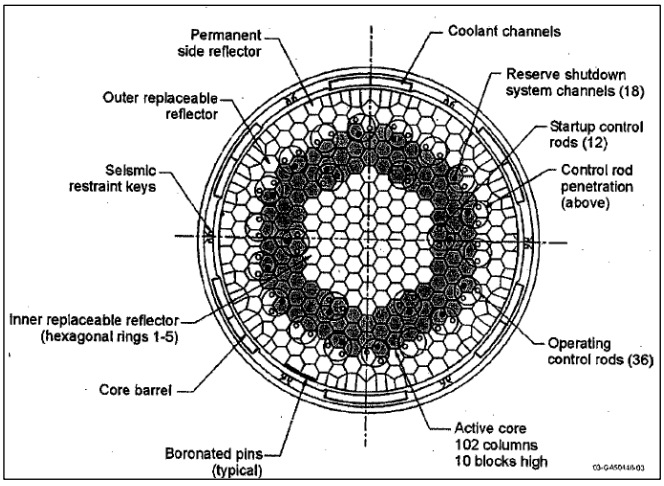

Fig. 5.1 GT-MR Core Layout

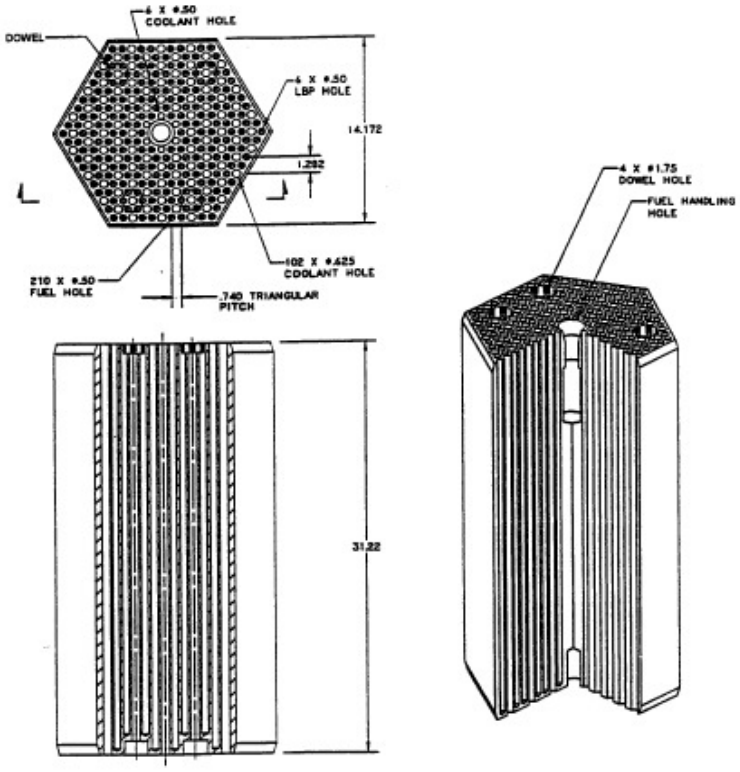

Fig. 5.2 Fuel Element

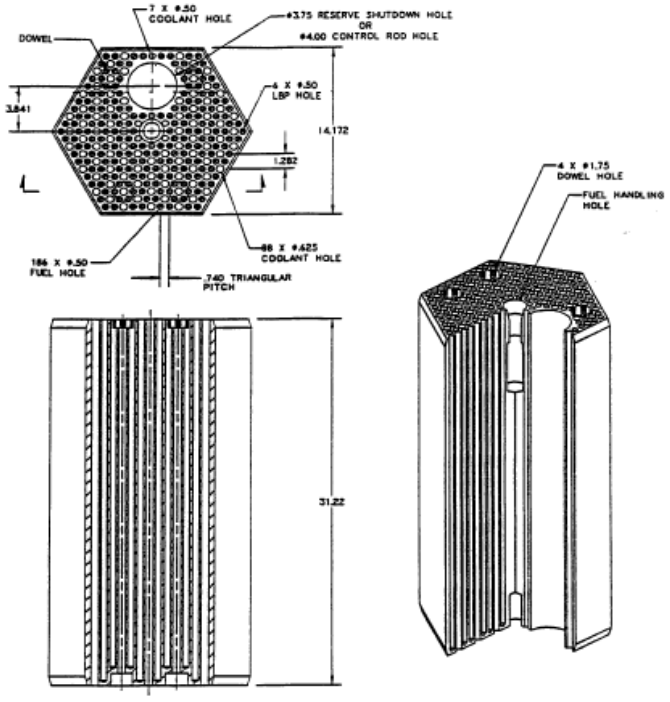

Fig. 5.3 Fuel Control Element

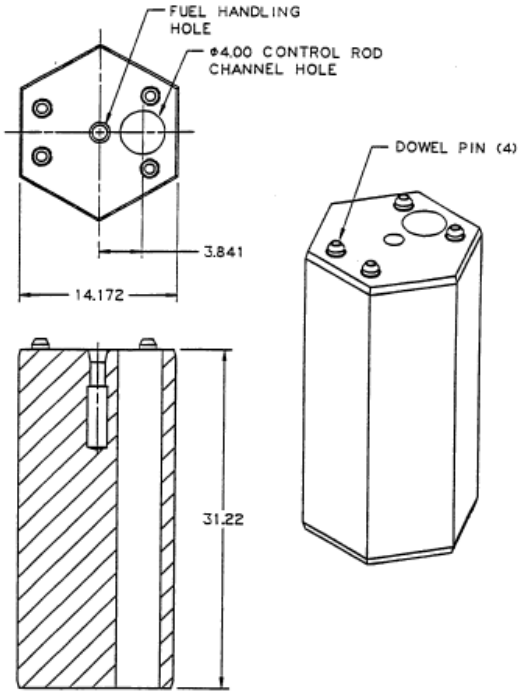

Fig. 5.4 Reflector Control Element

Core temperature control by power-profile management rather than orificing appears to be the current trend in gas reactor design. [5.1,5.2] Means of controlling the power distribution in the core include fuel element shuffling as a function of burnup, multiple enrichment zones, burnable poisons, and control rod power shaping. With the shuffling of fuel elements the possibility for power-to-flow mismatches exists. However, there are a number of means for detecting the consequences of a misplaced element including column exit thermocouples, monitoring for fission product release, detecting local flux perturbations, and element specific gas tagging. In this work, we assume power-profile management.

5.1.2 Phenomena Giving Rise to Leakage and Its Uncertainty

The most important effect leading to uncertainty in core coolant flow distribution appears to be uncertainty associated with dimensions of coolant flow paths. These can take the form of manufacturing tolerances and result in leakage sites where the leakage flow is not well characterized. Part of the problem is that graphite structures that interface to one another often involve a dry fit where the only engineered force constraining the fit is gravity. Stacked elements are an example. The gap size between two stacked elements depends on the tolerances the two faces have been machined to and local asperities related to surface finish. The elements in turn are subject to somewhat random forces (but of limited magnitude) exerted by neighboring elements with only the force of gravity serving as the engineered force to constrain the position of an element. While there may be a core restraint system, it typically constrains through periphery columns so the behavior of interior columns is subject to local inter-column gaps that has a component that depends only weakly on the core restraint system.[5.3] Another instance is the

graphite seal where an inter-column gap meets the core support blocks. These seals again rely on a dry fit, and their position appears to be constrained only by the weight of structures above. These seals are critical for minimizing leakage from these gaps into the outlet plenum.

The uncertainty in the dimensions of coolant flow paths can also take the form of uncertainty arising with the long-term distortion of core components. Such changes are pronounced at locations where there is a steep gradient in the temperature or neutron fluence with respect to position. A change in geometry can create leakage paths that reroute coolant that would otherwise pass through the core. Specific instances include geometry change in the stacked elements and gap seals cited above. Other instances are life-cycle induced cracks in elements and changes in flow area where control assemblies penetrate control rod holes in fuel control elements. Uncertainty in the prediction of dimensions has two components. First is that associated with the analytical methods for predicting the local fluence and temperature field. Second is the deformation response of the material. This depends on the properties of the graphite which in turn strongly depend on the specific blend of carbon used and the preparation method employed.[5.4] The literature suggests good properties characterization of the specific graphite used is a requirement for good analytic prediction of deformation response. Also under material properties is porosity. Coolant flowrate from coolant channels to inter-column gaps through pores in the graphite is a function of the material porosity.

The gas reactor literature describes some classic cases of deformation of graphite structures that lead to coolant leakage. The first is the opening of wedge-shaped gaps between stacked elements [5.2,5.5 - 5.8]. This effect is driven by either temperature or fluence gradients which give rise to differential thermal expansion and swelling of graphite. These gradients are steepest at the core periphery where the last row of fuel elements meets the first row of reflector elements. The second is deformation of the core support blocks upon which the core columns stand. [5.9 - 5.11] Openings in these seals can cause leakage of coolant from the inter-column gaps into the outlet plenum bypassing fuel element coolant channels.

The literature also identifies design approaches for minimizing these deformations and their effects. Thermally-induced deformations can be minimized by maintaining a flat temperature profile across the core in the radial direction through application of power-profile management strategies. [5.1] This same approach can be used to manage fluence-induced deformation. To minimize the effect of coolant leakage due to seal deformation, one can choose a seal geometry that is inherently less prone to leak with deformation of the graphite. An example using wedge-shaped seals is described in [5.11].

5.1.3 Core as a Two-Dimensional Array of Elements

There are two main spatial dependencies that determine the flow distribution in the core. The first is a local dependency, the type of element present at a column position. The second is a global dependency, the ordering of element types as one moves radially outward across columns starting at the core center and terminating at the outer reflectors.

There does not appear to be a strong azimuthal component to the flow conditions in any particular column type. These conclusions were drawn as follows. Figure 5.1 shows the GT-MHR core layout, also adopted for the NGNP. Column orificing is not used. In this core design, a 120 degree symmetry section of active columns is shown in Fig. 5.5. Each of the letters A and B denote column refueling where one-half the fuel columns are replaced at each refueling. If one examines the upper half of this figure, one sees a repetition of two two-dimensional fuel element arrays. A similar type of repetition appears in the lower half of Fig. 5.5. We approximate the repetition seen in the upper half by the rendering in Fig. 5.6 that shows these two arrays alternating to infinity.

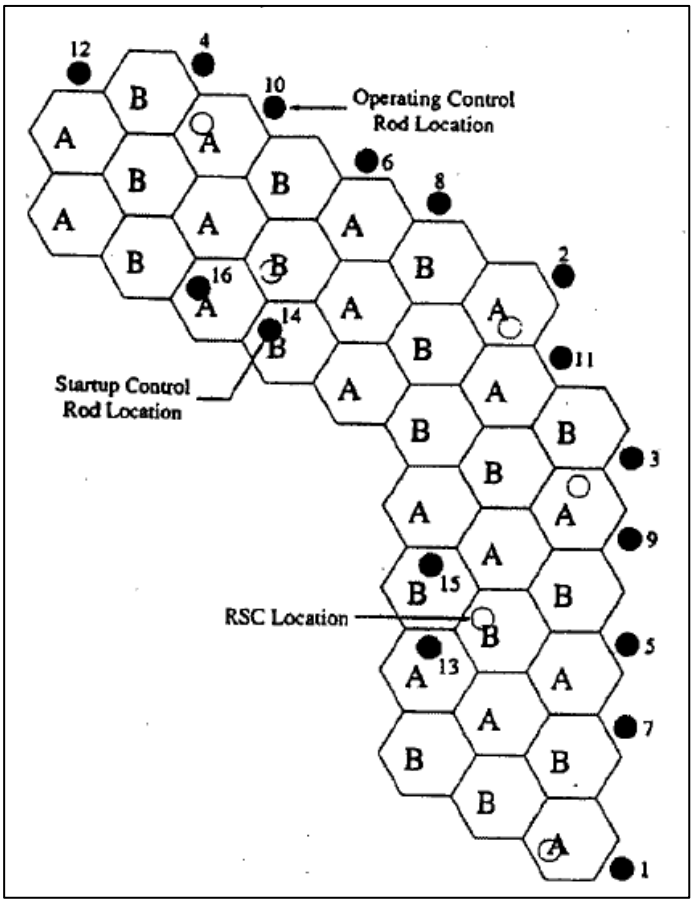

Fig. 5.5 Active Core Symmetry Section for GT-MHR

A second premise is that lateral flow interaction between these two adjacent two-dimensional fuel arrays (shown in bold in Fig. 5.6) can be ignored without significant consequence since the interaction is small compared to interaction between columns in the radial direction. Columns opposite one another in the two alternating arrays have differing powers but there does not appear to be a mechanism whereby this difference can significantly affect hydraulics. The channel axial coolant temperature profile will differ between opposite columns but this will not appreciably affect the channel pressure drop and hence the stacked element interface leakages. The columns are not orificed so the frictional resistance in coolant channels between opposite columns will be the same so there is no potential for cross-flow leakage between the two arrays. Essentially as we

move across these arrays in Fig. 5.6 in what was the azimuthal direction the same type of element is encountered. But if we move radially outward we first encounter reflector elements, then fueled elements, then reflector elements. The differing flow characteristics of each of these element types will give rise to a global flow distribution that has a radial dependence, both interior to the elements and in the gaps between elements. This dependence will be made stronger by the expected creation of a wedge-shaped gap between two stacked elements at locations in the core where fueled elements meet outer reflector elements. The gap will arise as a result of the steep temperature and fluence gradient there as described earlier. As a consequence, the interaction of flows among elements is well approximated by the arrows in Fig. 5.7. Essentially, the hydraulic solution for each of the two types of two-dimensional element arrays shown there, and the individual solution component flows by element type, can be taken as representative for the whole core.

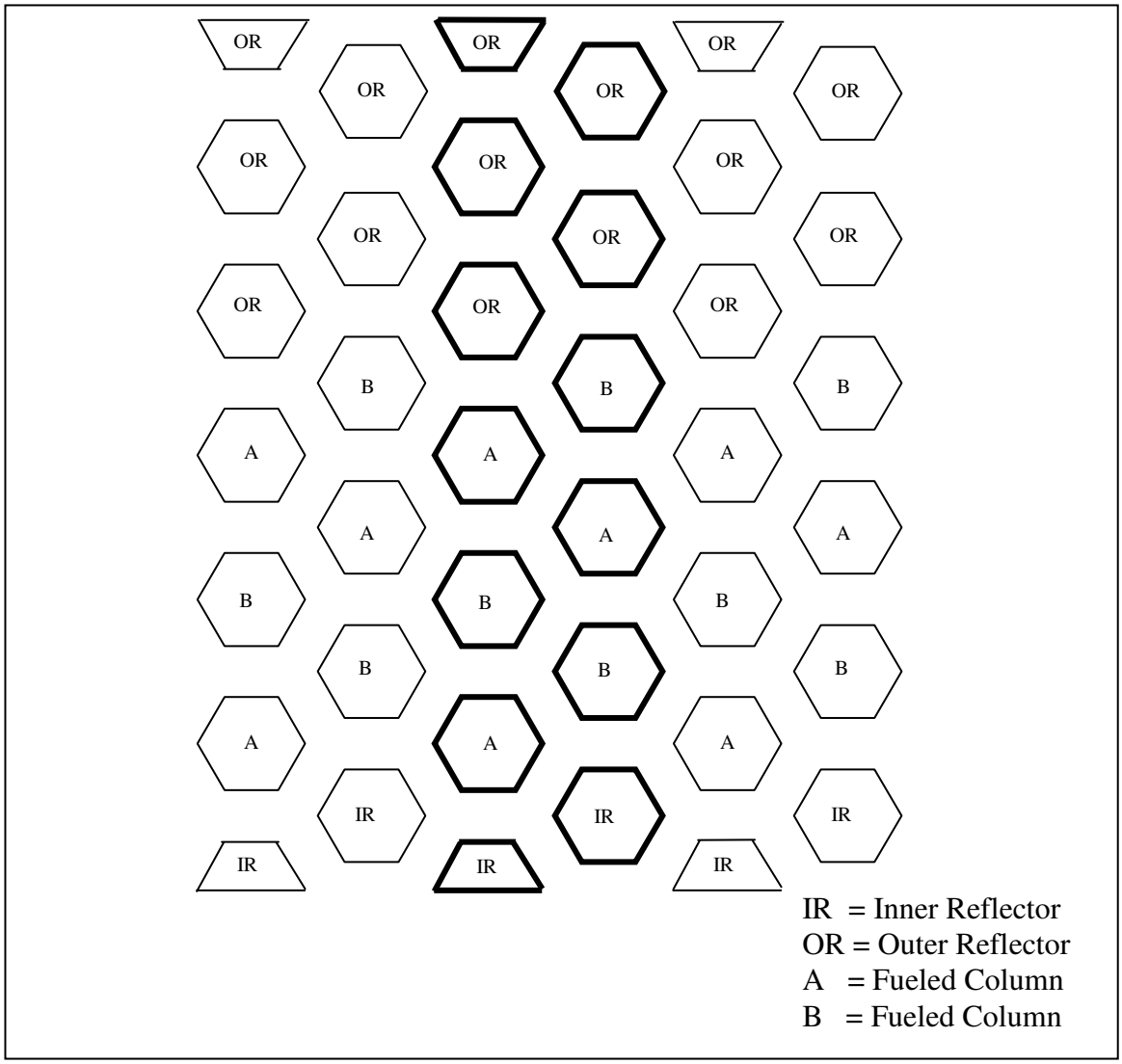

Fig. 5.6 Idealization of Core as Two Alternating Two-Dimensional Arrays of Elements. Unique arrays are identified in bold.

Given these alternating arrays of elements whose individual element solution is representative of core-wide elements, additional details can be added to reflect features not described above. There are variants on the basic reflector and control elements that give rise to four types of elements. These are represented in Fig. 5.8 in numbers in proportion to their appearance on an average core-wide basis as established in Table 5.1. They have also been ordered to reflect the core wide spatial arrangement of such assemblies. That is solid reflector elements in the core interior, three successive fuel elements with the last having a control rod hole, and finally at the core periphery a solid reflector control element with a control rod hole.

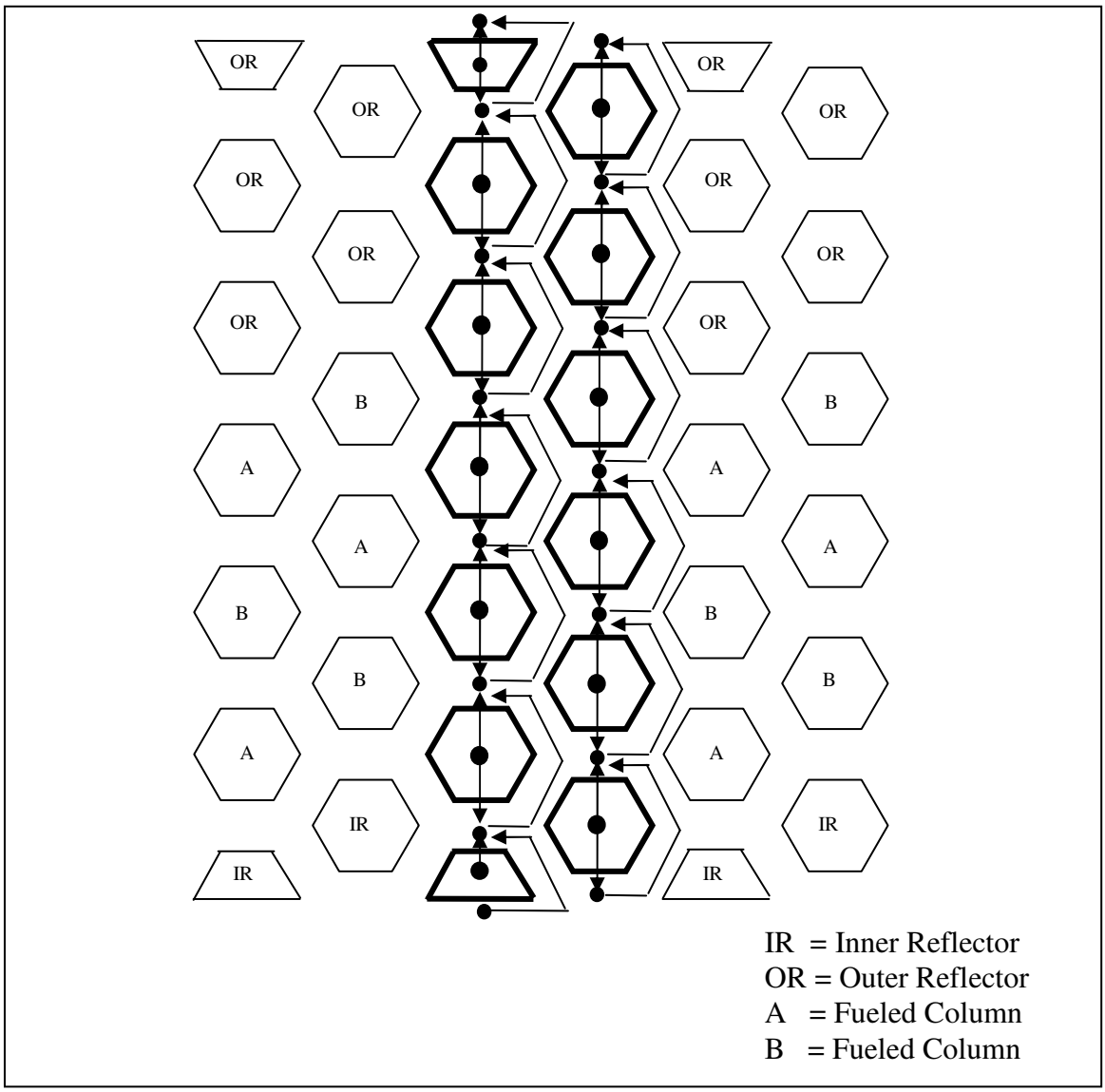

Fig. 5.7 Coolant Nodes and Flow Paths for Core Approximated by Two Alternating Two-Dimensional Arrays of Elements

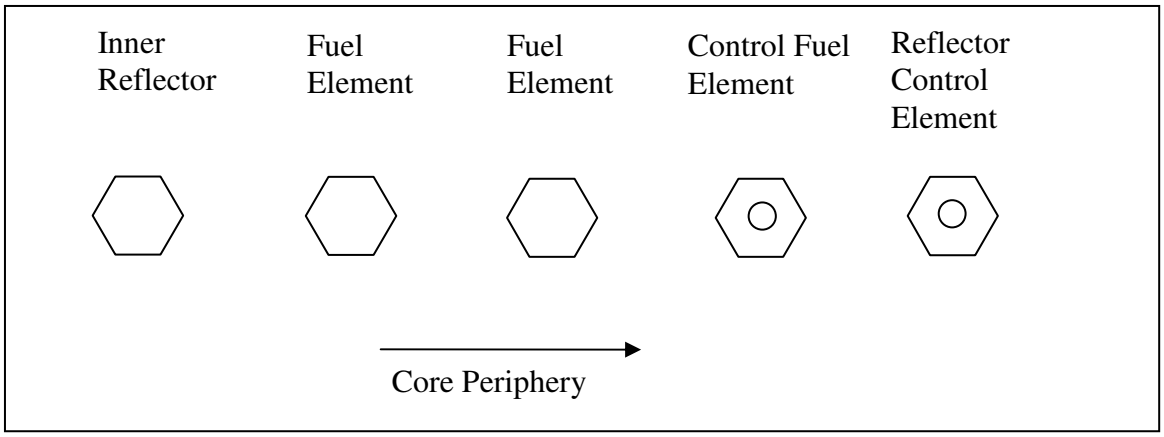

Fig. 5.8 Top View of Representative Row of Reactor Columns (see Table 5.1)

Table 5.1 Basis for Assumed Representative Row of Columns *

Element Type	Fractional Number	Number in Representative Row
Fuel Element	72/138= 0.52	2
Control Fuel Element (Reserve Shutdown and Startup Control Rods)	30/138=0.22	1
Reflector Control Element (Operating Control Rods)	36/138= 0.26	1

* Data from GT-MHR Design Description, General Atomics, 1996 [5.13]

5.1.4 Flow Distribution Model

The distribution of flow among block elements is governed by several important phenomena. Provision for representing them has been made in the model we have developed. Briefly, these phenomena include:

- Leakage from the coolant channels interior to two stacked elements laterally through the interface gap that separates the two, into the inter-column gap.
- Increased lateral leakage for fueled columns at the periphery of the core compared to interior columns by means of element-by-element specification of pressure loss coefficients.
- Leakage from the coolant channels interior to two stacked fuel control elements through the interface gap that separates the two into the control rod hole.
- Lateral flow between the inter-column gaps of neighboring columns.

- Either a flow or pressure boundary condition for the coolant channel, gap channel, and control-hole channel of each element at both the inlet and outlet of the core.

The provision for a flow boundary condition above permits representation of control rods at the inlet and seals at the outlet to be represented without explicit knowledge of their pressure loss characteristics. This also allows the consequences of seal effectiveness to be investigated parametrically. In addition to the phenomena above the usual axial Fanning friction losses in coolant, control rod hole, and inter-column gap channels are also represented.

The distribution of flow amongst the two-dimensional array of elements is represented by a network of interconnected unit block elements. The generic individual unit block element is shown in Fig. 5.9 and defines the various flows represented in the model. These flows combine and split at various locations in the core as described earlier. In the model this is assumed to occur at mass nodes whose locations in the unit block elements are shown as solid discs in Fig. 5.10.

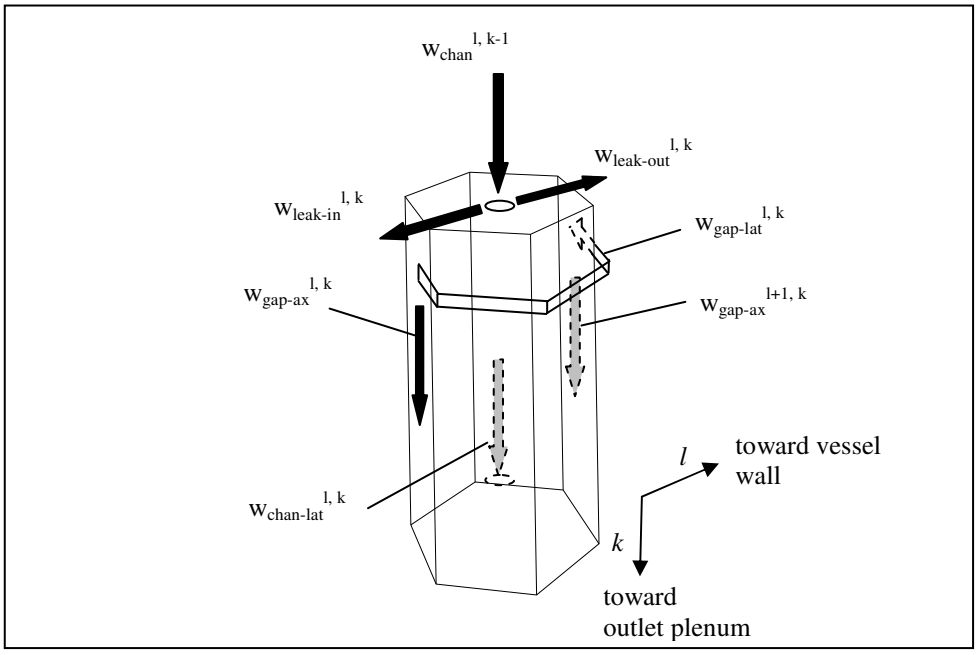

Fig. 5.9 Coolant Paths Through and Around an Element

It is assumed that flow paths couple mass nodes and that each of the flows shown in Fig. 5.9 is assumed to exit a node and re-enter a node without interacting with other flows.

Conservation of momentum governs the flow in each of these paths balancing frictional losses with change in pressure. This is depicted in Fig. 5.11 in a unit flow-pressure loop network where pressures are defined at the nodes and frictional losses are represented by resistances between nodes. The solid lines indicate where the mass and

momentum balances around an element are taken. The network repeats for blocks above and below and for blocks to either side. The dashed lines in the figure represent flow paths on adjacent unit networks. Figure 5.10 and 5.11 also define the node labeling scheme. Index *k* represents the block axial level and increases in the downward direction while index *l* represents the column number and increases radially outward.

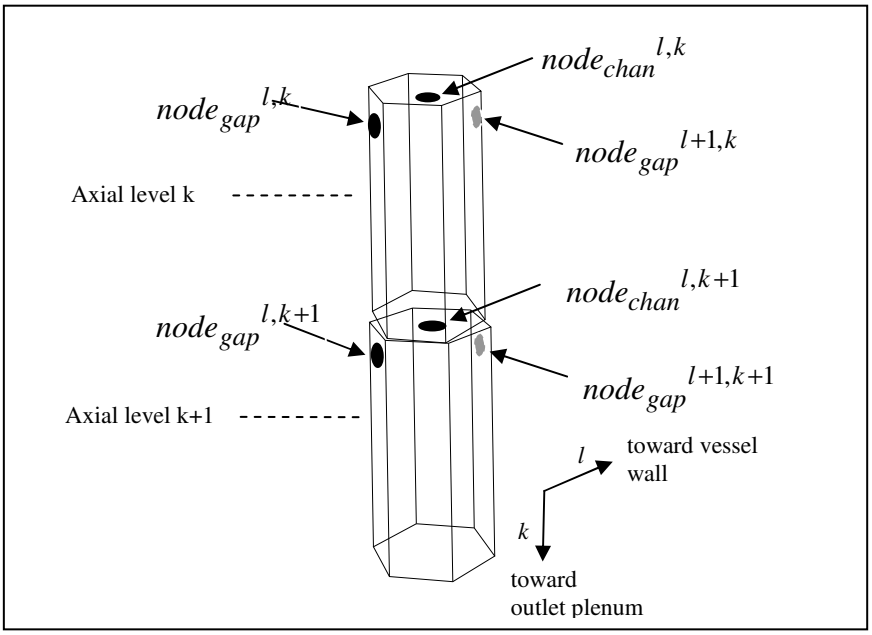

Fig. 5.10 Coolant Mixing Nodes for Elements

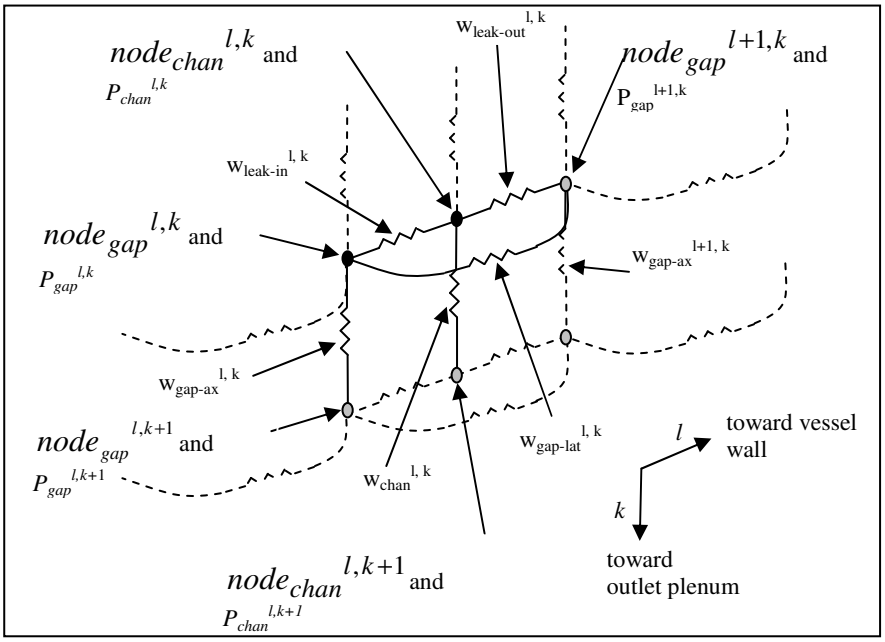

Fig. 5.11 Network Representation of Mass Nodes, Coolants Flowpaths, and Pressures. Unit network denoted by lines and nodes drawn in bold.

This network representation of the PMR core flow distribution model has been implemented in the GAS-NET code. Details of the code are available in Appendix I. GAS-NET has been used to perform the PMR sensitivity calculations outlined in the following sections.

5.1.5 Base Case

A reference case is defined for the sensitivity calculations. It provides a baseline against which the effect of variations in parameters of interest can be compared and sensitivities determined. For the reference case, the GT-MHR core is adopted with [5.13] serving as the source of basic engineering data. This document was used to identify the types of elements present in the core, the dimensions of the elements, and their arrangement in the core. This document is also used to determine the geometric details of the flow paths that bypass coolant around coolant channels in fueled elements. These flowpaths were identified above under the heading *Constitutive Equations*. Some engineering parameters do not have values given in [5.13]. These parameters include the inter-column gap thickness at full power operation, the nominal gap thickness of the interface between two stacked elements, and the dimensions of the wedge-shaped gap that evolves from this over time during operation at power. Means for estimating their values are described below.

For the base case it is assumed the distribution of coolant among the different elements in the core is given by the equivalent core representation shown in Fig. 5.7. The rationale for this representation was given in Section 5.1.3 under the heading *Core as a Two-Dimensional Array of Elements*. Each column in Fig.5.8 is assumed to consist of ten stacked elements with each element having the same length as in the GT-MHR. The definition of the base case is completed by specifying the values for loss coefficients in each of the flowpaths in each unit network associated with each element in Fig. 5.8 and by specifying the boundary conditions that drive the flow through the network of elements that represents Fig. 5.8.

The values for loss coefficients in the base case along with the engineering data used to derive these values are given in Tables 5.2 through 5.8. These tables reference the equations for loss coefficients presented in Appendix I. The loss coefficient for the axial coolant channels in a fuel element and in a control fuel element are given in Table 5.2 and appear in the coolant channel axial momentum balance of Eq. (I.7). The loss coefficient for flow through a control rod hole is given in Table 5.2a. The loss coefficient for flow down the gap between two adjacent columns on a per element basis is given in Table 5.3 and appears in the gap axial momentum balance of Eq. (I.3). The value is based on an inter-column gap thickness derived in Table 5.4 for the hot at beginning-of-life condition and assumes a value for the cold condition provided by [5.14]. The value obtained for the hot condition is very close to that given by General Atomics in Fig. 5.12. The loss coefficient for lateral flow through the inter-column gap is given in Table 5.5 and appears in the gap lateral momentum balance of Eq. (I.4). The calculation is for the shaded region in Fig. I.3 which takes in four element faces.

Table 5.2 Axial Loss Coefficient for Coolant Channels in a Fuel Element and in a Control Fuel Element per Element

	Fuel Element	Control Fuel Element
Reference	Eq. (I.7b)	Eq. (I.7b)
Number of coolant channels, N_{chan}	102+6=108	86+7=93
Coolant channel diameter, D_{chan} (m)	0.625*2.54e-2	0.625*2.54e-2
$A_{chan} = N_{chan}\ \Pi/4\ D_{chan}^{\ 2}$ (m^2)	2.14e-2	1.84e-2
$P_{w\text{-}chan} = N_{chan}\ \Pi\ D_{chan}$ (m)	5.39	4.64
$D_{h\text{-}chan} = 4\ A_{chan} / P_{w\text{-}chan}$ (m)	1.59e-2	1.59e-2
L_{chan} (m)	0.793	0.793
C, n	0.184, 0.2	0.184, 0.2
ρ (kg/m^3) @ (485+850)/2 C and 7.0 MPa	3.3	3.3
μ (Pa-s) @ (485+850)/2 C and 7.0 MPa	45e-06	45e-06
K_{chan}, loss coefficient per fuel element per Eq. (I.7b)	437	572

Table 5.2a Axial Loss Coefficient for Control Rod Hole in a Control Fuel Element and in a Control Reflector Element per Element

Reference	Eq. (I.10b)
Number of coolant channels, N_{chan}	1
Coolant channel diameter, D_{chan} (m)	4.0*2.54e-2
$A_{cntrl} = N_{chan}\ \Pi/4\ D_{chan}^{\ 2}$ (m)	8.10e-3
$P_{w\text{-}cntrl} = N_{chan}\ \Pi\ D_{chan}$ (m)	0.320
$D_{h\text{-}cntrl} = 4\ A_{chan} / P_{w\text{-}chan}$ (m)	0.102
L_{cntrl} (m)	0.793
C, n	0.184, 0.2
ρ (kg/m^3) @ (485+850)/2 C and 7.0 MPa	3.3
μ (Pa-s) @ (485+850)/2 C and 7.0 MPa	45e-06
K_{cntrl}, loss coefficient per control rod hole per element per Eq. (I.10b)	270

Table 5.3 Axial Loss Coefficient for Inter-Column Gap per Element

Reference	see Figure 5.9 and 5.11 and Eq. (I.3b)
f , column face width (m)	14.171/2/cos 30^o *2.54e-02=0.208
g, inter-column gap width (m) (at temp.)	3.80e-03 (Table 5.7)
$A_{gap\text{-}ax}$ (m)	2.40e-03
$P_{w\text{-}gap\text{-}ax}$ (m)	1.25
$D_{h\text{-}gap\text{-}ax}$ (m)	7.60e-3
L_{ax} (m)	31.22*2.54e-02=0.793
C, n	0.184, 0.2
ρ (kg/m^3) @ (485+850)/2 C and 7.0 MPa	3.3
μ (Pa-s) @ (485+850)/2 C and 7.0 MPa	45e-06
$K_{gap\text{-}ax}$, axial loss coefficient per inter-column gap per element per Eq. (I.3b)	5.50e4

Table 5.4 Average Inter-Column Gap in Prismatic Core

Estimate from Thermo-Physical Properties (BOC)	Gap at Cold Condition [a] (m)	0.04*2.54e-02=1.0e-03 (=0.04 inches)
	Temperature rise (C)	667-21=646
	Vessel Coefficient of Thermal Expansion (m/m/C)	1.5e-05
	Carbon/Graphite Coefficient of Thermal Expansion (m/m/C)	0.3e-05
	Number of Columns along Vessel Diameter	19
	Column Flat-Flat Distance (m)	14.171*2.54e-02=0.360
	Change in Sum of Gap Thicknesses along Vessel Diameter from Cold-to-Hot (m)	0.36*19*646*(1.5-0.3)*e-05= 0.053
	Change in a Single Average Gap (m)	0.053/19=2.8e-03
	Single Average Gap at Hot Condition (m)	(2.8+1.0)*e-03=3.8e-03 (=0.150 inches)
	Sum of Average Gaps at Hot Condition along Vessel Diameter (m)	3.8e-03*19=0.072 (=**2.8 inches**)
As Reported in Fig. 5.12	Sum of Average Gaps at Hot Condition along Vessel Diameter at BOC (m)	2.85*2.54e-02=0.074 (=**2.85 inches**)
	Sum of Average Gaps at Hot Condition along Vessel Diameter at EOC (m)	3.5 *2.54e-02=0.089 (3.5 inches)

[a] General Atomics personal communication, February 2006.

Table 5.5 Lateral Loss Coefficient for Single Inter-Column Gap Between Gap Nodes per Element

Reference	see Figure I.3 and Equation (I.4b)
f , column face width (m)	0.208
g, inter-column gap width (m) (at temp.)	3.80e-03
A_{lat} (m)	3.00e-3
$P_{w\text{-}lat}$ (m)	1.59
$D_{h\text{-}lat}$ (m)	7.60e-3
L_{lat} (m)	0.208*4 = 0.832
C, n	0.184, 0.2
ρ (kg/m^3) @ (485+850)/2 C and 7.0 MPa	3.3
μ (Pa-s) @ (485+850)/2 C and 7.0 MPa	45e-06
$K_{lat,}$ lateral loss coefficient per four inter-column gaps per element per Eq. (I.4b)	3.78e4

Table 5.6 Leakage Loss Coefficient for Laminar Flow between Exterior Edge Coolant Channels and Adjacent Exterior Inter-Column Gaps for Interface between Two Stacked Fuel Elements

Fuel Element	Circumference around Six Faces (m)	0.208*6=1.25
	Number of Coolant Channels Adjacent Six Faces	3*6=18
	Edge Length per Coolant Channel, a (m)	1.25/18=0.069
Single Coolant Channel Adjacent Exterior Face	Reference	Eq. (6)
	Coolant Channel Center to Face Distance, x_c (m)	0.017 [a]
	Coolant Channel Radius, r_c (m)	0.0159
	Gap between Blocks due to Asperities, δ (m)	50.0e-06 [b]
	$\alpha = (x_c^2 - r_c^2)^{1/2}$ (m)	0.0060
	Kinematic Viscosity, υ (m^2/s)	13.6e-06
	Loss Coefficient Per Coolant Channel, $K=\Delta P/w$	8.6e07
Coolant Channels Adjacent Three Exterior Faces	Loss Coefficient per Three Faces, $K=\Delta P/w$ (w=mass flowrate for nine coolant channels adjacent three exterior faces)	8.6e07/9=9.5e06

[a] (14.172-1.282(10))*2.54e-02/2 [b] Kaburaki, [5] p. 60

Table 5.7 Leakage Loss Coefficient for Laminar Flow between Interior Coolant Channels and Adjacent Interior Control Rod Hole for Interface between Two Stacked Control Fuel Elements (see Eq. (28))[a]

Control Fuel Element	Circumference around Control Rod Hole (m)	0.319 [c]
	Number of Coolant Channels Adjacent Hole	6
	Edge Length per Coolant Channel, a (m)	0.319/6=0.0532
Single Coolant Channel Adjacent Interior Control Rod Hole	Coolant Channel Center to Hole Edge Distance, x_c (m)	14.171/2*0.0254= 0.180
	Coolant Channel Radius, r_c (m)	0.0159
	Gap between Blocks due to Asperities, δ (m)	50.0e-06 [b]
	$\alpha = (x_c^2 - r_c^2)^{1/2}$ (m)	0.179
	Kinematic Viscosity, υ (m^2/s)	13.6e-06
	Loss Coefficient Equation	Eq. (6)
	Loss Coefficient Per Coolant Channel, $K=\Delta P/w$	6.51e09
Coolant Channels Adjacent Interior Control Rod Hole	Loss Coefficient per , $K=\Delta P/w$ (w=mass flowrate for six coolant channels adjacent interior control rod hole)	6.51e09/6= 1.09e09

[a] Assume control rod hole is centered in the fuel element. [b] Kaburaki, [5] p. 60
[c] 3.141*4.0*2.54e-2

Table 5.8 Leakage Loss Coefficient for Laminar Flow between Interior Control Rod Hole and Exterior Inter-Column Gap for Interface between Two Stacked Solid Reflector Control Elements (see Eq. (26))[a]

Reflector Control Element	Radius of Element (hex approximated as circle) (m)	14.171/2*0.0254= 0.180
	Radius of Control Rod Hole (m)	0.0508 [c]
Exterior Inter-Column Gap and Interior Control Rod Hole	Gap between Blocks due to Asperities, δ (m)	50.0e-06 [b]
	Kinematic Viscosity, υ (m^2/s)	13.6e-06
	Loss Coefficient Equation	Eq. (4)
	Loss Coefficient, $K=\Delta P/w$	2.63e08

[a] Assume control rod hole is centered in the reflector control element.
[b] Kaburaki, [5.5] p. 60 [c] 4.0/2.0*2.54e-2

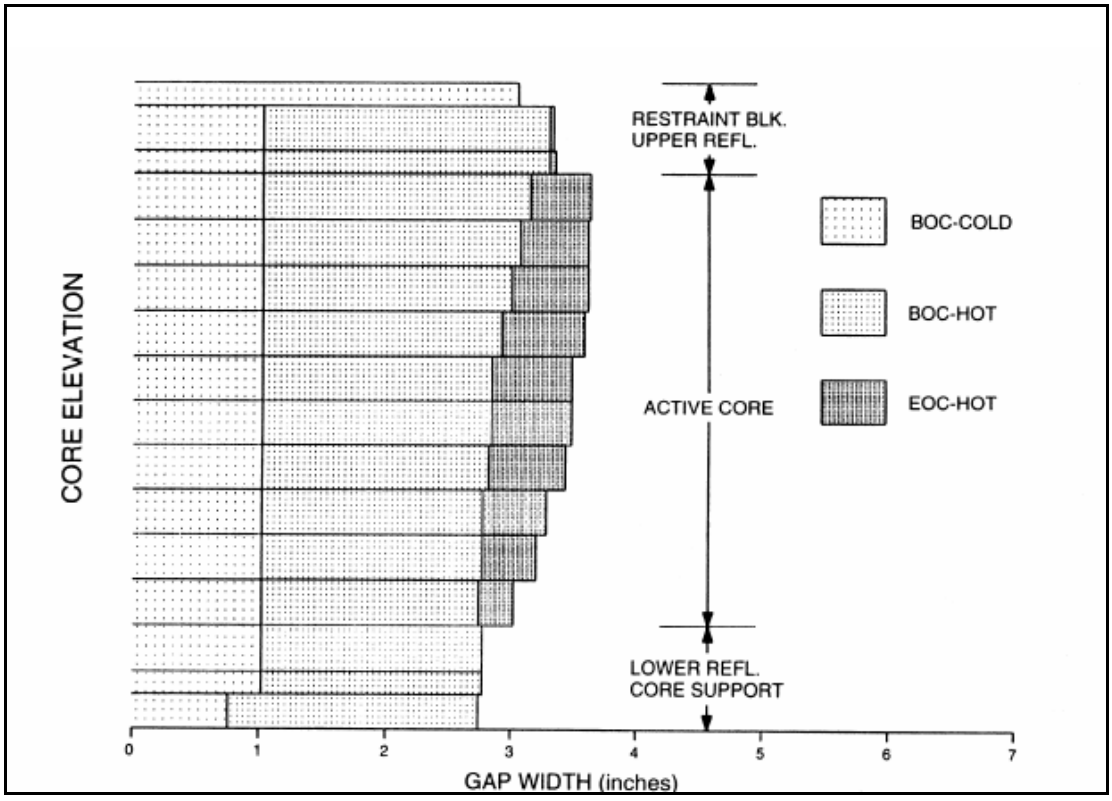

Fig. 5.12 Gap Widths in GT-MHR Prismatic Core

The remaining three loss coefficients are for leakage flowpaths that connect fuel coolant channels with parallel non-fuel coolant channels and thus are important to the fraction of core flow that bypasses the active core region. First, at the interface between two stacked elements, coolant can leak between the coolant channels in the periphery of the element and the inter-column gap that borders the face of the element. Table 5.6 derives the value of the loss coefficient for three faces of an element from Eq. (I.18). Figure I.6 defines the geometry assumed in this expression. These three faces are oriented inward in the case of the *leak-in* loss term in the momentum balance of Eq. (I.5) and

outward in the case of the *leak-out* term in Eq.(I.6). Note that in the GT-MHR design, nine three coolant channels border each element face. Second, at the interface between two fuel control stacked elements, coolant can leak between the control rod hole and the interior coolant channels that border this hole. The value of the loss coefficient is given in Table 5.7 and appears in the momentum balance of Eq. (I.9). Again, Eq. (I.18) and Fig. I.6 apply. Note in the GT-MHR design, six coolant channels border the control hole. Third, at the interface between two stacked control reflectors, coolant can leak between the control rod hole and the outer face edges of the elements. The loss coefficient is given in Table 5.8 and appears in the momentum balance of Eq. (I.9). The value is based on Eq. (I.6) and the geometry shown in Fig. I.5. Note for accurate assignment of core flow distribution, a key requirement is that the cross-sectional area of these three flowpaths be known with good precision. For all three loss coefficients, the value for the gap between the elements due to asperities is 50×10^{-6} m. as shown in Tables 5.6, 5.7, and 5.8 and as given in [5.11] for the Fort St. Vrain Reactor.

While the GT-MHR core dimensions given above imply a coolant distribution for an imposed overall core pressure drop between inlet and outlet, we chose to allocate total core coolant at beginning of life as follows: fuel coolant channels, 90%; inter-column gaps, 8.5%; and control rod holes, 1.5%. This represents the midpoint between the GT-MHR conditions in [5.13] and the HTTR conditions in [5.2]. The exact values are unimportant since it is the sensitivities of these values to geometry changes that are of interest.

These fractional flow splits were obtained by applying a single pressure boundary condition across all channels at the core inlet and applying individual flow boundary conditions at the outlet of each of the core channels. The flow boundary conditions applied appear in Fig. 5.13 at the core outlet. The actual flow split among the three channel types is shown in Fig. 5.14. In practice the core coolant distribution follows from a pressure drop that is maintained between inlet and outlet plenum. In a second run of the code, the loss coefficients at the bottom row of elements (row ten) shown in Fig. 5.13 were adjusted to bring all channels into an overall pressure drop of 50 KPa, the same value as in the GT-MHR.

All perturbed cases assumed as a starting point the Base Case with this 50 KPa inlet to outlet pressure drop as the imposed boundary condition. In each of the perturbed cases, the effect of a change in a dimension in a leakage path was simulated by changing the corresponding loss coefficient by an amount that would be induced by such a change.

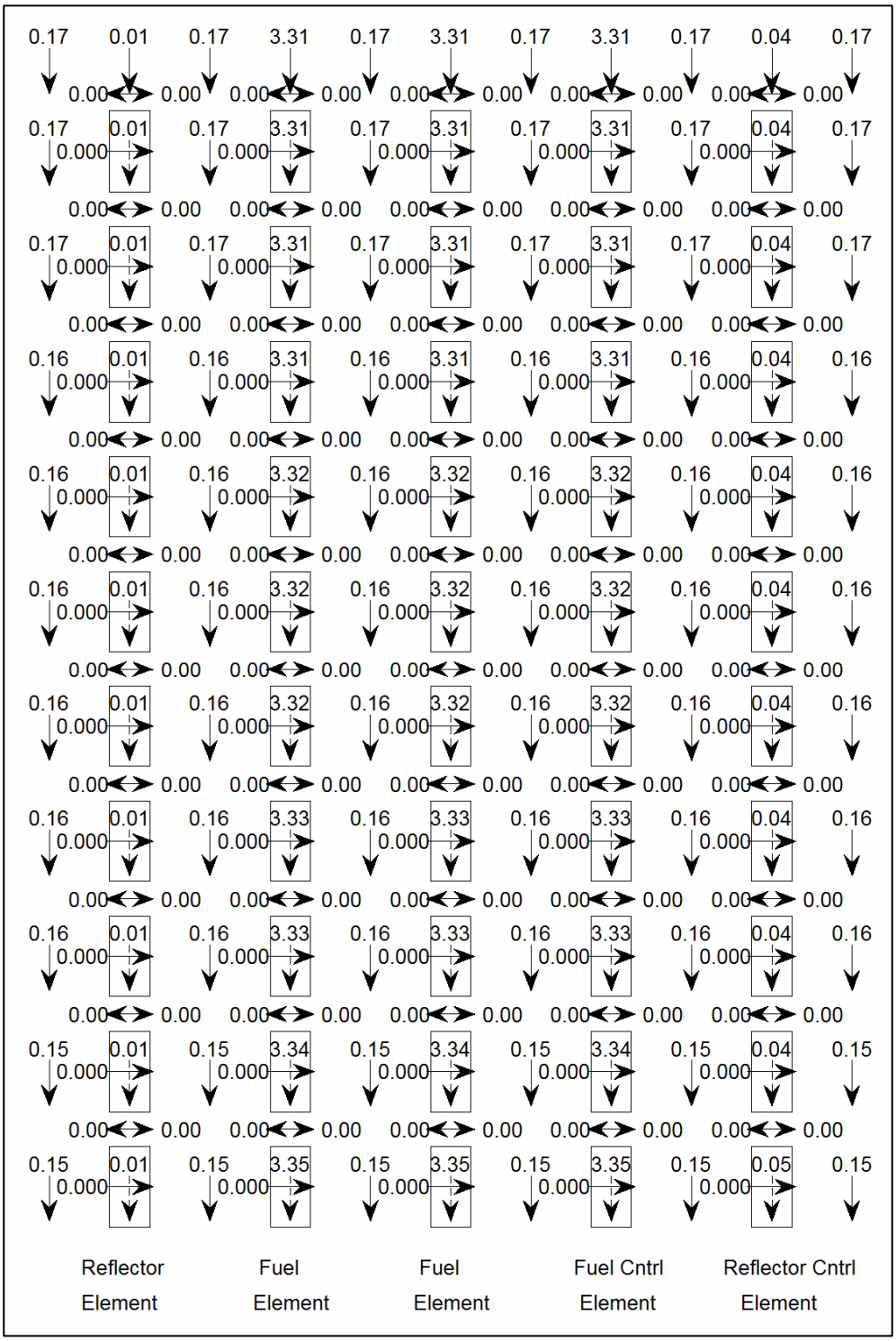

Fig. 5.13 Axial and Lateral Coolant Flowrates (kg/s) for Base Case. Pressure boundary condition at core inlet; flow boundary condition at outlet of each channel. Loss coefficients defined between channel outlets and outlet plenum provide for 50 KPa overall pressure drop. Columns are ten elements high. Dashed arrow is flow internal to element. Not shown: control rod hole flow in fuel control and reflector control elements.

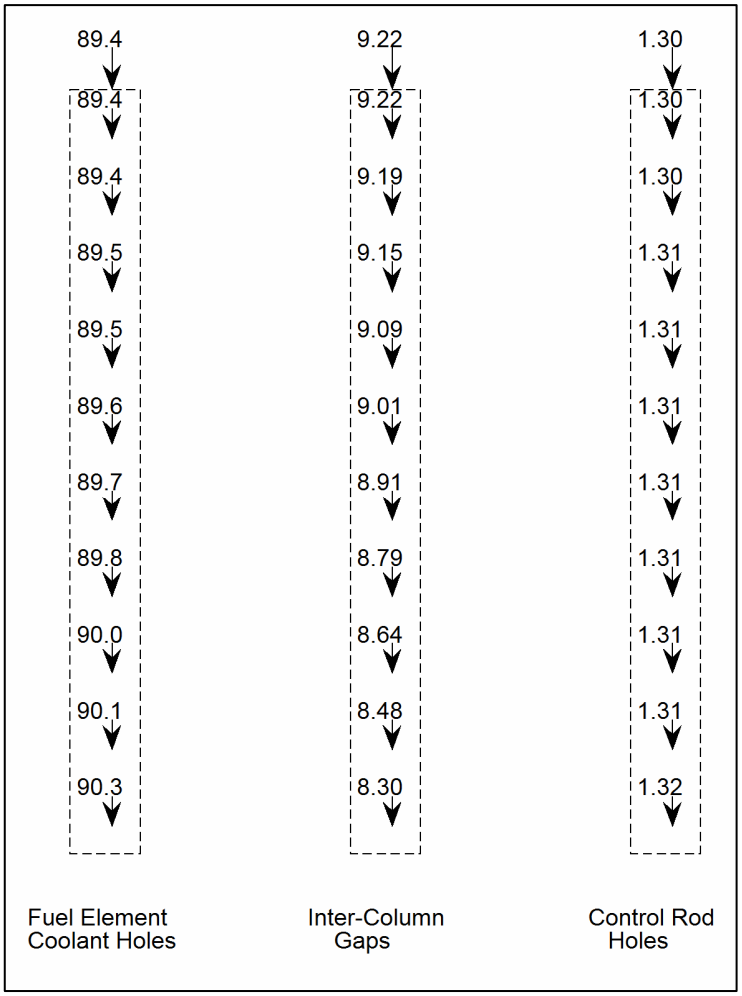

Fig. 5.14 Axial Coolant Flow Distribution for Base Case

5.1.6 Perturbed Cases

The base case establishes a core flow distribution at nominal conditions and serves as a reference against which the results of perturbing a parameter in a leakage path can be compared. The consequence of the perturbation is measured in terms of the change induced in the axial temperature profile of the coolant in a fuel element.

In practice, the effect of a perturbation in core hydraulics involves establishing a new equilibrium for flow around the entire primary system. The new equilibrium will be a function of the head to flow curve for the primary system that takes in the characteristics of the turbomachines. Since the calculation of flow distribution in this section of the report is limited to a pressure boundary condition imposed between the inlet and outlet plenum, care must be exercised in interpreting these results and drawing conclusions about what they might imply for the behavior of the core in the context of the integrated plant. The approach taken is in each perturbed case to adjust the individual flows by that factor such that the sum of these adjusted individual flows sums to the total core flow in the Base Case. Now since each of the perturbed cases corresponds to a net

decrease in core hydraulic resistance compared to the base case, the total primary flow will increase. By not taking credit for this increase, the axial temperature profile in a fuel element coolant channel for the integrated plant will lie below what we calculate. So the sensitivities presented below could be considered an upper bound on what would occur in the integrated plant.

The fuel coolant axial temperature in the Base Case as a function of axial length l from top to bottom of core is from an energy balance

$$T_{BC-i}(l) = T_{BC}(0) + \int_o^l \frac{K_i \; q'(l)}{w_{BC-i}(l)} dl \tag{1}$$

where

$q'(l)$ = axial linear power profile in the core, and

$w_{BC-i}(l)$ = fuel element coolant flowrate in Base Case in fuel column i

where K_i is a constant such that the outlet temperature in column i satisfies

$$T_{BC-i}(L) = 490 + (850 - 490) \frac{w_{BC-tot}}{\sum_i w_{BC-i}(L)} . \tag{2}$$

That is, the fuel coolant exit temperatures from fueled columns in the Base Case are equal and are elevated above the core average temperature by an amount that takes into account the flow that bypasses the fuel columns. The numerator and denominator in the above expression are related to one another through

$$w_{BC-tot} = \sum_i w_{BC-i}(L) + \sum_{other} w_{BC-other}(L) \tag{3}$$

where i represents fuel coolant and *other* represents all axial coolant other than fuel coolant i.e. inter-column gaps and control rod holes.

The fuel coolant outlet temperature from column i for perturbed Case k subject to the total core flow rate equaling that in the Base Case is then

$$T_{Case\,k-i}(l) = T_{BC}(0) + \int_o^l \frac{K_i \; q'(l)}{w_{BC-tot} \cdot \dfrac{w_{Case\,k-i}(l)}{w_{Case\,k-tot}}} dl \tag{4}$$

where

$$w_{Case\,k-tot} = \sum_i w_{Case\,k-i}(L) + \sum_{other} w_{Case\,k-other}(L) . \tag{5}$$

The axial linear power profile adopted for the prismatic core analysis is the ten block case shown in Fig. 5.15 which is Fig. 56 of [5.15] edited to show tabular values. The fuel coolant temperatures as a function of axial position for the Base Case calculated from Eq. (4) are shown in Figure 5.16. With power-profile management, the temperature profiles for the three columns (channels) fall on top of each other. Table 5.9 summarizes the sensitivity results for the fuel coolant channel outlet temperatures for all the cases.

Table 5.9 Sensitivities of Fuel Coolant Channel Outlet Temperature

	Column 2: Fuel Element	Column 3: Fuel Element	Column 4: Fuel Control Element
Base Case	889	889	889
Case 1: Leakage Past Control Rod	891	891	891
Case 2: Leakage Past Gap Seal at Core Support	909	909	909
Case 3: Wedge-Shaped Opening in Elements at Core Periphery	900	900	897
Case 4: Opening of Inter-Column Gap Width	890	890	890

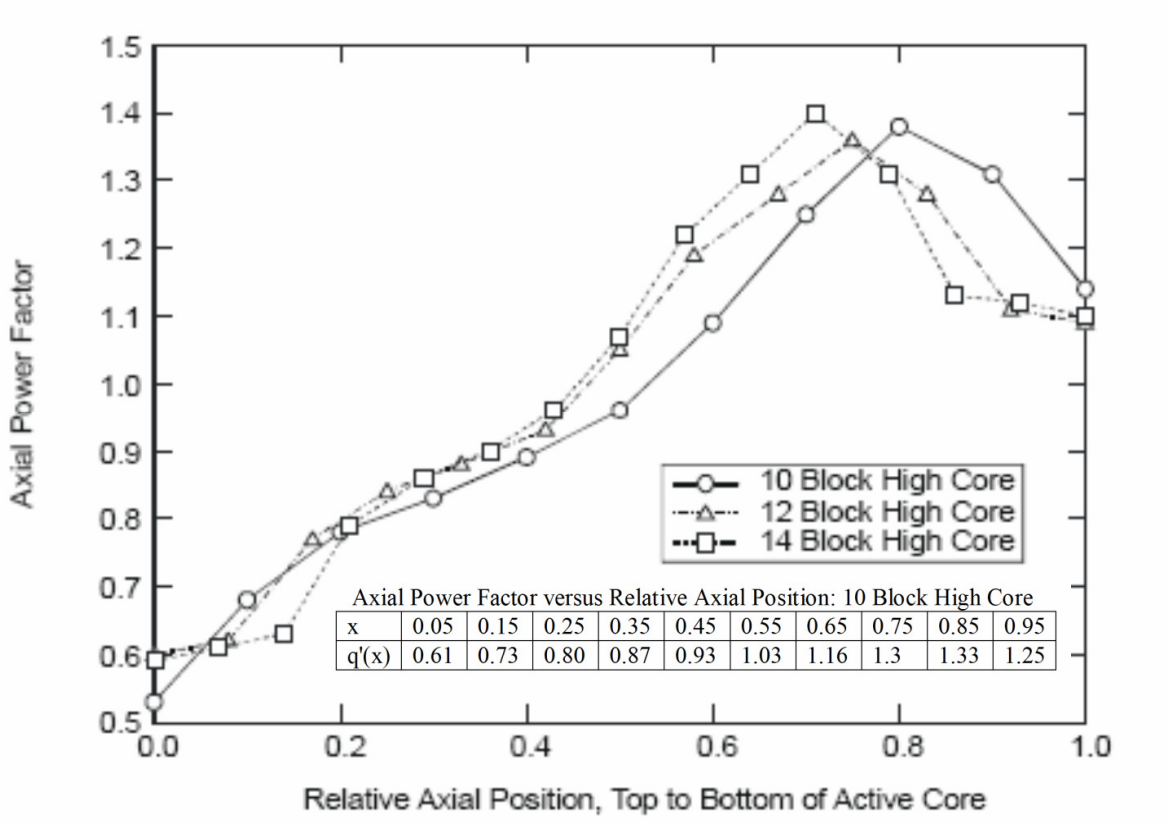

Fig. 5.15 Axial Power Profile Adopted as Representative for Prismatic Core

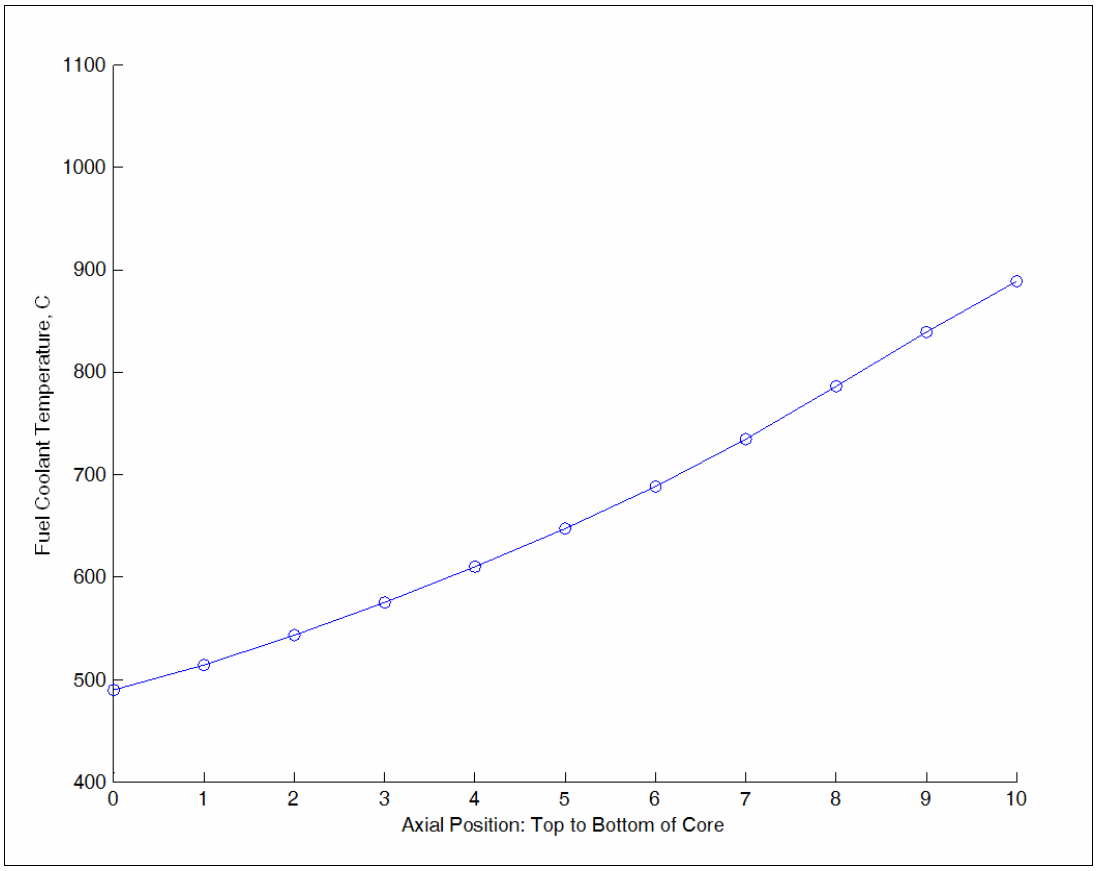

Fig. 5.16 Fuel Coolant Temperatures as a Function of Axial Position: Base Case. Columns 2 through 4 shown. Radial power profile selected via constant K_i to give same temperature at outlet of the three columns.

Case 1: Geometry Resistance to Control Rod Hole Flow

In the Base Case, a small fraction of the reactor coolant passes through the control hole in each of columns 4 and 5 as seen in Fig. 5.14. The friction pressure drop is several orders of magnitude smaller than the overall core pressure drop. The residual pressure was distributed so that one half occurred over the length of the hole in the top element and the other half over the length of the hole in the bottom element. The former represents the blocking of the control hole by the control rod and the latter the effect of the seals at the bottom of the control rod hole. This is achieved through the appropriate choice of values for loss coefficients in the control hole channel.

To simulate the case of the control rod not present in the control rod hole or, equivalently, posing no flow resistance, the upper loss coefficient was set to zero in columns 4 and 5. There was essentially no change in lateral flowrates compared to the Base Case shown in Fig. 5.13. The axial flowrates expressed as a percentage of reactor flowrate are shown in Fig. 5.17. Again, this figure indicates no significant change in lateral leakage from the Base Case. The seal at the bottom of the control hole essentially limits any large change in the flowrate in the control hole. The new axial temperatures in

the fuel coolant channels are shown in Fig. 5.18. The results (squares) fall on top of the base case (circles).

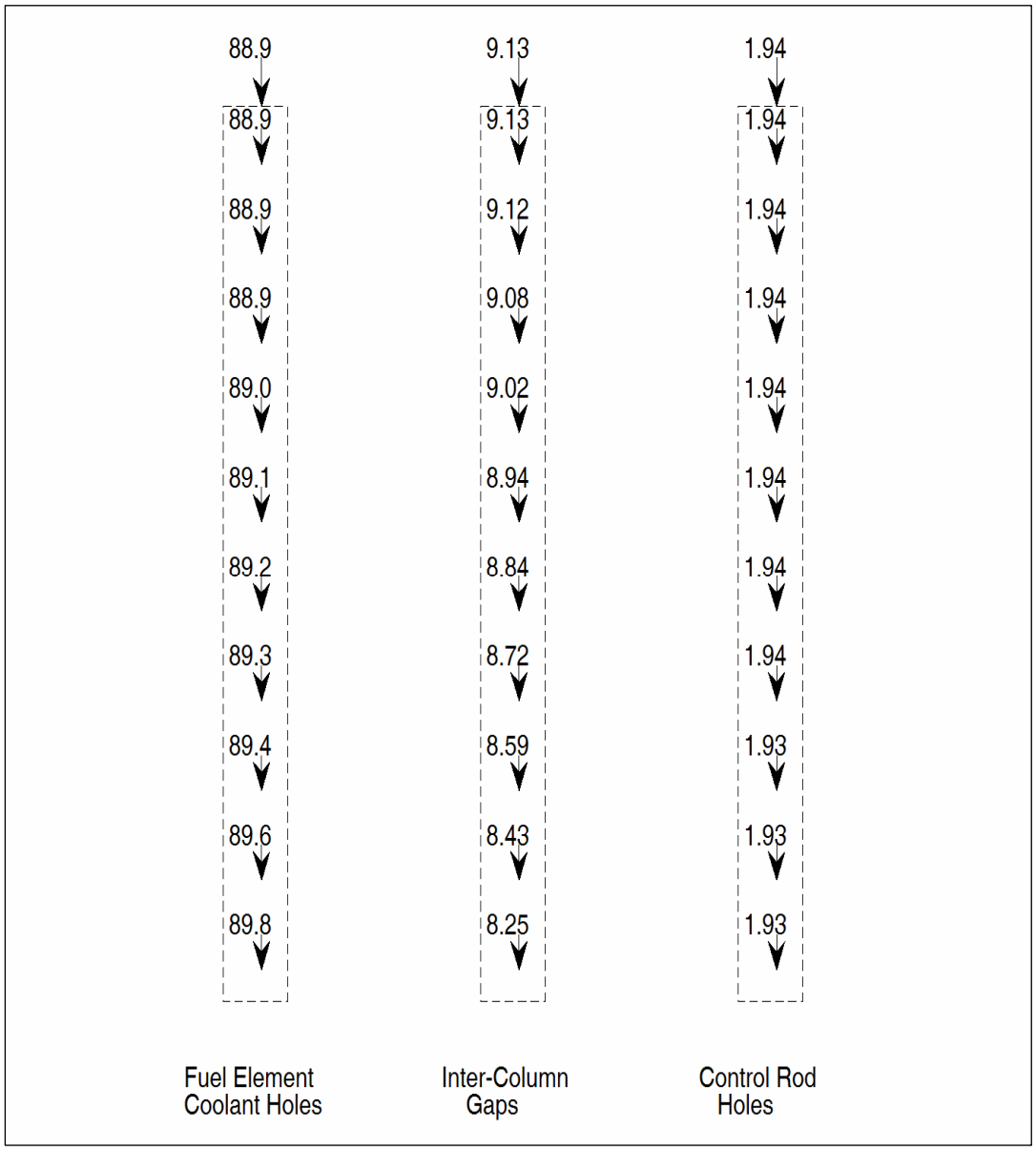

Fig. 5.17 Axial Coolant Flow Distribution: Case 1 - Leakage Past Control Rod

Case 2: Design Seal Behavior in Inter-Column Gap at Core Support

In the Base Case, the coolant at the base of an inter-column gap is assumed restricted by a seal for flow through the core support blocks to the outlet plenum. The hydraulic behavior of the seal is represented by a loss coefficient in the gap at the bottom level of the core. This loss coefficient raises the total pressure loss for the gap flow up to

the overall core pressure drop. The axial pressure drop through the seal is about 66% of the overall core pressure drop.

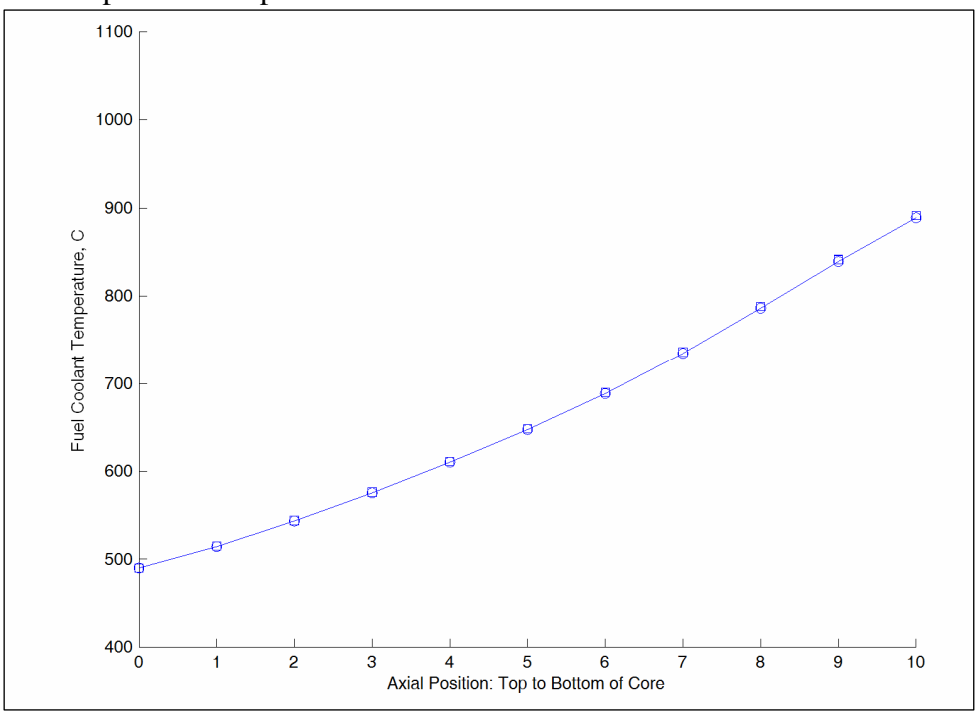

Fig. 5.18 Fuel Coolant Temperatures as a Function of Axial Position: Case 1 - Leakage Past Control Rod. Columns 2 through 4 shown.

The failure of this seal was simulated by setting the loss coefficient to a value equal to the friction loss coefficient in the gap over the length of one element. This change was limited to the gaps associated with columns 4 and 5 to simulate geometry distortion at the core periphery. The impact of this change on core flow distribution is seen in Fig. 5.19. Compared to the Base Case there is an increase in coolant flow through the seal. Some of this flow comes from neighboring column gaps as indicated by the general trend of lateral gap flow towards columns 4 and 5. Overall there is an increase in flow into the inter-column gaps at the top of the core as the path resistance has been reduced. Figure 5.20 shows that the increased gap flow occurs at the expense of fuel coolant flow. The new axial temperatures in the fuel coolant channels are shown in Fig. 5.21. A noticeable difference can be seen between the base case and Case 2. There is no variation between the three columns for each case.

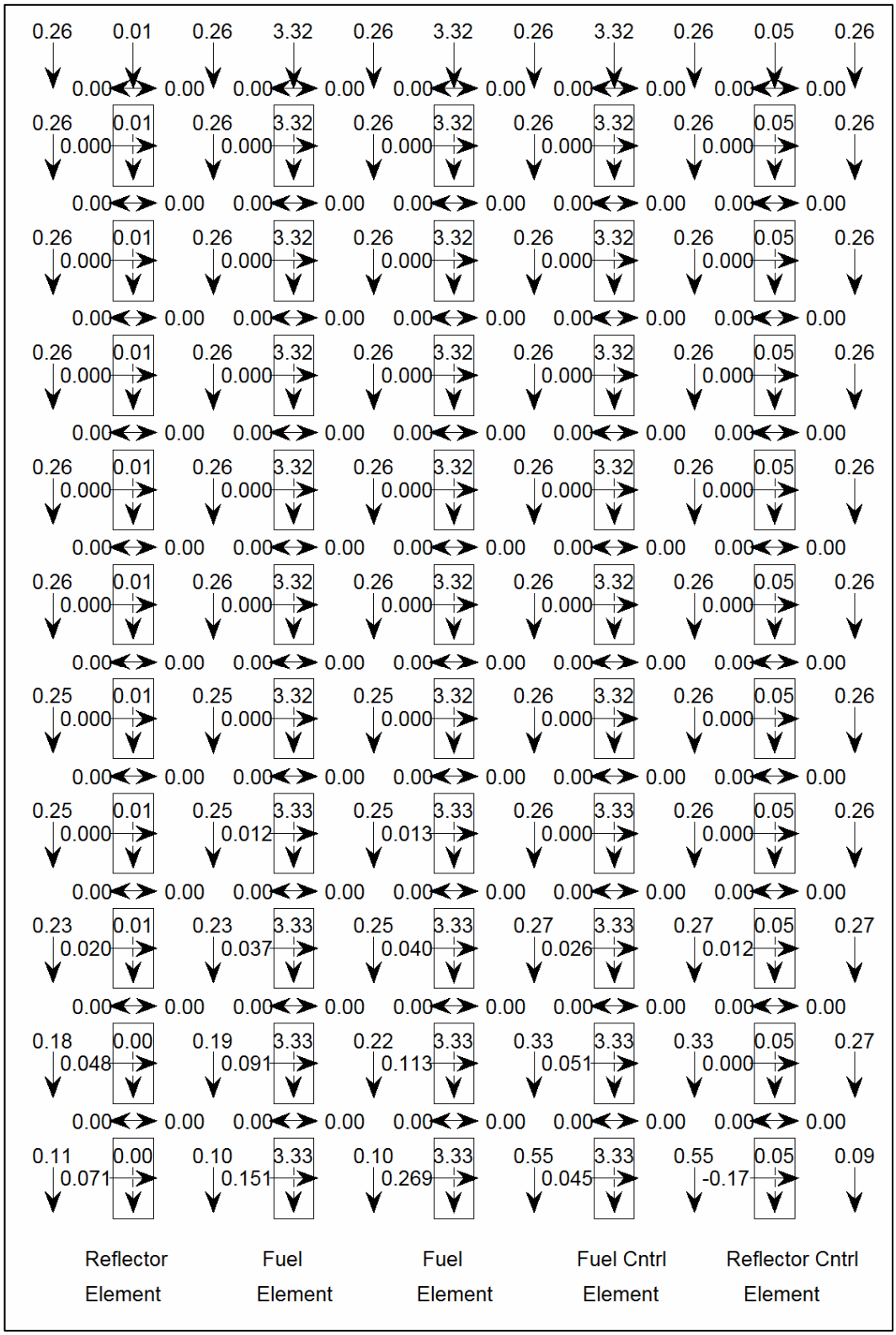

Fig. 5.19 Axial and Lateral Coolant Flowrates (kg/s): Case 2 - Leakage from Inter-Column Gap Past Seals at Core Support

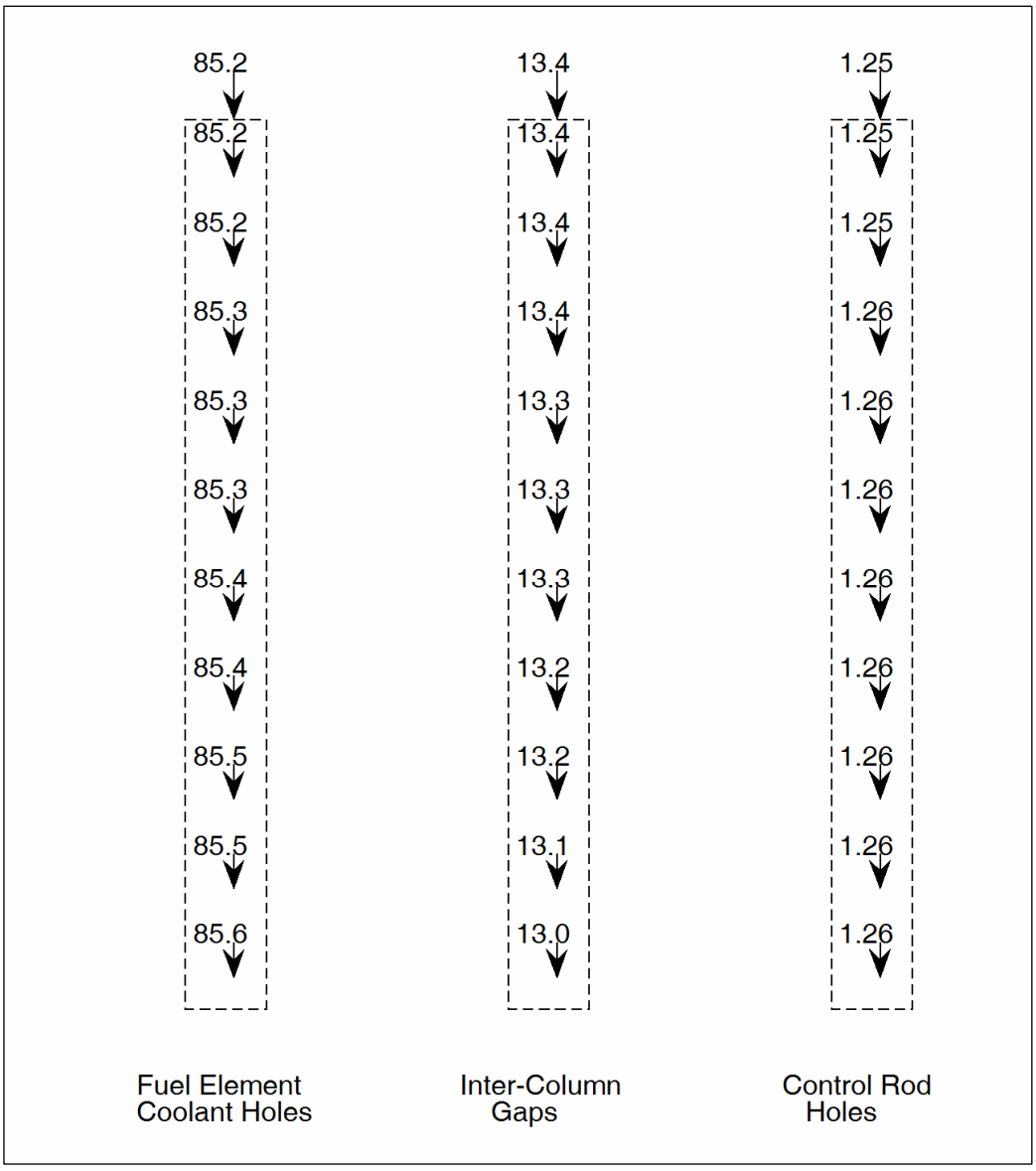

Fig. 5.20 Axial Coolant Flow Distribution: Case 2 - Leakage from Inter-Column Gap Past Seals at Core Support

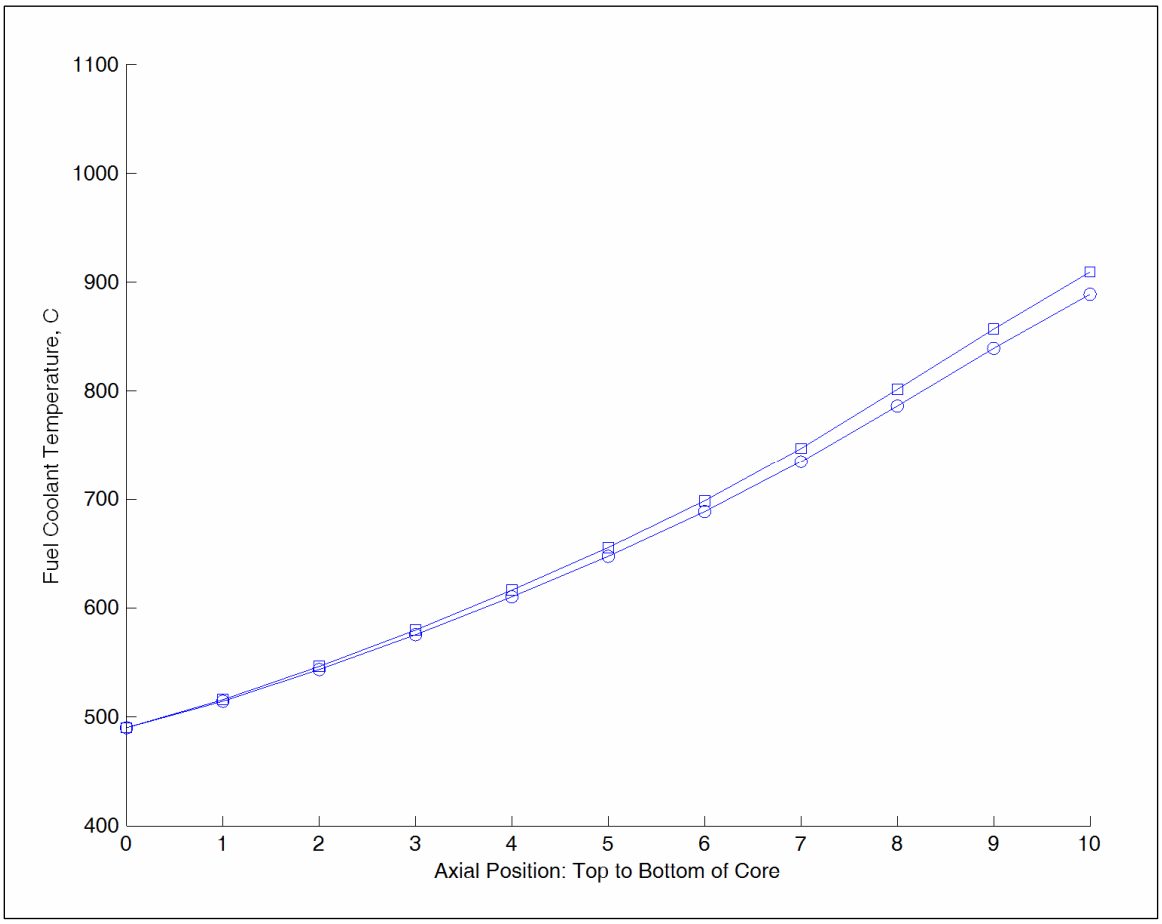

Fig. 5.21 Fuel Coolant Temperatures as a Function of Axial Position: Case 2 - Leakage from Inter-Column Gap Past Seals at Core Support. Base Case Shown as Circles, Case 2 as squares.

Case 3: Block-to-Block Stacking Surface Fit

In the Base Case, the friction pressure drop in the fuel coolant channels is equal to the overall core pressure drop, while the friction pressure drop in the gap coolant channels is about 33% of the overall core pressure drop. Both these channel types are open at the top of the core. There is no significant lateral leakage flow from between stacked elements into or from inter-column gaps as Fig. 5.13 for the Base Case shows.

The effect of a wedge-shaped opening of the interface between stacked elements at the periphery of the core due to graphite distortion was examined. The outboard leakage coefficients in columns 4 and 5 for both fuel coolant and control hole coolant were decreased by a factor of 100 over the entire axial length of these columns. This corresponds to an increase in interface gap size of 4.6. Because of the large pressure drop through the seals at the base of the inter-column gap in the Base Case, there is a pressure differential between fuel coolant channel and gap channel that increases with decreasing axial elevation. This differential drives coolant from the gaps into the fuel coolant

channels. Opening the inter-element gap reduces the resistance. As a consequence at the bottom of the core there is increased flow from gaps into the fuel coolant channels. One sees in Fig. 5.22 the increased fuel coolant axial flow in column 4 and the decreasing gap axial flow in neighboring column gaps as the core outlet is approached. Significant gap lateral flow in the direction of column 4 is generated across the core as the gap flow sees the reduced path of resistance thorough the fuel coolant channels to the core exit. Figure 5.23 shows the axial behavior after combining flows for fuel channels and for gap channels. One also sees that the control holes at the core midplane serve as an alternate route for former gap coolant to make its way to the core outlet via the fuel coolant channels at the bottom of the core. The new axial temperatures in the fuel coolant channels are shown in Fig. 5.24. There is some variation between the results for the three fuel columns (squares) and the base case (circles).

Case 4: Inter-Column Gap History at Core Periphery

An opening of the inter-column gap along the entire axial length of the core creates a reduced resistance path for core coolant causing an increase in the fraction of flow that bypasses fuel coolant channels. Figure 5.12 shows roughly a ten percent increase in inter-column gap size in going from beginning of life to end of life. This corresponds to a 21 percent decrease in the axial friction loss coefficient in the gap based on Eq. (I.13).

To simulate the effect of a ten percent increase in the gap size throughout the core over life, the gap axial pressure loss coefficient was reduced by 21 percent compared to the base case for columns 1 through 5. The consequence for fuel coolant flow versus gap flow appears in Fig. 5.25. Essentially the large pressure drop through the seals at the base of the gaps dominates the change in gap axial flow resistance. There is a reduction in fuel coolant flowrate, but it is relatively small. As a result, the new axial temperatures in the fuel coolant channels essentially overlay the Base Case when plotted against the data in Fig. 5.16.

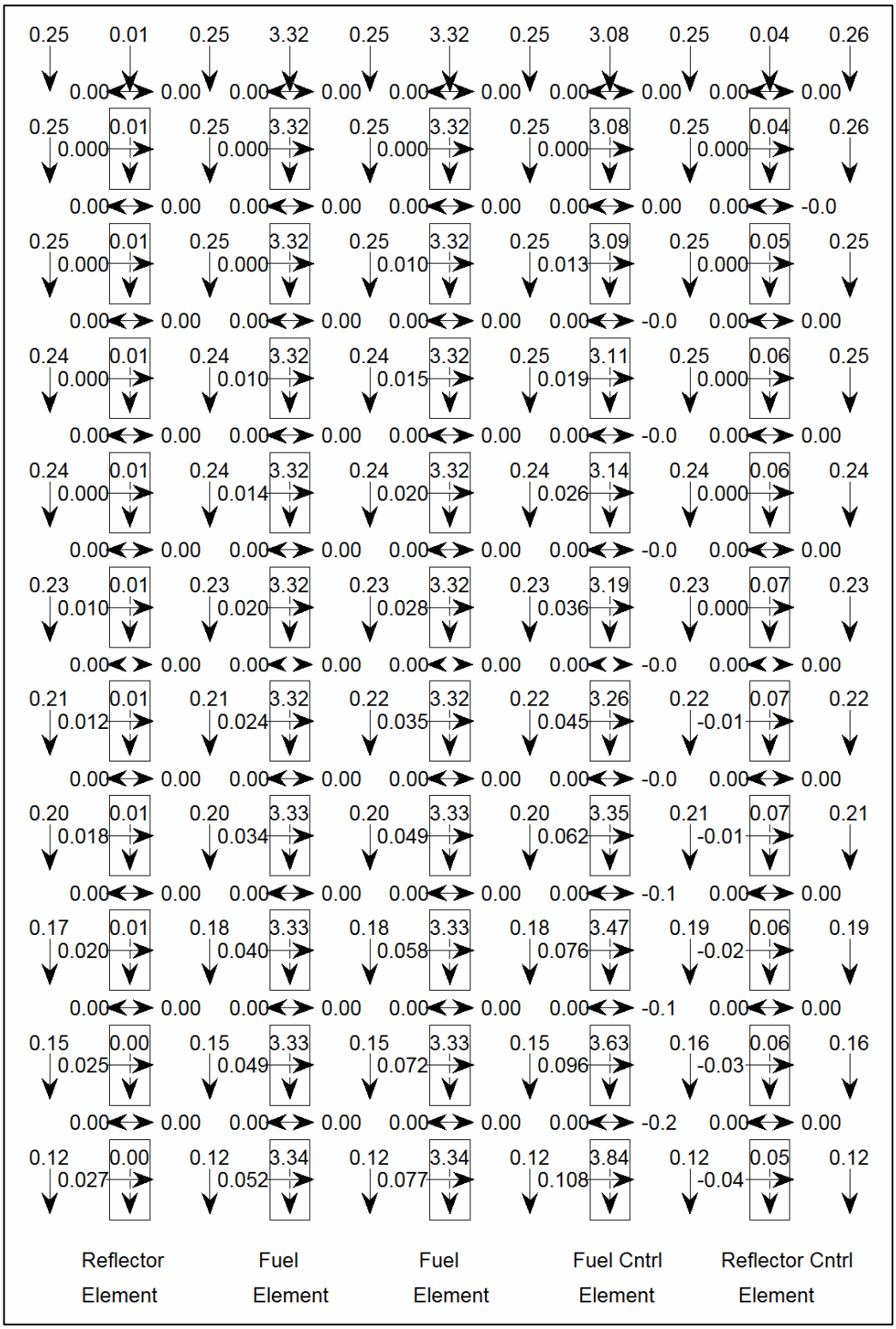

Fig. 5.22 Axial and Lateral Coolant Flowrates (kg/s): Case 3 – Wedge-Shaped Opening in Stacked Element at Core Periphery

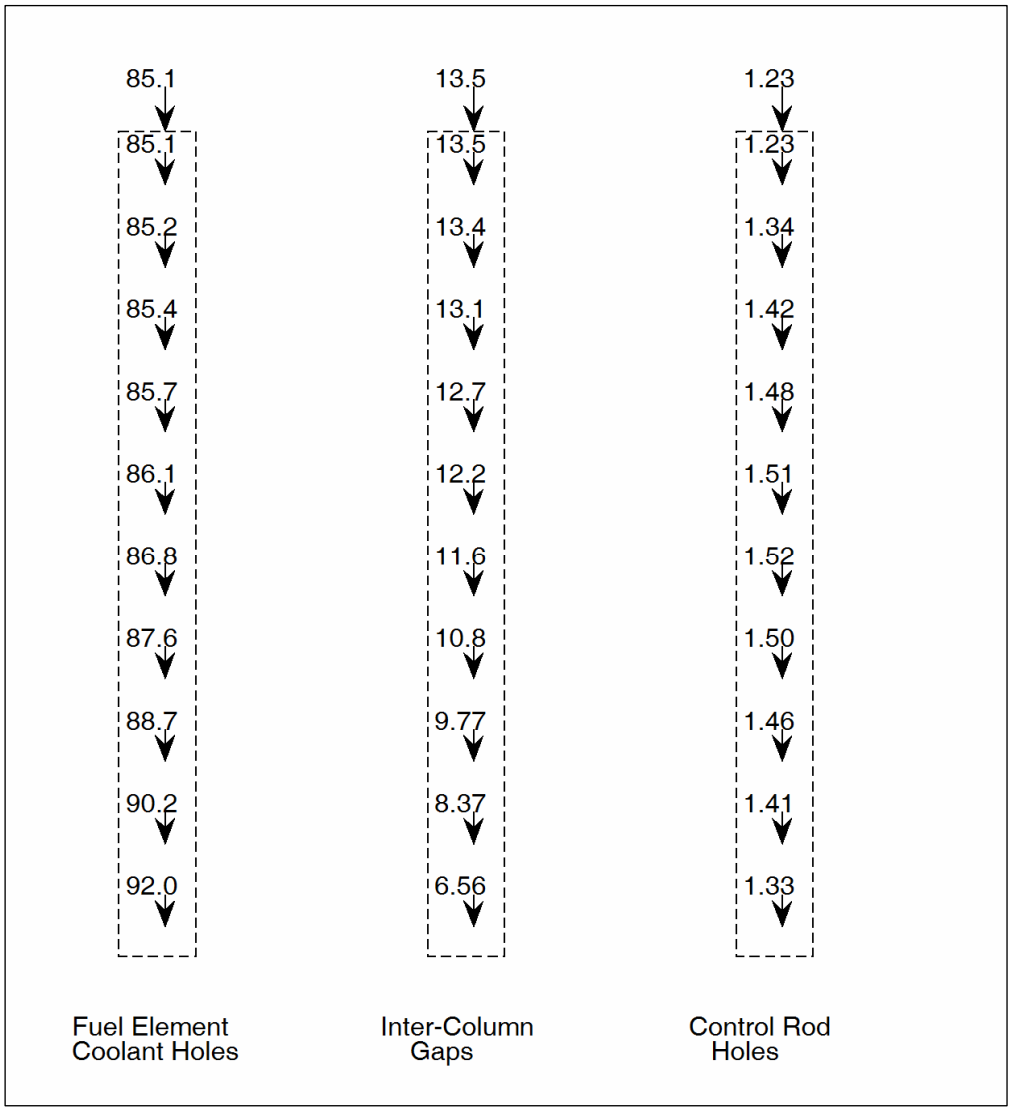

Fig. 5.23 Axial Coolant Flow Distribution: Case 3 - Wedge-Shaped Opening in Stacked Element at Core Periphery

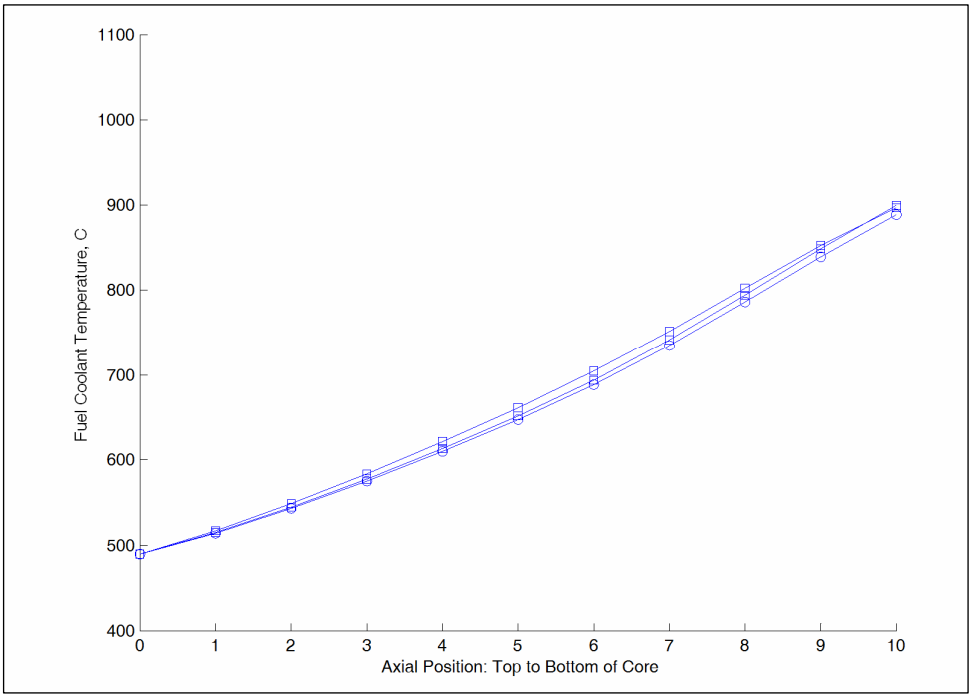

Fig. 5.24 Fuel Coolant Temperatures as a Function of Axial Position: Case 3 - Wedge-Shaped Opening in Stacked Element at Core Periphery, Base Case Shown as Circles, Case 3 as Squares.

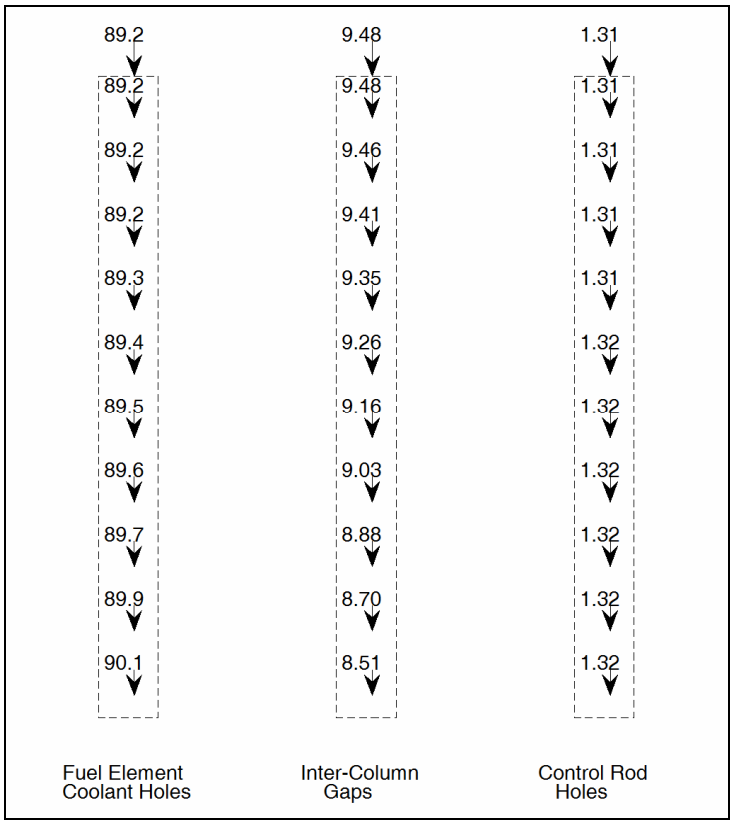

Fig. 5.25 Axial Coolant Flow Distribution: Case 4 - Opening of Inter-Column Gap Width at Core Periphery

5.2 PBR Core Flow Distribution Study

During the development of the PIRTs for pebble bed reactor cores, questions were consistently raised about the difficulty in assessing peak fuel temperatures in pebble bed systems as a consequence of the uncertainty associated with the core configuration and the distribution of coolant flow within the bed. The assessment of the peak temperature in the pebble bed core relies on three individual predicted quantities: the volumetric rate of power generation in the hottest pebble in the bed, the rate of flow of coolant over the surface of that pebble and the heat transfer coefficient associated with that rate of flow and the pebble bed configuration. The current assessment is focused only on the identification of thermal hydraulic modeling capability and needs, so it is assumed that suitable core neutronics analyses can be completed to provide a prediction of the peak rate of power generation with acceptable accuracy. The work summarized herein provides an initial assessment of the sensitivity of predictions of the core thermal hydraulic characteristics to the uncertainty in the pebble size and pebble coolant void distribution for assessment of steady state reactor performance. Experimentally derived correlations, taken from the open literature, for the pressure loss coefficient and the heat transfer coefficient provide a basis for this assessment. Future assessments will consider the additional parameter space needed for transient assessments, including radiation, conduction and natural convection heat transfer within the bed and the solid graphite moderator.

5.2.1 Assumed Pebble Bed Characteristics and Dimensions

As stated in the introduction, a candidate design for a potential pebble bed reactor concept has not yet been identified. However, in the assessment of the impacts of uncertainty in design parameters, it is often necessary to identify a design baseline in order to assess deviations from baseline system performance as a consequence of specific uncertainties. For the purpose of these analyses, a 600 MW_{th} reactor with a core outlet coolant temperature of 900 ºC and a core temperature rise of 400 ºC is assumed. The reactor core is assumed to have an annular design with a solid graphite outer moderator surrounding the core and a cylindrical solid graphite moderator at the center of the core. The outer diameter of the fueled region is assumed to be 3.5 m, and the inner diameter of the fueled region is assumed to be 1.75 m. The active core region is assumed to have a height of 8.5 m [5.16]. The fueled region is assumed to contain a fixed bed of fuel pebbles with an outer diameter of 6.0 cm. Assumed geometric quantities are summarized in Table 5.10.

For the purpose of these studies, the bypass flow through the gaps in the moderator blocks is neglected, and it is assumed that the assessments completed for the Prismatic Cores in the previous section is directly applicable in those regions. It is expected that the uncertainty related to the distribution of pebbles within the bed is more significant than the bypass flow, and geometric assumptions have been made to allow a preliminary study to be completed without detailed design information. A more rigorous assessment of the impact of bypass flow through the moderator assemblies versus the impact of the uncertainties in the pebble bed itself requires a more detailed baseline

design to be defined and can easily be completed using the procedures outlined in this report when such design data is available.

Table 5.10 Assumed Pebble Reactor Core Parameters

Quantity	Notation	Units	Value
Reactor Thermal Power	P_{tot}	MW	600
Pebble Diameter	d_p	cm	6.0
Core Outer Diameter	$d_{o,c}$	m	3.5
Core Inner Diameter	$d_{i,c}$	m	1.75
Core Height	H	m	8.5
Core Outlet Temperature	$T_{o,c}$	ºC	900
Core Inlet Temperature	$T_{i,c}$	ºC	500

In addition to the geometric description of the reactor core, thermophysical data is needed in order to calculate key non-dimensional quantities, such as the Reynolds number, needed to evaluate the applicability of experimentally derived correlations as well as the sensitivity of those correlations' predictions to uncertainties in the core geometric data. The primary system coolant is assumed to be helium at a pressure of 7 MPa. The thermophysical properties in Table 5.11 [5.17] calculated at this pressure and at a core midpoint temperature of 700 ºC are used in all analyses presented herein.

Table 5.11. Assumed Helium Thermophysical Properties.

Quantity	Notation	Units	Value
Density	P	kg/m^3	3.435
Specific Heat	c_p	kJ/kg-ºC	5.190
Dynamic Viscosity	M	Pa-s	4.534×10^{-5}
Conductivity	K	W/m-ºC	0.357
Mean Coolant Temperature	$\overline{T}$	ºC	700

Using these parameters, an open bed Reynolds number can be calculated. Since the local mass flow rate within the bed is expected to be a strong function of the pebble packing density, correlations for related parameters are typically presented as functions of the open bed Reynolds number, Re, which is a function of the velocity of coolant through the bed with all pebbles removed. The pebble Reynolds number, Re_p, remains a more useful measure of turbulence and heat transfer characteristics of a single pebble, the calculation of the pebble Reynolds number requires not only knowledge of the pebble diameter but also the local coolant velocity within the pebble bed. Since these parameters are not normally known for a pebble bed system, the open bed Reynolds number provides a more useful engineering quantity. For the assumed baseline pebble

bed, the open bed Reynolds number is approximately 1.5 million. Additional calculated parameters for the baseline pebble bed reactor considered are shown in Table 5.12.

5.2.2 Prediction of Pebble Bed Mass Flows and Local Velocities

The accurate prediction of the local flow velocities or mass flow rates within the pebble bed is tied to the accurate prediction of the bed pressure loss coefficient. For conventional pressure loss coefficient correlations to be applicable, the diameter of the pebbles must generally be significantly smaller than the effective diameter of the reactor core, which is consistent with the nominal pebble bed concept. Furthermore, the pebbles must be of uniform size and uniformly distributed within the core for the simplest correlations to be applied. While the diameter and distribution of the pebbles are likely to be subject to significant uncertainty in a real system and these correlations should not be expected to provide an accurate prediction of the local thermal hydraulic characteristics within the three-dimensional core, the application of correlations based upon these assumptions does provide a means of bounding the expected values for the core pressure drop or mass flow as well as the impact of local uncertainties in geometric configuration.

Table 5.12 Calculated Pebble Bed Thermal Hydraulic Quantities

Quantity	Notation	Formula	Units	Value
Core Temperature Rise	ΔT_c	T_{out} - T_{in}	ºC	400
Core Cross Sectional Area	$A_{xs,c}$	$\frac{\pi}{4}\left(d_{o,c}^2 - d_{i,c}^2\right)$	m^2	7.216
Core Wetted Perimeter	$P_{w,c}$	$\pi\left(d_{o,c} + d_{i,c}\right)$	m	16.49
Core Hydraulic Diameter	$d_{h,c}$	$4A_{xs,c} / P_{w,c}$	m	1.75
Core Mass Flow	m_c	$P_{tot} / c_p \Delta T_c$	kg/s	289
Open Bed Velocity	u_c	$m/ \rho A_{xs,c}$	m/s	11.65
Open Bed Reynolds Number	Re_c	$\rho u_c d_{h,c} / \mu$		1.5×10^6
Helium Prandtl Number	Pr	$c_p \mu / k$		0.659

5.2.2.1 Standard Correlations for Pressure Drop

With the assumptions and constraints described, the pressure drop associated with a porous bed can be calculated as a function of the pebble diameter, D_P, and packing fraction, ε, using the well-known equation of Ergun [5.18]

$$\Delta p = \tfrac{1}{2}\rho u_c^2 \frac{H}{d_{h,c}} \lambda_E , \qquad (6)$$

where the loss coefficient, λ_E, is given by

$$\lambda_E = \frac{1-\varepsilon}{\varepsilon}\left(\frac{300}{\mathrm{Re}_p/(1-\varepsilon)} + 3.5\right), \qquad (7)$$

and the Reynolds number, Re_p, is calculated as

$$\mathrm{Re}_p = \frac{\rho u_c d_p}{\mu}. \tag{8}$$

The quantity $Re_p/(1-\varepsilon)$ is shown as a function of the packing fraction, ε, in Fig. 5.26. The quantity $Re_c/(1-\varepsilon)$ is also shown for comparison. In the development of the Ergun equation, it is assumed that its applicability is limited to the range of $0 \le Re_p \le 2500$. However, studies at higher Reynolds number, notably the work of Achenbach [5.19], have shown that the dimensionless pressure loss coefficient approaches a constant value for $Re_c/(1-\varepsilon) \ge 5x10^5$. For this reason, the Ergun formulation is often applied at higher Reynolds numbers as a baseline prediction. The Ergun equation was also developed for $0.4 \le \varepsilon \le 0.6$, but is often applied beyond those bounds as a baseline for comparison. [5.19] The Ergun pressure loss coefficient and the resulting pressure drop through the baseline pebble bed core are shown in Fig. 5.27, which clearly illustrates that the pressure drop and the pressure loss coefficient are related by a simple multiplicative constant. As a consequence, consideration of only the pressure loss coefficient is sufficient to assess the impact of geometric and bypass flow uncertainties on the predictions of mass transport related quantities.

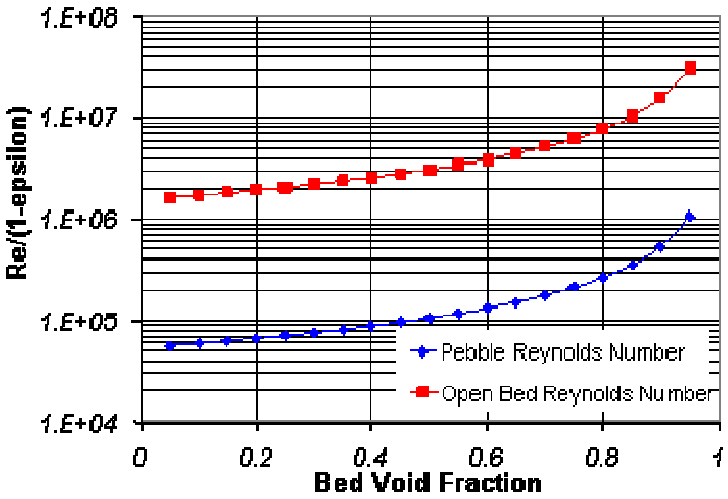

Fig 5.26. Comparison of Open Bed and Pebble Reynolds Numbers Divided by the Quantity (1- ε). Note the Use of Logarithmic Y-Axis to Show Detail at Low Void Fractions.

Alternatively, Idelchik [5.20] recommends the slightly more complex equation of Bernshtein, et al., where the loss coefficient, λ_B, is given by

$$\lambda_B = \frac{1.53}{\varepsilon^{4.2}}\left(\frac{30}{\mathrm{Re}_B/(1-\varepsilon)} + \frac{3}{(\mathrm{Re}_B/(1-\varepsilon))^{0.7}} + 0.3\right), \tag{9}$$

and the Reynolds number, Re_B, is calculated as

$$\mathrm{Re}_B = \left(\frac{0.45\varepsilon^{0.5}}{\varepsilon} \right) \mathrm{Re}_p . \qquad (10)$$

The applicability of the Bernshtein correlation is limited to the range $0 \leq \mathrm{Re_B} \leq 10^4$ and the range $0.4 \leq \mathrm{Re_B} \leq 0.6$. The value of $\mathrm{Re_B}$ is compared with the value of $\mathrm{Re_c}$ as a function of ε in Fig. 5.28.

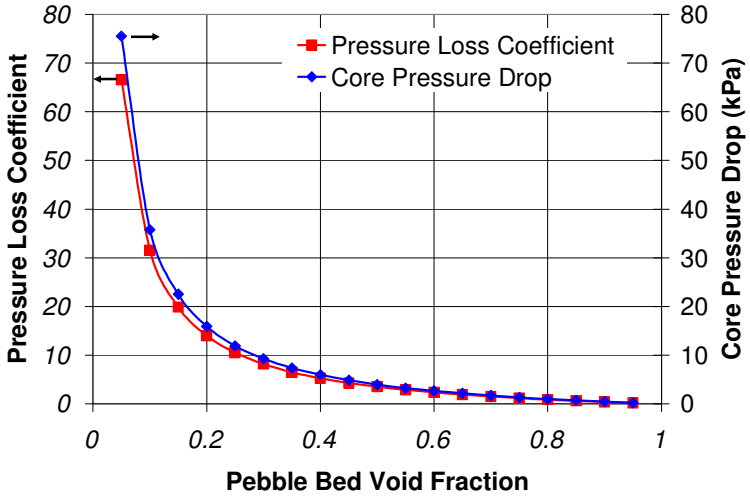

Fig. 5.27. Pressure Loss Coefficient Predicted by Ergun Correlation for a Reynolds Number of 1.5 x 10^6.

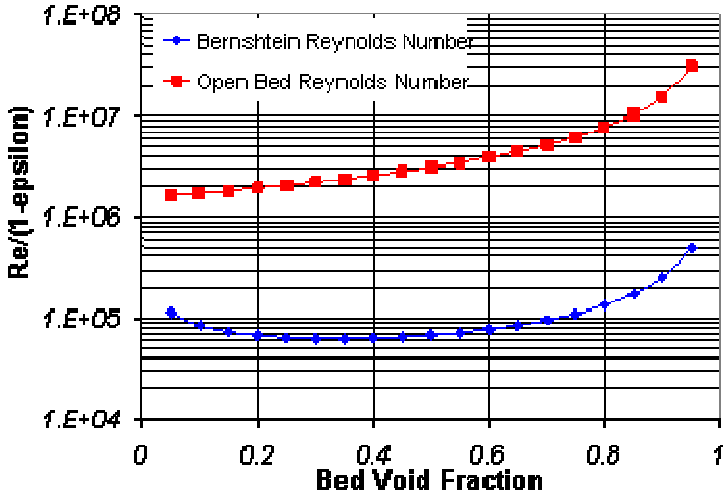

Fig. 5.28. Comparison of Open Bed and Pebble Reynolds Numbers Divided by the Quantity (1- ε). Note the Use of Logarithmic Y-Axis to Show Detail at Low Void Fractions.

Achenbach [5.21] recommends a modified Ergun equation that is more consistent with the experimentally observed asymptotic approach to a constant value at high Reynolds numbers (Re_c up to $5x10^5$), where the loss coefficient, λ_A, is given by

$$\lambda_A = 1.75 + \frac{320}{Re_c/(1-\varepsilon)} + \frac{20}{(Re_c/(1-\varepsilon))^{.4}}. \qquad (11)$$

The Achenbach equation is valid for Reynolds numbers in the range $250 \leq Re_c \leq 5x10^5$ and void fractions in the range $0.3 \leq \varepsilon \leq 0.8$ The pressure loss coefficients calculated using the Ergun, Bernshtein and Achenbach correlations are shown as a function of bed void fraction in Fig. 5.29. While the predictions of the three correlations converge to the same value for high void fractions there is significant deviation at low void fractions. However, it should be noted that a tetrahedral packed bed provides the maximum possible bed density or minimum possible void fraction, with a void fraction of approximately 0.3336.

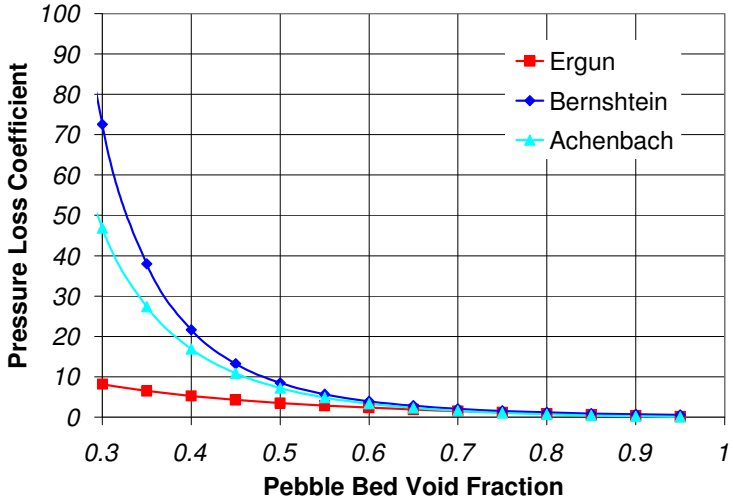

Fig. 5.29. Comparison of Pressure Loss Coefficient Predictions Using the Ergun, Bernshtein and Achenbach Correlations for a Reynolds Number of 1.5×10^6.

The Ergun equation provides the basic form for most other applicable pressure drop correlations. Eisfeld and Schnitzlein, in their extensive review and comparison of correlations from the literature with more than 2000 experimental data points found that the modified Ergun equations, such as those of Bernshtein and Achenbach, provide only small improvements to the accuracy of equations of this type. Most notably, these equations do not account for the effect of the walls that bound the pebble bed on the pressure loss coefficient. [5.22]

Eisfeld and Schnitzlein point out the two counteracting effects near the walls – the flow rate near the walls increases as a consequence of the higher void fraction in that region, but at the same time the friction at the wall reduces the velocity to zero. According to the boundary layer theory proposed by Eisfeld, the wall friction is expected to dominate at low Reynolds numbers and the voidage effect is expected to dominate at

high Reynolds numbers where the boundary layer thickness is reduced. Furthermore, the effects of the wall more strongly affect the pressure drop when the ratio of the core hydraulic diameter to the pebble diameter approaches 1.

To better approximate the effects of the bounding wall on the pebble bed pressure drop, Eisfeld and Schnitzlein [5.22] propose a modification of the correlation of Reichelt, which has the form

$$\lambda_R = \frac{1-\varepsilon}{\varepsilon^3}\left[\frac{K_1 A_w^2}{\left(\mathrm{Re}_p/(1-\varepsilon)\right)} + \frac{A_w}{B_w}\right], \tag{12}$$

where the wall correction terms are given by

$$A_w = 1 + \frac{2}{3\left(d_{h,c}/d_p\right)(1-\varepsilon)}, \tag{13}$$

and

$$B_w = \left[k_1\left(\frac{d_p}{d_{h,c}}\right)^2 + k_2\right]^2. \tag{14}$$

In the modified form, Eisfeld and Schnitzlein fit the empirical coefficients K_1, k_1, and k_2 to the extensive database collected in their study, arriving at values of 154, 1.15, and 0.87, respectively, for packed beds of spheres. The predicted pressure loss coefficient using the equation of Eisfeld and Schnitzlein is shown in comparison to the Ergun-type equations in Figure 5.30. While the current study does not provide an opportunity to assess the accuracy of the predictions, it should be noted that the Ergun and Bernshtein correlations bound the two other formulations presently considered.

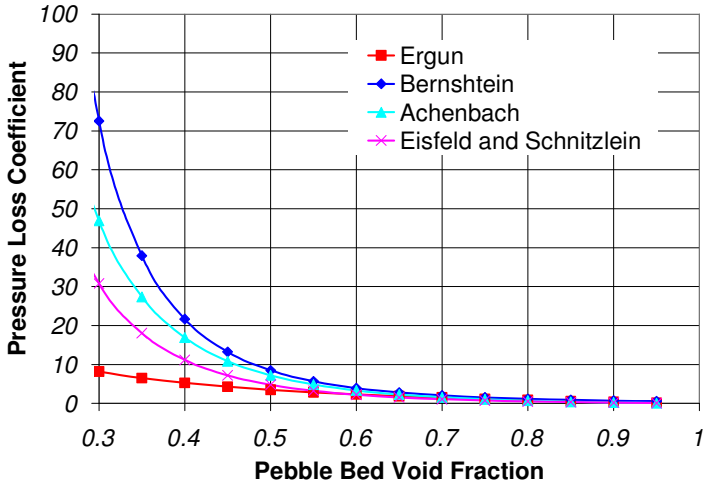

Fig. 5.30 Comparison of Pressure Loss Coefficient Predictions Using the Wall Correction Model of Eisenfeld and Schnitzlein with Predictions Using Correlations of the Ergun Type for a Reynolds Number of 1.5×10^6.

Others have proposed more rigorous approaches to the analysis of the effects of the bounding walls. One notable example is the work of Sodré and Parise, which offers a correction to the velocity terms in the Ergun formulation. [5.23] In general, these more rigorous approaches are limited to laminar flows with values of $Re/(1-\varepsilon) \leq 2000$ and the applicability of these methods to the highly turbulent flows expected in the pebble bed core is unknown. These more advanced models may be applicable during the natural convection phases of transients to be considered in future analyses.

5.2.2.2 Sensitivity Assessments for Prediction of Pebble Bed Pressure Loss Coefficient

In these studies, the uncertainty in the pressure drop is assumed to be a consequence of uncertainties in the pebble bed geometry, including the diameter of the pebble, the bed void fraction, the outer diameter of the annular bed, and the inner diameter of the annular bed. The sensitivities of the pressure loss coefficient were calculated using the Ergun and Bernshtein correlations for changes in pebble diameter and void fraction as well as for changes in the inner and outer core diameters. The sensitivities of the predicted pressure drop to changes in the four geometric parameters are shown for the Ergun equation in Fig. 5.31 and for the Bernshtein equation in Fig. 5.32.

For both models, the predicted pressure drop is an inverse power function of the pebble bed diameter and a fourth order polynomial function of the pebble bed void fraction. The predicted pressure drop is also a fourth order polynomial function of the core inner and outer diameter. Since the expected fractional error in the void fraction is much larger than the expected fractional error in the core dimensions, reasonable errors in the prediction of the pebble bed void fraction have the most significant impact on the calculated effective Reynolds number for both formulations. It should also be noted that the pressure drops predicted by the Bernshtein equation are a factor of two larger than the pressure drops predicted by the Ergun equation and that uncertainties associated with the correlations themselves may be larger than the uncertainties associated with errors in determination of geometric parameters.

To allow a more rigorous assessment of the sensitivity of the pressure loss coefficient prediction to uncertainty in the pebble bed void fraction, Achenbach proposed that the pressure loss coefficient, λ, could be represented by the asymptotic function

$$\lambda = \frac{A}{\left(\mathrm{Re}_c/(1-\varepsilon)\right)^n}, \tag{15}$$

where n is a function of Re_c such that

n=1 for $Re_c \rightarrow 0$
n=0 for $Re_c \rightarrow \infty$

Therefore, the relative variation of the pressure loss coefficient can be evaluated as a function of the relative variation of the void fraction by

$$\frac{\partial \lambda}{\lambda} = \frac{3-2\varepsilon}{1-\varepsilon}\frac{\partial \varepsilon}{\varepsilon}, \tag{16}$$

as shown in Fig. 5.33. As an example, this relationship indicates that for a randomly packed bed of spherical pebbles with an average void fraction of 0.5, an error in the prediction of the bed void fraction results in an error in the prediction of the pressure loss coefficient which is 4 times larger.

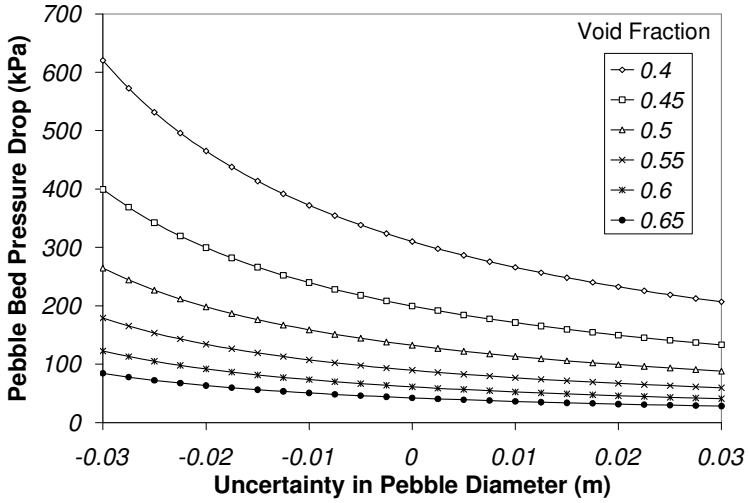

(a)

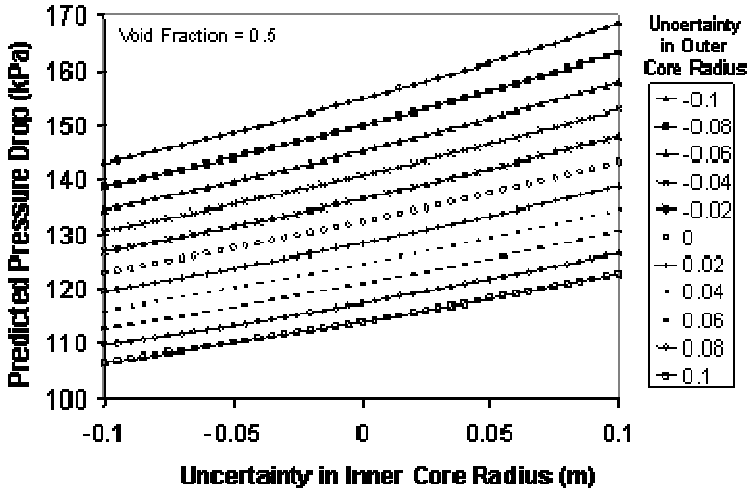

(b)

Fig. 5.31. Sensitivity of Pressure Drop Predictions Using the Ergun Correlation to Uncertainty in (a) Pebble Diameter and Void Fraction and (b) Core Inner and Outer Diameters.

Achenbach extended this approach to consider the limiting cases of the relative variation in the mass flow rate ($Re_c \to 0$ and $Re_c \to \infty$) which can be calculated as a function of the relative variation of the void fraction by

$$\frac{\partial \dot{m}}{\dot{m}} = \frac{3-\varepsilon(2-n)}{(2-n)(1-\varepsilon)} \frac{\partial \varepsilon}{\varepsilon}, \tag{17}$$

As shown in Fig. 5.34, as an example, this relationship indicates that for a randomly packed bed with a density of 0.5, an error in the predicted pebble bed void fraction results in an error in the predicted mass flow rate that is twice as large for high Reynolds numbers and as much as 5 times as large for low Reynolds numbers.

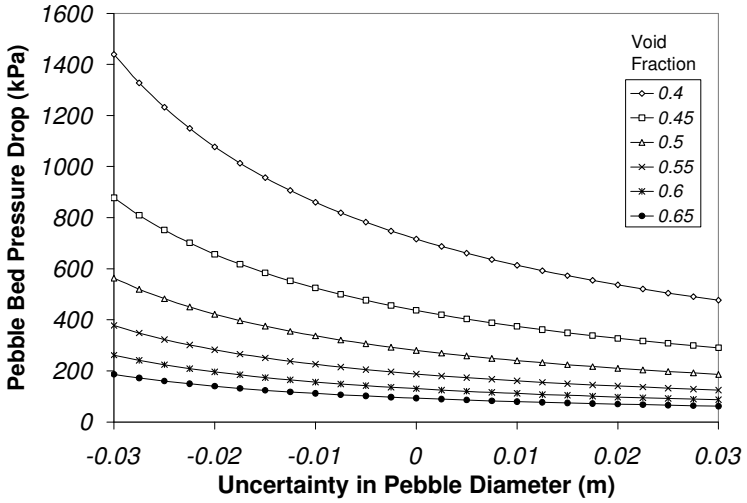

(a)

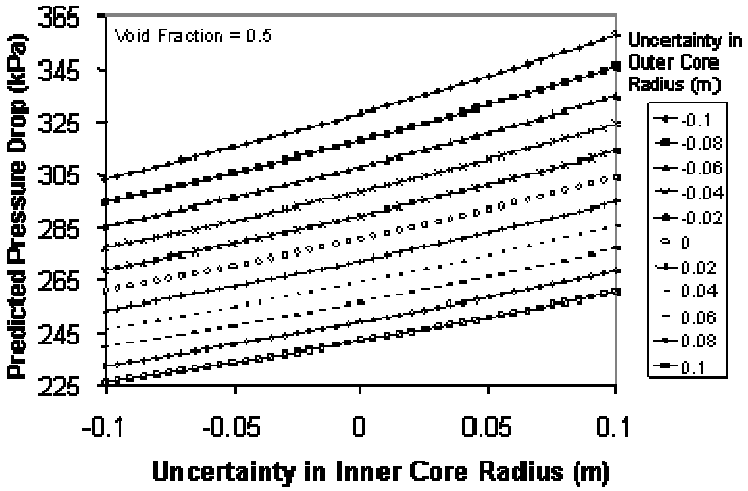

(b)

Fig. 5.32. Sensitivity of Pressure Drop Predictions Using the Bernshtein Correlation to Uncertainty in (a) Pebble Diameter and Void Fraction and (b) Core Inner and Outer Diameters.

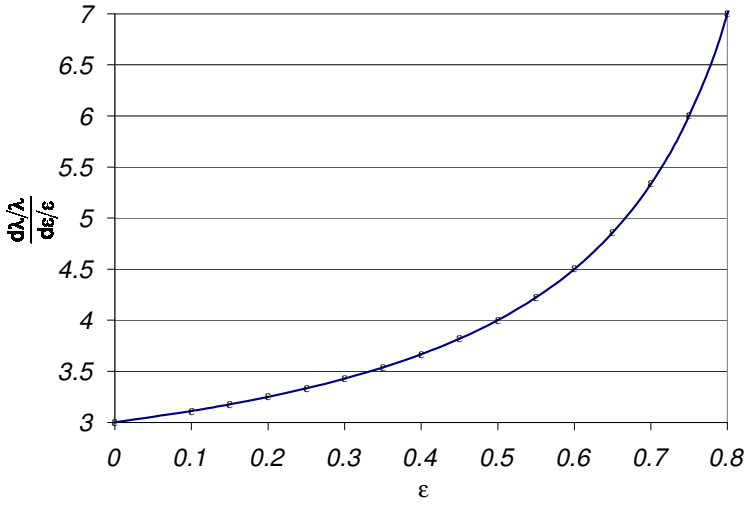

Fig. 5.33. Relative Sensitivity of the Pressure Loss Coefficient to Variation in Pebble Bed Void Fraction.

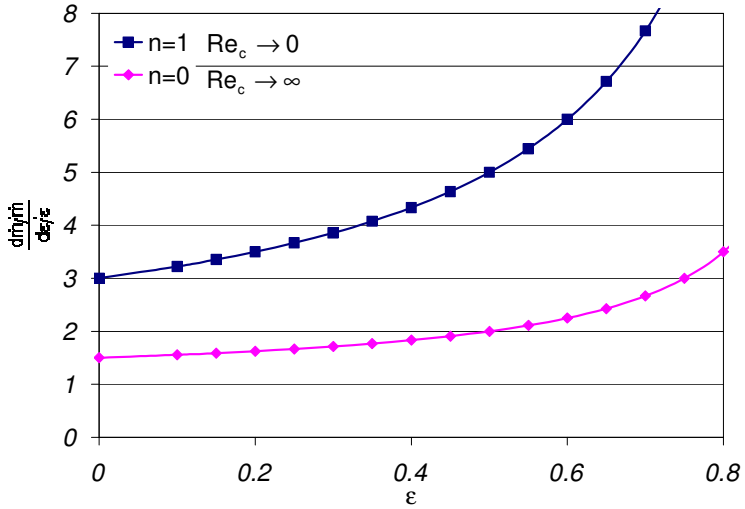

Fig. 5.34. Relative Sensitivity of the Mass Flow Rate to Variation in Pebble Bed Void Fraction.

In these studies, Achenbach's approach has been further extended to include the analysis of the effects of uncertainty in pebble and core dimensions. In order to fully account for the effects of these geometric parameters, the pebble bed void fraction must be assumed to be a function of the pebble diameter, d_p, and the core hydraulic diameter, $d_{h,c}$, of the form

$$\varepsilon = B + C\left(\frac{d_p}{d_{h,c}}\right)^2, \tag{18}$$

which follows the form recommended by Achenbach based on the data of Carman. [5.24]

The relative uncertainty in the pressure loss coefficient as a consequence of uncertainty in the pebble diameter can be evaluated by

$$\frac{\partial \lambda}{\lambda} = n\left(\frac{2C\left(d_p/d_{h,c}\right)^2}{1-B-C\left(d_p/d_{h,c}\right)^2}-1\right)\frac{\partial d_p}{d_p}. \tag{19}$$

If the constants C, B, and n are taken from the recommendation of Achenbach, [5.24] where

$$\begin{aligned} B &= 0.375 \\ C &= 0.78 \\ n &= \begin{cases} 0 & for\ \mathrm{Re} \to \infty \\ 1 & for\ \mathrm{Re} \to 0 \end{cases} \end{aligned} \tag{20}$$

then the ratio of the relative error in the pressure loss coefficient as a consequence of the relative error in the pebble diameter falls between the bounding curves shown in Fig. 5.35. Based on these limiting values, the relative variation in the pressure loss coefficient for an expected pebble diameter of 6.0 cm is on the same order of the relative variation in the pebble diameter for very low Reynolds numbers and approaches zero as Reynolds number increases. Based on this analysis, the relative uncertainty in the pebble bed void fraction has a much larger impact on the relative uncertainty in the pressure loss coefficient, but the uncertainty in the pebble diameter cannot be neglected if that uncertainty is large and the Reynolds numbers are relatively low.

The choice of B and C in the assumed function for the bed void fraction could impact the slope of the n=1 curve, however the function is asymptotic to one for positive values of C. Negative values of C would require a significant departure from the empirical value suggested by Achenbach [5.19] based on the experimental data of Carman.

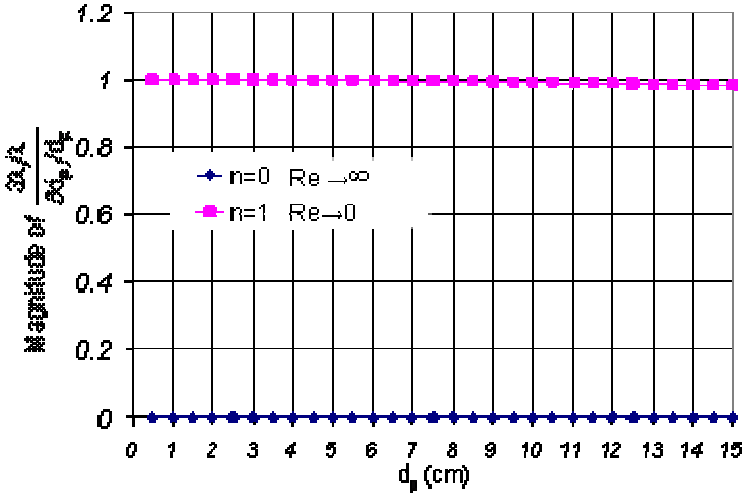

Fig. 5.35. Relative Sensitivity of the Pressure Loss Coefficient to Variation in Pebble Diameter.

Using the same approach, with the pebble bed void fraction defined by a function of the form

$$\varepsilon = B + C\left(\frac{d_p}{d_{h,c}}\right)^2, \tag{21}$$

the relative uncertainty in the pressure loss coefficient as a consequence of uncertainty in the core hydraulic diameter can be evaluated by

$$\frac{\partial\lambda}{\lambda} = n\frac{2C\left(d_p/d_{h,c}\right)^2}{1-B-C\left(d_p/d_{h,c}\right)^2}\frac{\partial d_{h,c}}{d_{h,c}}. \tag{22}$$

If Achenbach's recommended values of B,C, and n are again assumed, then the ratio of the relative error in the pressure loss coefficient as a consequence of the relative error in the core hydraulic diameter falls between the bounding curves shown in Fig. 5.36. Although the n=1 function has a sharp peak at very small core hydraulic diameters, the function asymptotically approaches a value of zero for hydraulic diameters in the range of interest for pebble bed reactor cores. Therefore, a relative error in the core hydraulic diameter would be expected to produce a negligible relative error in the prediction of the pressure loss coefficient. As a consequence of the asymptotic behavior of the function, the selection of values for the constants B and C do not significantly impact the ratio of relative variations in the range of hydraulic diameters of interest.

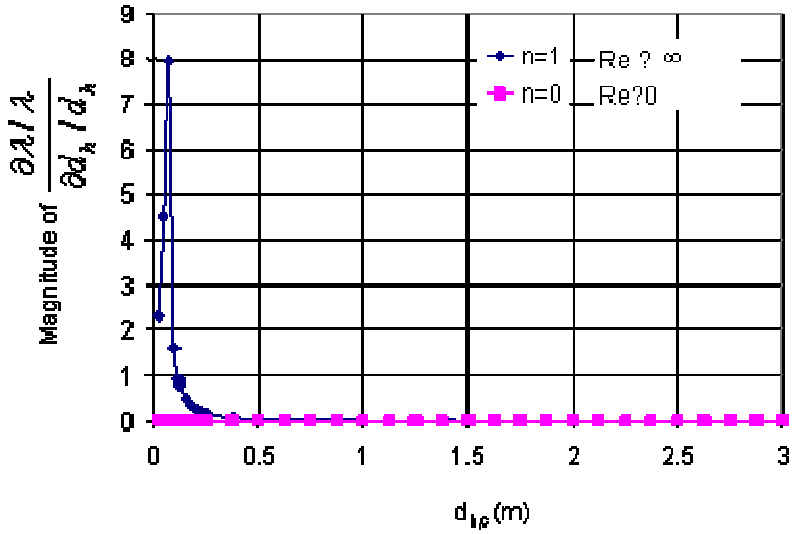

Fig. 5.36. Relative Sensitivity of the Pressure Loss Coefficient to Variation in Core Hydraulic Diameter.

5.2.2.3 Summary of Pebble Bed Pressure Loss Coefficient Prediction Uncertainties

In these sections, the sensitivity of pebble bed pressure loss coefficient predictions has been evaluated for uncertainties related to pebble diameter, pebble bed void fraction,

core hydraulic diameter, and choice of model formulation. The largest uncertainties in predictions relate to the uncertainty in the pebble bed void fraction as a consequence of the randomly packed nature of the bed. Large uncertainties are also associated with the choice of model formulation, regardless of the Reynolds number of the flow. More complex models that account for wall effects may improve accuracy of predictions, but results appear to fall within the band of results from simpler infinite bed models. At low values of the Reynolds number, the uncertainty in the pebble radius may be significant, but this effect vanishes with increasing Reynolds number. The uncertainty in the core hydraulic diameter would only have a significant impact on pressure loss coefficient predictions in pebble bed reactor cores with hydraulic diameters an order of magnitude smaller than assumed for the baseline design in this study.

5.2.3 Prediction of Pebble Bed Forced Convective Heat Transfer Coefficients

Accurate predictions of pebble surface temperature, and, hence, pebble centerline temperature, require knowledge of the heat generation rate within the pebble and the heat transfer coefficient associated with the local geometric configuration and mass flow rate, as shown by

$$T_{surface} = \frac{q''}{h} + T_{Bulk}\,, \tag{23}$$

where q" is the surface heat flux and h is the heat transfer coefficient.

As in the previous section's discussion of models of pressure loss coefficients, heat transfer coefficient correlations typically require that the diameter of the pebbles be significantly smaller than the effective diameter of the reactor core, which is consistent with the nominal pebble bed concept. Furthermore, the pebbles should again be of uniform size and uniformly distributed within the core for the simplest correlations to be applied. While the diameter and distribution of the pebbles are likely to be subject to significant uncertainty in a real system and these correlations should not be expected to provide an accurate prediction of the local thermal hydraulic characteristics within the three-dimensional core, the application of correlations based upon these assumptions does provide a means of bounding the expected values for the forced convective heat transfer coefficient as well as the impact of local uncertainties in geometric configuration.

5.2.3.1 Standard Correlations for Forced Convective Heat Transfer Coefficients in Pebble Beds

With these assumptions and constraints, the convective heat transfer coefficient within the porous bed can be calculated using the well known Eckert correlation [5.25] for the Nusselt number:

$$Nu = \frac{hd_P}{k} = 0.8\,\mathrm{Re}_p^{0.7}\,\mathrm{Pr}^{1/3}\,, \tag{24}$$

where Re_p, is the pebble Reynolds number given by:

$$\mathrm{Re}_p = \frac{\rho u d_P}{\mu}. \tag{25}$$

The heat transfer coefficient, h, is simply calculated by

$$h = \frac{Nu \cdot k}{d_p}. \tag{26}$$

The Eckert equation is generally applicable only in the laminar regime for low Reynolds numbers and moderate values of bed void fraction since this formulation does not explicitly account for the impact of the void fraction on the heat transfer mechanisms. However, this simplistic form, much like Achenbach's simple power function formulation for the pressure loss coefficient, can be useful for the assessment of sensitivity of the heat transfer coefficient to uncertainties in other parameters.

The correlation proposed by Gnielinski [5.26] is widely used for analysis of heat transfer within pebble bed systems with volumetric heat addition. The model is an extension of the heat transfer equations of a flat plate, and it was first applied to a single sphere before further extension to packed beds of spheres. Indeed the formulation assumes that the Nusselt number of a single sphere, Nu_s, can be related to the Nusselt number of the packed bed by an arrangement factor, which is a function of the bed void fraction.

$$Nu = \frac{h d_{h,c}}{k} = f(\varepsilon) Nu_s, \tag{27}$$

where

$$f(\varepsilon) = 1 + 1.5(1 - \varepsilon). \tag{28}$$

The Nusselt number for a single sphere is given by

$$Nu_s = 2 + \sqrt{Nu_l^2 + Nu_t^2} \tag{29}$$

where the laminar part is given by

$$Nu_l = 0.664 \,\mathrm{Pr}^{1/3} \left(\frac{\mathrm{Re}}{\varepsilon} \right)^{1/2}, \tag{30}$$

and the turbulent part is given by

$$Nu_t = \frac{0.037\,\mathrm{Pr}\left(\frac{\mathrm{Re}}{\varepsilon}\right)^{0.8}}{1+2.443\left(\frac{\mathrm{Re}}{\varepsilon}\right)^{-0.1}\left(\mathrm{Pr}^{2/3}-1\right)}. \qquad (31)$$

The Gnielinski formulation is valid for $2 \le \mathrm{Re} \le 10^4$, for $0.7 \le \mathrm{Pr} \le 10^4$, and for $0.26 \le \varepsilon \le 0.935$, which nearly encompasses the expected bounds of operation for a pebble bed reactor core. The Gnielinski formulation is compared with the Eckert correlation as a function of Reynolds number for three different pebble bed void fractions in Fig. 5.37. The two formulations provide comparable predictions for turbulent heat transfer (Re>~1000) in densely packed pebble beds ($\varepsilon \approx 0.35$). In more open packings or at low Reynolds numbers, accounting for the void fraction by using the Gnielinski model results in a slightly larger deviation from the simpler Eckert correlation.

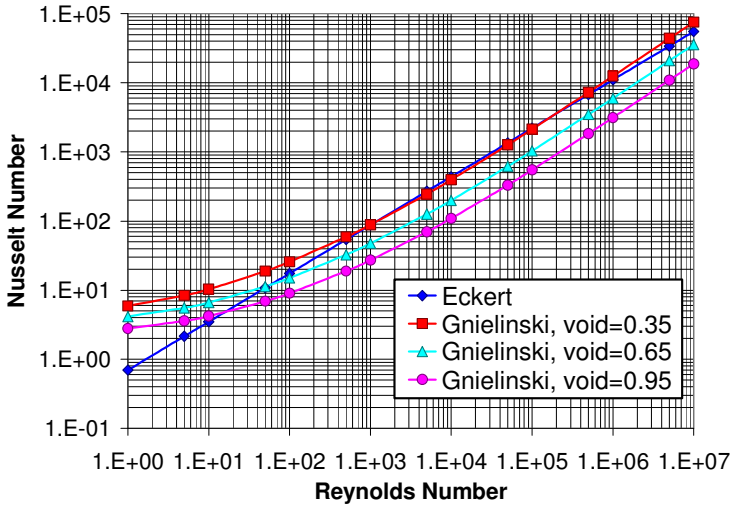

Fig. 5.37. Predicted Nusselt Number Using the Eckert and Gnielinski Models as a Function of Reynolds Number

5.2.3.2 Sensitivity Assessments for Prediction of Pebble Bed Heat Transfer Coefficient

Assuming that validated equation sets are identified which reduce correlation error to near-zero, uncertainty in the prediction of the heat transfer coefficient within the pebble bed core will be a consequence of uncertainties in the pebble diameter, the pebble bed void fraction, and the flow velocity within the bed, which is directly related to the uncertainty in the ability to predict the core pressure drop. The dependence of the heat transfer coefficient, h, on the pebble diameter and the pebble bed void fraction was calculated using the correlations of Eckert and Gnielinski. Results of these calculations are shown in Figs. 5.38 and 5.39 respectively. As one would expect, the impact of uncertainty in these parameters is clearly larger when the value of the parameter is small.

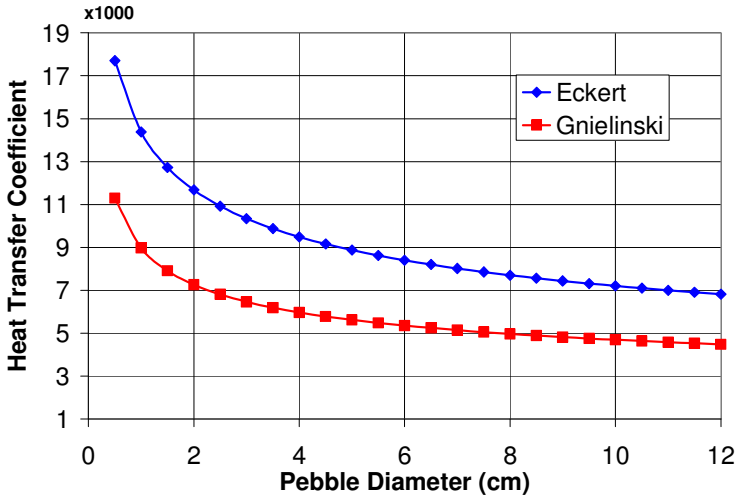

Fig. 5.38. Predicted Heat Transfer Coefficient as a Function of Pebble Diameter using Correlations of Eckert and Gnielinski (assumed void fraction of 0.5).

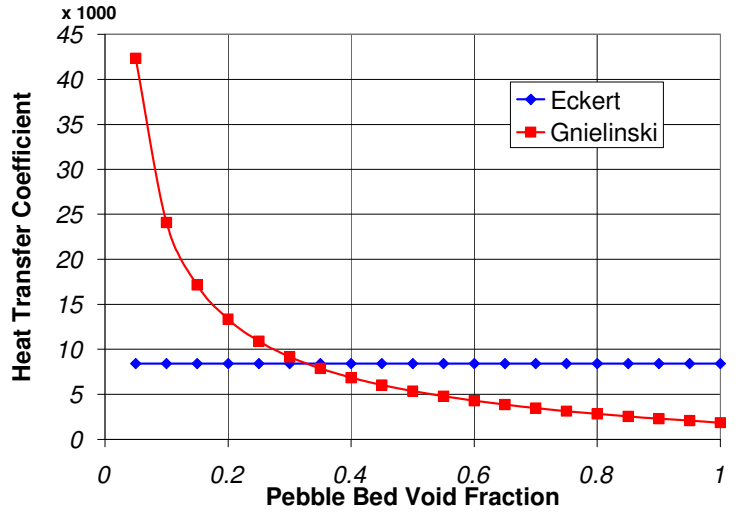

Fig. 5.39. Predicted Heat Transfer Coefficient as a Function of Pebble Bed Void Fraction using Correlations of Eckert and Gnielinski (assumed pebble diameter of 6 cm).

The more rigorous procedure outlined by Achenbach for the assessment of sensitivities in the pressure loss coefficient predictions can be applied to the heat transfer coefficient if the simple correlation of Eckert,

$$Nu = \frac{hd_P}{k} = 0.8\,\mathrm{Re}_p^{0.7}\,\mathrm{Pr}^{1/3}, \tag{32}$$

is assumed to be applicable. The relative variance in the heat transfer coefficient as a consequence of the relative variation in the pebble diameter is given by

$$\frac{\partial h}{h} = -0.3\frac{\partial d_p}{d_p}. \tag{33}$$

Therefore, any relative uncertainty in the pebble diameter can be expected to result in a relative uncertainty in the heat transfer coefficient that is three tenths the magnitude of the uncertainty in the core mass flux.

The relative variance in the heat transfer coefficient as a consequence of the relative variation in the core mass flux, $G_0 = \rho u$, is given by

$$\frac{\partial h}{h} = 0.7\frac{\partial G_0}{G_0} \tag{34}$$

Therefore, any relative uncertainty in the core mass flux results in a relative uncertainty in the heat transfer coefficient that is seven tenths the magnitude of the uncertainty in the pebble diameter.

Since the Eckert equation does not account for the effect of the pebble bed void fraction, the effect of relative variations in that parameter cannot be calculated in this fashion. The more qualitative approach using the Gnielinski correlation as shown in Figs. 5.38 and 5.39 must be employed for this assessment. Based on the results shown in Figs. 5.38 and 5.39, the effects of relative variation in pebble bed void fraction appear to be more significant than the effects of comparable relative variations in pebble diameter or core mass flux.

5.2.3.3 Summary of Pebble Bed Heat Transfer Coefficient Prediction Uncertainties

In these sections, the uncertainty in the prediction of pebble bed heat transfer coefficients has been evaluated as a consequence of uncertainties in pebble diameter, core mass flux, and pebble bed void fraction. The effect of choice of model formulation is also considered, but is much less severe than for the prediction of the pebble bed pressure loss coefficient. Relative uncertainty in core mass flux is more than twice as significant as the relative uncertainty in pebble diameter in the prediction of pebble bed heat transfer coefficients. Although the impact of relative uncertainty in the pebble bed void fraction cannot easily be calculated directly, qualitative comparisons of Fig. 5.38 and 5.39 appear to indicate that relative uncertainty in the void fraction may be most significant factor in the accurate prediction of pebble bed heat transfer coefficients.

References

5.1 R. Kapernick, personal communication, Los Alamos Nuclear Laboratory, October 15, 2005.

5.2 S. Maruyama et. al, "Evaluation of Core Thermal and Hydraulic Characteristics of HTTR," Nuclear Engineering and Design, 152, p 183-196, 1994. (japan_th_flow_network.pdf)
5.3 H.G. Olson, H.L. Brey, "The Fort St. Vrain Hugh Temperature Gas-Cooled Reactor: X. Core Temperature Fluctuations," Nuclear Engineering and Design, 72 p 125-137, 1982.(hardcopy)
5.4 B.J. Marsden, "Nuclear Graphite for High Temperature Reactors," AEA Technology, Risely, Warrington, UK. (graphite.pdf)
5.5 H. Kaburaki, "Leakage Flows in High-Temperature Gas-Cooled Reactor Graphite Fuel Elements," Journal of Nuclear Science and Technology, v 22, n 5, p 387-397, May 1985. (kaburaki_leakage.pdf)
5.6 H. Kaburaki, "Effect of Crossflow on Flow Distribution in HTGR Core Column," Journal of Nuclear Science and Technology, v 24, n 7, p 516-525, Jul 1987. (kaburaki_crossflows.pdf)
5.7 K. Suzuki, "Analysis of Flow Distribution in Experimental VHTR," First Atomic Power Industry Group, n 102, p 2-8, 1982.
5.8 T. Takizuka, "Research on Crossflow in VHTR Core. (I) Two-Block Crossflow Experiments," Journal of the Atomic Energy Society of Japan, v 27, n 4, p 347-356, Apr 1985.
5.9 H. Kaburaki, "Leakage Flow Characteristics of Highly-Effective Graphite Seal Mechanism for HTGR Core Support Blocks," Journal of Nuclear Science and Technology, v 25, n 1, p 92-99, Jan 1988. (kaburaki_seal_leakage_characteristics.pdf)
5.10 H. Kaburaki, "Leakage Flow Experiments of Seal Mechanism for HTGR Core Support Blocks," Journal of the Atomic Energy Society of Japan, v 30, n 5, p. 434-442, May 1988.
5.11 H. Kaburaki, "Leakage Flows in High-Temperature of Seal Mechanism for HTGR Core Support Blocks," Journal of Nuclear Science and Technology, n9, p 742-747, Sep 1987. (support_block_leaks.pdf)
5.12 H.G. Groehn, "Estimate of Cross Flow in High Temperature Gas-Cooled Reactor Fuel Blocks," Nuclear Technology, vol 56, Feb. 1982.
5.13 Gas Turbine-Modular Helium Reactor (GT-MHR) Conceptual Design Report, General Atomics Report 910720, July 1996.
5.14 General Atomic, personal communication, February 2006.
5.15 P.E. MacDonald, "NGNP Point Design – Results of the Initial Neutronics and Thermal-hydraulic Assessments During FY-03," INeel/EXT-03-00870, Idaho National Engineering and Environmental Laboratory, September 2003.
5.16 A. Walter, A. Shultz, G. Lohnert, "Comparison of Two Models for Pebble Bed Modular Reactor Core Coupled to a Brayton Cycle," 2nd Int. Topical Meeting on High Temperature Reactor Technology, Beijing, China, Sept 2004.
5.17 Thermophysical Properties of Fluid Systems, NIST Chemistry Webbook, July 31, 2006 from http://webbook.nist.gov/chemistry/fluid/.
5.18 *Chem. Eng. Prig.*, **48**. 93, 1953.
5.19 E. Achenbach, "Pressure drop, forced convective, free convective, and radiant heat transfer of pebble beds," *Post Accident Debris Cooling: Proceedings of the*

Fifth Post Accident Heat Removal Information Exchange Meeting, Karlsruhe, Germany, July, 1982.

5.20 I. Idelchik, *Handbook of Hydraulic Resistance,* Berlin: Springer-Verlag, 1986.

5.21 E. Achenbach, "Pressure drop, forced convective, free convective, and radiant heat transfer of pebble beds," *Post Accident Debris Cooling: proceedings of the Fifth Post Accident Heat Removal Information Exchange Meeting*, Karlsruhe, Germany, July, 1982.)

5.22 B. Eisfeld and K. Schnitzlein, "The Influence of Confining Walls on the Pressure Drop in Packed Beds," *Chemical Engineering Science,* **56**, 2001, pp. 4321-4329.

5.23 (J. Sodré and J. Parise, "Fluid flow pressure drop through an annular bed of spheres with wall effects," *Experimental Thermal and Fluid Science*, **17**, 1998, pp. 265-275).

5.24 P. C. Carman, "Flow through Granular Beds," *Trans. Inst. Chem. Engrs.,* **15**, 1937, pp.150-166.

5.25 W. Rosenhow and H. Choi, *Introduction to Heat and Mass Transfer,* New York: McGraw-Hill, 1950.

5.26 V. Gnielinski, "Gleichungen zur Berechnung des Wärme- und Stoffaustausches in durchströmten ruhenden Kugelschütten bei mittleren und großen Peclet-Zahlen," *Verfahrenstechnik*, **12** (6), 1978, pp. 363-366.

6.0 Conclusions

To date, a select set of VHTR/NGNP events have been evaluated to identify phenomena expected to occur during the transients and that could be of importance to model in the thermal-fluid design and safety analyses tools due to their effect on the performances and safety consequences. In FY06 the focus was on water-ingress, a control rod withdrawal ATWS and the hydrogen plant side aspect. This set of sequences was chosen to complement those evaluated in FY05: the protected station blackout, the large break depressurization with shutdown and the load change. These events span the normal operating, off-normal to the design-basis and the beyond-design basis spectra. A range of initiators are involved from leaks to loss of electrical power to reactivity transients. Two generic designs, one for a PBR and one for a PMR were considered. The set of phenomena identified from these sequences for inclusion in the modeling needs should be quite broad and encompassing. The range of behavior should include the limiting envelope. However, there remains a need to:

(i) Consider an indirect cycle plant design and a water-cooled RCCS. The two generic designs which have been utilized in the PIRT development have both been direct cycle plant. Moreover as a first iteration, both designs were assumed to utilize an air-cooled RCCS.

(ii) Pressure upset initiators should be assessed. Phenomena relating to pressure perturbation such as PCU check valve failures or problems in the turbo-machinery could selectively broaden the list of modeling needs. Another initiator category which would fall into this category are seismic initiators. In particular, this would perhaps produce phenomena relating to core reconfigurations.

(iii) Additional definition to the phenomena matrix outlined in the PIRTs would add sub-phenomena with an additional level of detail to the modeling needs in the codes. The phenomena of core flow distribution would require a sub-level on the treatment of the core bypass flow in this scheme.

Core flow distribution and bypass was identified as an area for that it would be beneficial to perform sensitivity studies to assess the various factors that affect the magnitude and distribution of this flow. Modeling development needs have been preliminarily determined based on the results of these studies. The conclusions are summarized below.

6.1 PMR Core Flow Distribution Modeling Needs

Based on the calculations presented above, a list can be compiled identifying the most important phenomena that contribute to uncertainty in core coolant temperature.

The goal of calculations in this work was to quantify the effect of fuel coolant temperature of variation in four key parameters. The parameters are the leakage resistance at the inter-column gap seals at the core support structure, the width of the gap between two stacked elements, the leakage resistance past an inserted control rod, and the

width of the inter-column gap. The base case is the GT-MHR core with nominal inter-column gap flow of 10 percent, control rod hole flow of 1.5 percent, and fuel coolant channel flow equal to the balance. The results show that effectiveness of the inter-column gap seals at the core support structure has the greatest effect on fuel element coolant temperature uncertainty. This is the most sensitive leakage resistance. Next in importance is the gap size between stacked elements at the core periphery that results in an uncertainty about half as great as that for the inter-column gap seals. For these two locations, flow leakage at beginning of life can probably be well characterized through laboratory experiments. The Japanese had an experiment program to do this for the HTTR. In comparison to these two locations, the uncertainty in leakage past control rods and uncertainty in inter-column gap thickness result in a fuel coolant temperature uncertainty of about an order of magnitude smaller.

The ranking of priorities based on the numerical results in Table 5.9 is preliminary as it is dependent upon the base case. This is certainly designer dependent. One may want to investigate the impact of design related choices such as the type of graphite, the design of core support seals, layout of coolant holes in graphite elements, and flux and temperature distributions across the core on the flow split between fuel coolant holes and bypass channels (control rod holes and inter-column gaps) before considering the effect of uncertainties.

The sensitivity of fuel coolant temperature to an individual effect is dependent in part on the design definition. For example, both the inter-column gap axial flow resistance and the leakage resistance of the block seal at the base of the inter-column gap are key factors influencing the bypass flowrate. While block seal performance is rated most important in this work, increased gap resistance due to gap narrowing would act as an upstream seal, diminishing the sensitivity of temperatures to block seal leakage resistance. An example of another important factor is the termination of control rod holes at the core support. In this work, we assumed these holes terminate blind at the core support. If the designer choose otherwise, a significant new path for leakage to the outlet plenum exists. Thus, rankings in general are sensitive to the base case definition. Without a base case definition that reflects the final core design, the usefulness of rankings is diminished.

Furthermore, the correlations used in this study for leakage are based on analytical derivations and have their own assumptions. The correlations at issue are those used for leakage from a coolant channel to an inter-column gap, from a coolant channel to a control rod hole, and from a control rod hole to an inter-column gap. A set of experiments is needed to either establish the uncertainty on these correlations or to develop new ones highly tuned to the geometric specifics of the graphite elements in the final core design. CFD simulation of leakage hydraulics would be useful but only after the geometry of the leakage path has been characterized. Since this path depends on the mating of ultimately unobservable surfaces, it is difficult to imagine how this geometry could be characterized directly. On the other hand, measuring the hydraulic consequences through an experiment is straight forward.

Finally, there is the question of the dimensions of leakage paths in the base case. The nominal gap thickness in each of the leakage paths listed above is highly uncertain at this time. The thickness depends on how surfaces are prepared, the precision to which elements are machined, and the type of graphite and the characteristics of how it deforms over life. All these factors influence the mating of inter-element surfaces in a column of stacked elements constrained at the top and by nearest neighbors. A potential range of the gap thickness between stacked elements comes from [5] where it is noted that the gap thickness used for HTTR calculations is a factor of ten smaller than the value given there for the Fort St. Vrain Reactor. Additionally, the size of the leakage gaps both for between stacked elements and in core support seals is a function of the type of graphite and the local flux and temperature gradients. Clearly, these effects must be quantified as to their role in coolant bypass uncertainty.

6.2 PBR Core Flow Distribution Modeling Needs

The analyses presented in section 5.2 clearly indicate that accurate knowledge of the distribution of pebbles within the pebble bed reactor core in the form of a core average void fraction or, preferably, a core void fraction distribution is essential to accurately predicting the thermal hydraulic performance of the reactor core during normal operating conditions. An experimental or numerical assessment of the probability distribution function describing the pebble void fraction distribution for pebbles (appropriately scaled diameter) moving through an annular column (appropriately scaled diameter) is needed. Scaled numerical or physical experiments could potentially be used by maintaining the ratio of the pebble diameter to the core hydraulic diameter.

The variation between conventional correlations for pebble bed pressure loss coefficients and heat transfer coefficient is significant. For the pressure drop loss coefficient, the effect of the wall is lost in the uncertainty. Therefore, appropriately scaled, instrumented, and documented experimental data is needed to identify and validate suitable correlations or, if necessary, develop new system-specific correlations for those parameters. Furthermore, it is expected that within a pebble bed reactor core the Reynolds number based on pebble diameter may approach or even exceed a value of 10^5, which approaches or surpasses the limit of applicability or at least validation for most conventional pebble bed correlations. Any potential new validation experiments completed to support the development of a pebble bed high temperature gas-cooled reactor must include data for values of the Reynolds number greater than 10^5.

All pebble bed correlations assume a uniform distribution of pebbles at some constant density within the bed. In reality, cavitation or bridging may occur within the pebble bed as old pebbles are extracted and new pebbles are added. The effects of these granular flow phenomena on thermal hydraulic performance are unquantified. Appropriately scaled experimental or numerical assessments of both the probability of occurrence and the impact of the development of such regions within the bed on the reactor's thermal hydraulic performance are needed.

Finally, the work reported herein considers only the correlations of importance in steady state operation. Future assessments of uncertainty impacts must include the correlations important to transient analyses such as natural and mixed convection heat transfer coefficients, radiation heat transport and conduction heat transport.

References

6.1 H. Kaburaki, Leakage Flows in High-Temperature Gas-Cooled Reactor Graphite Fuel Elements", Journal of Nuclear Science and Technology, v 22, n 5, p 387-397, May 1985. (kaburaki_leakage.pdf)

Appendix I: PMR Core Flow Network Representation

I.1 Conservation Equations

The flow network is composed of an array of unit flow networks where the unit network represents the flow of conserved quantities around a single block. Since our core model is a single row of columns, with each column a stack of blocks, the flow network is a two-dimensional construct of linked unit networks. Below we give the conservation balances for the unit flow network for the block in column *l* at axial level *k*. Presently, the model momentum equation accounts for only shear stress pressure drop in a channel. Entrance and exit losses and pressure change with coolant acceleration are not included. Inclusion of these terms at a later time is a simple matter. Appropriate correlations for entrance and exit losses would first need to be identified.

A. Channel Coolant Node Mass Balance

Coolant channel node $node_{chan}{}^{l,k}$ shown in Fig. 5.10 situated at the top of the block in column *l* at block axial level *k*. Performing a mass balance on the flows shown in Fig. 5.9 into and out of this node gives

$$0 = w_{chan}{}^{l,k-1} - w_{leak-in}{}^{l,k} - w_{leak-out}{}^{l,k} - w_{chan}{}^{l,k} - w_{leak-cntrl}{}^{l,k} \tag{I.1}$$

where

$w_{chan}{}^{l,k}$ = flowrate through all the coolant channels in the block,

$w_{leak\text{-}in}{}^{l,k}$ = leakage flowrate on the inboard side of the interface gap between blocks at axial levels *k-1* and *k* in column *l*, taken as a positive quantity when emanating from the coolant channels on trasnit to the gap,

$w_{leak\text{-}out}{}^{l,k}$ = same as $w_{leak\text{-}in}{}^{l,k}$, but on the outboard side, and

$w_{leak-cntrl}{}^{l,k}$ = flowrate from coolant channel to control rod hole when present. Assumed positive when flow is from the coolant hole to the control rod hole.

B. Gap Coolant Node Mass Balance

Gap node $node_{gap}{}^{l,k}$ shown in Fig. 5.10 is sitiated on the inboard side of the block in column *l* at block axial level *k*. Performing a mass balance on the flows shown in Fig. 5.9 into and out of this node gives

$$0 = w_{gap-lat}{}^{l-1,k} - w_{gap-lat}{}^{l,k} + w_{leak-in}{}^{l,k} + w_{leak-out}{}^{l-1,k} + w_{gap-ax}{}^{l,k-1} - w_{gap-ax}{}^{l,k} \tag{I.2}$$

where the mass flowrates are shown in Fig. 5.9 and are defined as

$w_{gap\text{-}lat}^{l,k}$ = lateral flow, taken as a positive quantity when leaving the gap node, on transit to the next outboard gap node, and

$w_{gap\text{-}ax}^{l,k}$ = axial flow, taken as a positive quantity when leaving the gap node, on transit to the next gap node below it. This flow is assumed to be distributed between the gaps that subtend the 90 degree sector that occupies the lower right quadrant of block l,k and the 90 degree sector that subtends the upper right quadrant of block l-1,k.

C. Inter-Column Gap Coolant Axial Momentum Balance

That component of the coolant that flows axially down the gap between blocks is assumed to transit between gap nodes. The flow network diagram in Fig. 5.11 shows flowrate $w_{gap\text{-}ax}^{l,k}$ flowing between nodes $node_{gap}^{l,k}$ and $node_{gap}^{l,,k+1}$. A momentum balance between these nodes gives

$$0 = P_{gap}^{l,k} - K_{gap-ax}^{l,k}\, w_{gap-ax}^{l,k}\, |w_{gap-ax}^{l,k}|^{1-n} - P_{gap}^{l,k+1} \tag{I.3a}$$

where

$$K_{gap-ax}^{l,k} = \frac{C\, L_{ax}^{l,k}}{2\rho\, D_{h-gap-ax}^{l,k} (A_{gap-ax}^{l,k})^2} \left(\frac{\mu\, A_{gap-ax}^{l,k}}{D_{h-gap-ax}^{l,k}} \right)^n ,$$

$$D_{h-gap-ax}^{l,k} = \frac{4 A_{gap-ax}^{l,k}}{P_{w-gap-ax}^{l,k}} , \tag{I.3b}$$

$$A_{gap-ax}^{l,k} = 3fg + \frac{\sqrt{3}}{2} g^2 ,$$

$$P_{w-gap-ax}^{l,k} = 6f$$

where $A_{ax}^{l,k}$ and $P_{w\text{-}ax}^{l,k}$ are the crossectional area and wetted perimeter, respectively, of the participating coolant shown as the shaded region in Fig. I.1 and f and g are defined in Fig. I.2. As appears in Fig. I.1, in representing the hydraulics of the coolant in the gaps, we have lumped in with it the coolant in the single triangle and the two half triangles formed by the vertexes of the blocks that lie at the corners of the rectangular gaps. An expression for the ratio of this area to gap area for a unit cell for typical dimensions of g = 0.15 in. and f = 14 in. gives the ratio of these areas as 0.003. Thus, the combined fluid behaves predominalty as the fluid in the gap.

D. Inter-Column Gap Coolant Lateral Momentum Balance

That component of the coolant that flows laterally in the gap between blocks is assumed to transit between gap nodes. The flow network diagram in Fig. 5.11 shows

flowrate $w_{gap\text{-}lat}^{l,k}$ flowing between nodes $node_{gap}^{l,k}$ and $node_{gap}^{l+1,k}$. A momentum balance between these nodes gives

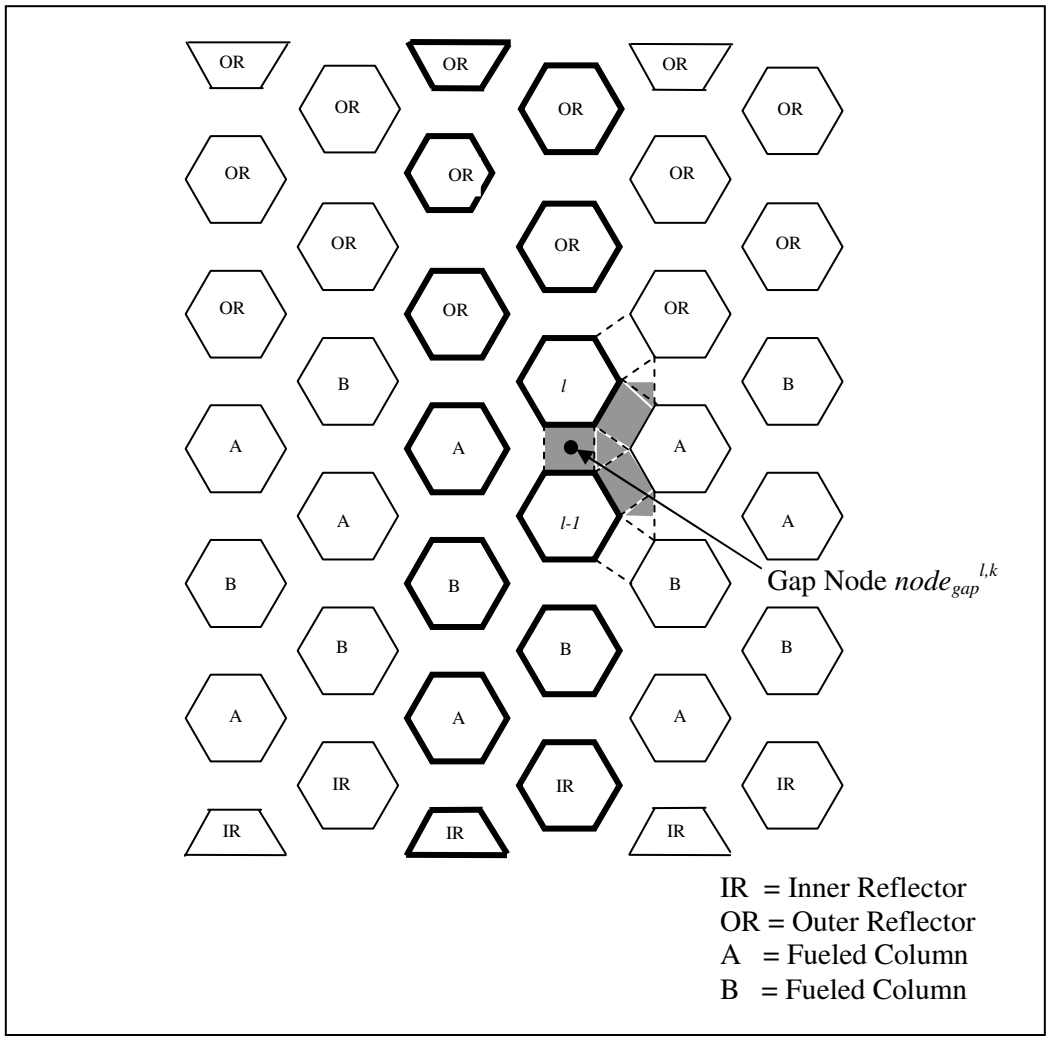

Fig. I.1 Coolant Participating in Axial Momentum Balance between Gap Nodes $node_{gap}^{l,k}$ and $node_{gap}^{l,k+1}$. Coolant is shown as shaded region.

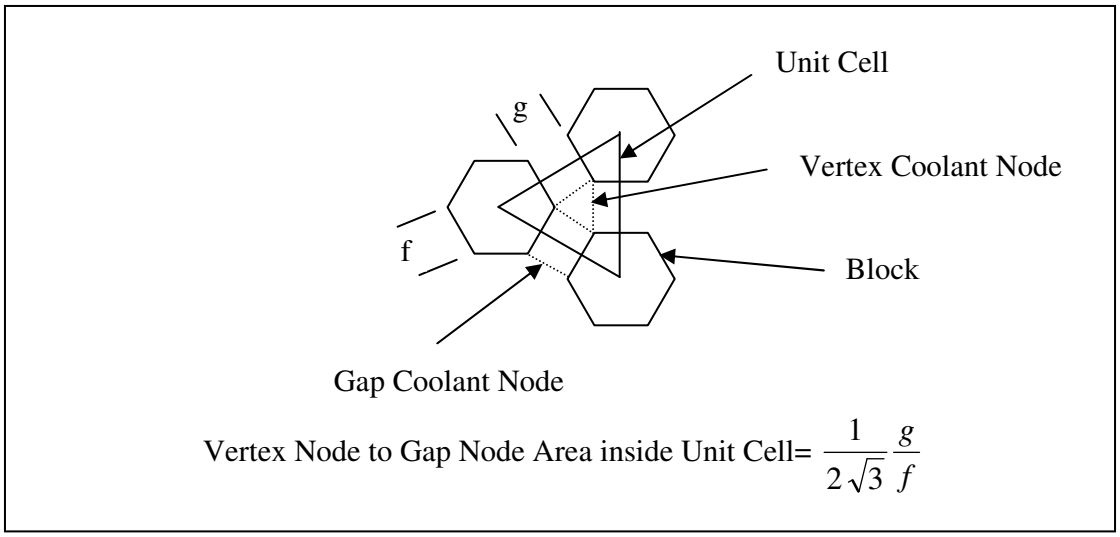

Fig. I.2 Coolant Nodes and Unit Cell

$$0 = P_{gap}^{\ l,k} - K_{lat}^{\ l,k}\ w_{gap-lat}^{\ l,k}\ |\, w_{gap-lat}^{\ l,k}\ |^{1-n} - P_{gap}^{\ l+1,k} \tag{I.4a}$$

where

$$K_{lat}^{\ l,k} = \frac{C\, L_{lat}^{\ l,k}}{2\rho\, D_{h-lat}^{\ l,k} (A_{lat}^{\ l,k})^2} \left(\frac{\mu\, A_{lat}^{\ l,k}}{D_{h-lat}^{\ l,k}} \right)^n ,$$

$$D_{h-lat}^{\ l,k} = \frac{4A_{lat}^{\ l,k}}{P_{w-lat}^{\ l,k}} ,$$

$$L_{lat} = 4f \tag{I.4b}$$

$$A_{lat}^{\ l,k} = L_{ax}\, g$$

$$P_{w-lat}^{\ l,k} = 2L_{ax}^{\ l,k}$$

where $A_{ax}^{\ l,k}$ and $P_{w\text{-}ax}^{\ l,k}$ are the crossectional area and wetted perimeter, respectively, of the participating coolant shown as the shaded region in Fig. I.3. Viewed from the side of the column, the particpating coolant is assumed to extend from the middle of the block at axial level *k* to the middle of block *k-1* where axial levels are defined in Fig. 5.10. The length of the channel, L_{lat}, is set equal to the number of block gaps that are passed in going from nodes $node_{gap}^{\ l,k}$ and $node_{gap}^{\ l+1,k}$. Figure I.3 shows this number to be four.

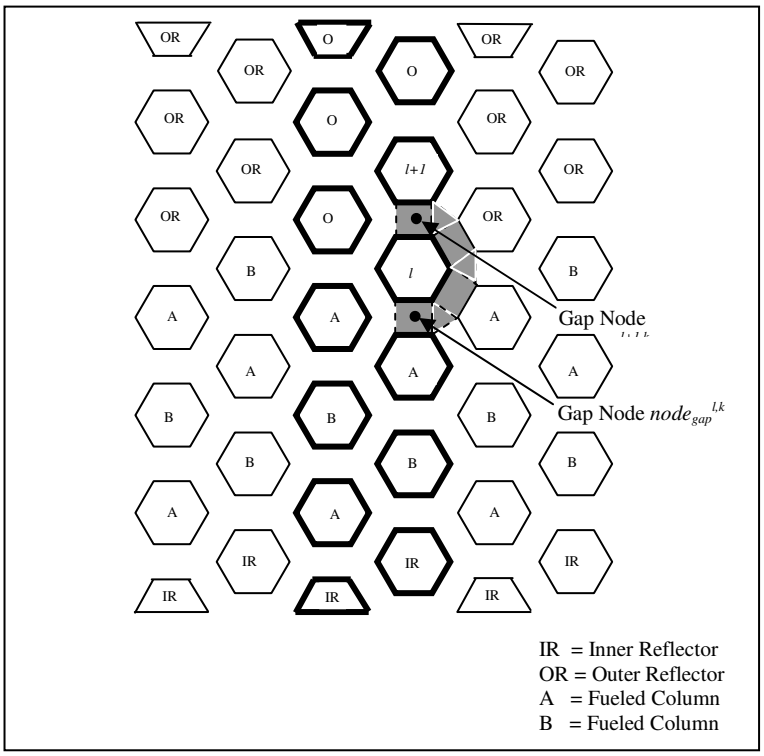

Fig. I.3 Coolant Participating in Lateral Momentum Balance between Gap Nodes $node_{gap}^{l,k}$ and $node_{gap}^{l+1,k}$. Coolant is shown as shaded region.

E. Block Interface Coolant Momentum Balance

A momentum balance for the horizontal interface between two stacked blocks is taken from the center of the blocks out to the periphery. Two momentum balances are written, one for that one-half of the interface area that is on the inboard side and the other for the interface area that is on the outboard side, respectively

$$0 = P_{chan}^{l,k} - K_{leak-in}^{l,k} w_{leak-in}^{l,k} * | w_{leak-in}^{l,k} |^{1-n} - P_{gap}^{l,k} \tag{I.5}$$

$$0 = P_{chan}^{l,k} - K_{leak-out}^{l,k} w_{leak-out}^{l,k} * | w_{leak-out}^{l,k} |^{1-n} - P_{gap}^{l+1,k} \tag{I.6}$$

We assume positive $w_{leak\text{-}in}^{l,k}$ and $w_{leak\text{-}out}^{l,k}$ represent flow from the center to the periphery.

In these expressions, the form the loss coefficients take depend on whether the gap is of uniform thickness as is the case where the blocks have not deformed or whether it is wedge-shaped as in the case where the blocks are deformed and inter-block forces cause the two stacked blocks to ride on a single edge. In the first case, the relation between flowrate and frictional pressure drop is given by Eq. (I.16) for two stacked

reflector elements with a control rod hole and by Eq. (I.18) for two stacked fuel elements for coolant channels adjacent the inter-column gap. In both cases n=1. In the second case, (i.e. deformed block) the relation between flowrate and frictional pressure drop is given by Eq. (I.22) and n=0. In the second case however, the leakage terms will exhibit a dependence on the orientation of the wedge. Generally, the neutron gradient changes most predominantly in the radial direction resulting in the assemblies to bow in the radial direction. In this case, the gap will tend to open up in one of two directions, either radially outward or radially inward. Obviously, the exact case will bear on the form Eqs. (I.5) and (I.6) assume.

F. Channel Coolant Axial Momentum Balance

For the coolant channels in a block the momentum balance for the variables in the network diagram of Fig. 5 is

$$0 = P_{chan}^{\,l,k} - K_{chan}^{\,l,k}\; w_{chan}^{\,l,k} \,|\, w_{chant}^{\,l,k} \,|^{1-n} - P_{chan}^{\,l,k+1} \tag{I.7a}$$

where

$$K_{chan}^{\,l,k} = \frac{C\, L_{chan}^{\,l,k}}{2\rho\, D_{h-chan}^{\,l,k} (A_{chan}^{\,l,k})^2} \left(\frac{\mu\, A_{chan}^{\,l,k}}{D_{h-chan}^{\,l,k}} \right)^n, \tag{I.7b}$$

$$D_{h-chan}^{\,l,k} = \frac{4 A_{chan}^{\,l,k}}{P_{w-chan}^{\,l,k}}$$

and where $D_{h\text{-}chan}$ is the diameter of the coolant channels in the block, $P_{w\text{-}chan}$ is the wetted perimeter of all the coolant channels in the block, A_{chan} the area of all the coolant channels in the block, and where

$$A_{chan}^{\,l,k} = n_{chan}^{\,l,k} (\pi/4) (D_{chan}^{\,l,k})^2$$
$$P_{w-chan}^{\,l,k} = n_{chan}^{\,l,k}\, \pi\, D_{chan}^{\,l,k}$$

where n_{chan} is the number of coolant holes per element and D_{chan} their diameter. When the multiple channel diameters exist, these last two equations are written as a sum of terms, one for each diameter.

G. Control Rod Hole Coolant Node Mass Balance

The control rod hole is situated in the interior of a block and runs its length. Coolant leaks into the hole from coolant holes that neighbor it. The leakage is assumed to occur through the interface between two stack blocks. Performing a mass balance on the flows into and out of this node shown in Fig. I.4 gives

$$0 = w_{cntrl}^{\,l,k-1} + w_{leak-cntrl}^{\,l,k} - w_{cntrl}^{\,l,k} \tag{I.8}$$

where *cntrl* refers to the control rod hole and *leak* refers to the coolant leaking from the coolant channel into the control rod hole. $w_{leak-cntrl}^{l,k}$ is assumed positive when flow is from the coolant hole to the control rod hole. Note that Fig. I.4 depicts the original unit network of Fig. 5.11 extended to include a control rod hole.

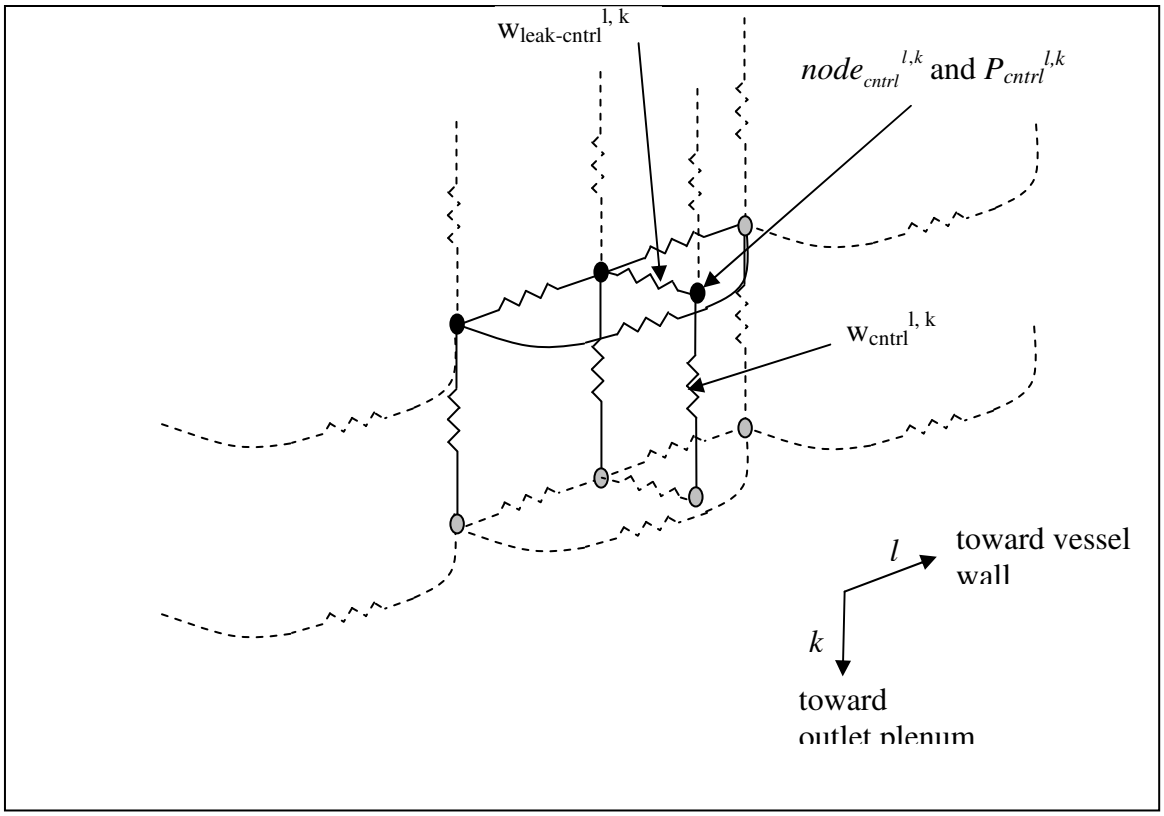

Fig. I.4 Network Representation of Mass Nodes, Coolants Flowpaths, and Pressures for Elements with Control Rod Holes. Consists of unit network representation with added path for coolant flow in control rod hole. Only those variables associated with control rod hole are shown. Variables not shown are those associated with unit network.

H. Block Interface Coolant Channel to Control Hole Coolant Momentum Balance

A momentum balance between the coolant channels adjacent the control rod hole gives

$$0 = P_{chan}^{l,k} - K_{leak-cntrl}^{l,k} w_{leak-cntrl}^{l,k} * | w_{leak-cntrl}^{l,k} |^{1-n} - P_{cntrl}^{l,k} \qquad \text{(I.9)}$$

where $K_{leak-cntrl}^{l,k}$ is the loss coefficient. The loss coefficient is given by Eq. (I.18) with n=1 in the above equation.

I. Control Rod Hole Coolant Axial Momentum Balance

For the control rod hole, the momentum balance for the variables in the network diagram of Fig. I.4 is

$$0 = P_{cntrl}^{\,l,k} - K_{cntrl}^{\,l,k}\, w_{cntrl}^{\,l,k} * |\, w_{cntrl}^{\,l,k}\,|^{1-n} - P_{cntrl}^{\,l,k+1} \tag{I.10a}$$

where

$$K_{cntrl}^{\,l,k} = \frac{C\, L_{cntrl}^{\,l,k}}{2\rho\, D_{cntrl}^{\,l,k} (A_{cntrl}^{\,l,k})^2} \left(\frac{\mu\, A_{cntrl}^{\,l,k}}{D_{cntrl}^{\,l,k}} \right)^n, \tag{I.10b}$$

D_{cntrl} = the diameter of the control rod hole in the block, and

A_{cntrl} = the area of the control rod hole in the block.

J. Outboard Gap Coolant Node Mass Balance

The outboard gap is situated on the outermost side of the last block. Performing a mass balance on the flows into and out of this node gives

$$0 = w_{gap-lat}^{\,ncol,k} + w_{leak-out}^{\,ncol,k} + w_{gap-ax}^{\,outbd,k-1} - w_{gap-ax}^{\,outbd,k} \tag{I.11}$$

where the subscripts have the same meaning as previously. The superscripts are as before except *ncol* which refers to the last column and *outbd* refers to the outboard gap.

K. Ouboard Gap Coolant Axial Momentum Balance

A momentum balance between two vertically adjacent mass nodes in the outboard gap gives

$$0 = P_{gap}^{\,outbd,k} - K_{gap-ax}^{\,outbd,k}\, w_{gap-ax}^{\,outbd,k}\, |\, w_{gap-ax}^{\,outbd,k}\,|^{1-n} - P_{gap}^{\,outbd,k+1} \tag{I.12}$$

where

$$K_{gap-ax}^{\,outbd,k} = \frac{C\, L_{ax}^{\,outbd,k}}{2\rho\, D_{gap-ax}^{\,outbd,k} (A_{gap-ax}^{\,outbd,k})^2} \left(\frac{\mu\, A_{gap-ax}^{\,outbd,k}}{D_{gap-ax}^{\,outbd,k}} \right),$$

$$D_{h-lat}^{\,outbd,k} = \frac{4 A_{ax}^{\,outbd,k}}{P_{w-ax}^{\,outbd,k}}$$

where $A_{gap\text{-}ax}^{outbd,k}$ and $P_{w\text{-}gap\text{-}ax}^{outbd,k}$ are the crossectional area and wetted perimeter, respectively, of the participating coolant.

I.2 Constitutive Equations

The relationship between mass flowrate and shear in the fluid near the wall of a channel is a key element in predicting the distribution of coolant. Expressions are developed for four geometries that appear in the core.

A. Channel Flow

A channel is a straight length enclosure through which coolant flows entering at an inlet and exiting at an outlet. A channel is taken to have a constant cross-sectional shape and area from inlet to outlet. In the GT-MHR, there are several flow paths that meet this description: the gap of rectangular cross section that extends axially between opposing faces of two blocks in adjacent columns, which we denote by *chan;* the gap of rectangular cross section that extends laterally between opposing faces of two blocks in adjacent columns, which we denote by *gap;* and the circular hole that extends axially the length of a block for insertion of a control rod, which we denote by *cntrl*.

In a channel of arbitrary cross section, frictional pressure drop is obtained from circular tube experiment data using the concept of dimensional similitude. One obtains the expression

$$0 = P_{in} - \frac{f\ L}{2\rho D_h A^2}\, w_{out} * \left| w_{out} \right| - P_{out}$$

relating mass flowrate and pressure drop through the hydraulic diameter D_h defined as $4*A/P_w$ where A is the crossectional flow area and P_w is the wetted perimeter and the friction factor

$$f = C\,\mathrm{Re}^{-n} \quad \text{where} \quad \mathrm{Re} = \frac{w\,D_h}{\mu\,A}$$

where C and n are constants and μ is viscosity. A loss coefficient is defined by collecting terms in the above two equations

$$K = \frac{CL}{2\rho DA^2}\left(\frac{\mu A}{D}\right)^n \tag{I.13}$$

so that

$$0 = P_{in} - K\ w_{out} * \left| w_{out} \right|^{1-n} - P_{out} \tag{I.14}$$

B. Leakage Between Parallel Disks

Reflector blocks are stacked vertically in columns creating an interface gap bewteen two stacked blocks. In the case of a reflector block with a control rod hole, there then is a leakage path between the interior hole and the inter-block gap at the exterior of the block through the interface gap. The flowrate through this gap is modeled assuming the following approximations. The reflector block is represented as a right-circular cyclinder having a radius of a circle with the same area as the hex face. The interior control rod hole is assumed to be centered in this circle. Then assuming the gap is small enough to produce laminar flow, [I.1] gives the flowrate as that between two parallel disks shown in Fig. I.5.

$$w = \frac{\pi}{6} \cdot \frac{\delta^3}{\upsilon} \cdot \frac{\Delta P}{\ln\left(\frac{r_o}{r_i}\right)}$$

where δ is the gap thickness and υ is the kinematic viscosity with the remaining symbols defined in Fig. I.5. Rewriting the above equation in terms of a flow resistance K we have

$$\Delta P = K\, w \tag{I.15}$$

where

$$K = \frac{6}{\pi} \cdot \frac{\upsilon}{\delta^3} \cdot \ln\left(\frac{r_o}{r_i}\right). \tag{I.16}$$

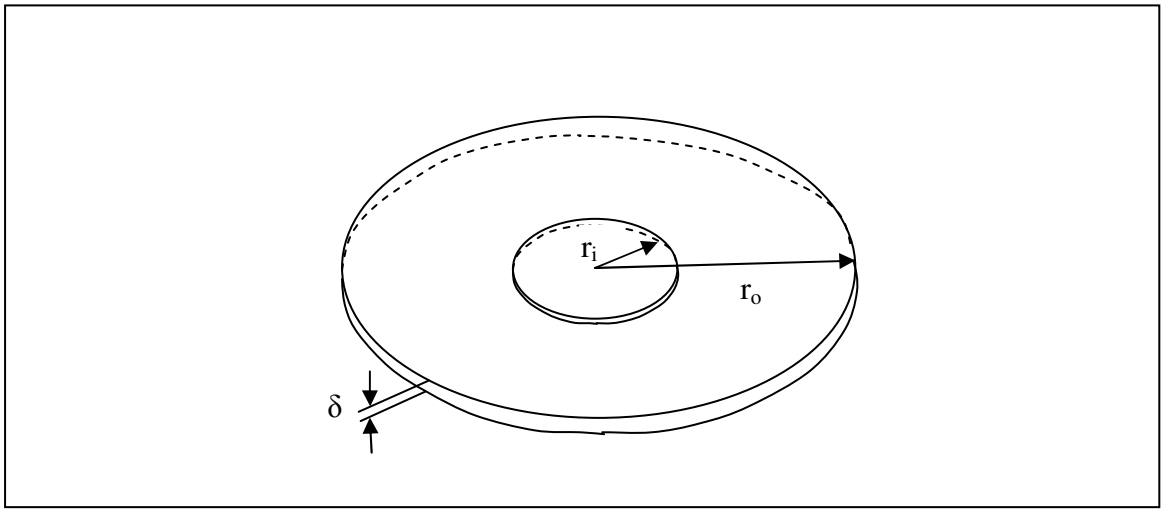

Fig. I.5 Geometry for Leakage between Parallel Plates

C. Leakage from Circular Channel Through Thin Gap

In the case where blocks have not undergone deformation, the gap between two stacked blocks is small. It has been shown that approximately 98 percent of the coolant

leaking from coolant channels and escaping through the gap between the blocks originates in the outermost peripheral channels.[I.1] To model this, consider two flat-faced blocks stacked one on top of the other and subject only to the force of gravity. The two blocks meet at an interface whose gap thickness is a function of surface asperities and the contact pressure. In the case where the gap thickness is a few micrometers, the flow of gas in the gap is laminar and can be solved for analytically. Kaburaki [I.1] gives the following relation for coolant mass flowrate and pressure drop for a circular channel near the periphery of these blocks as shown Fig. I.6.

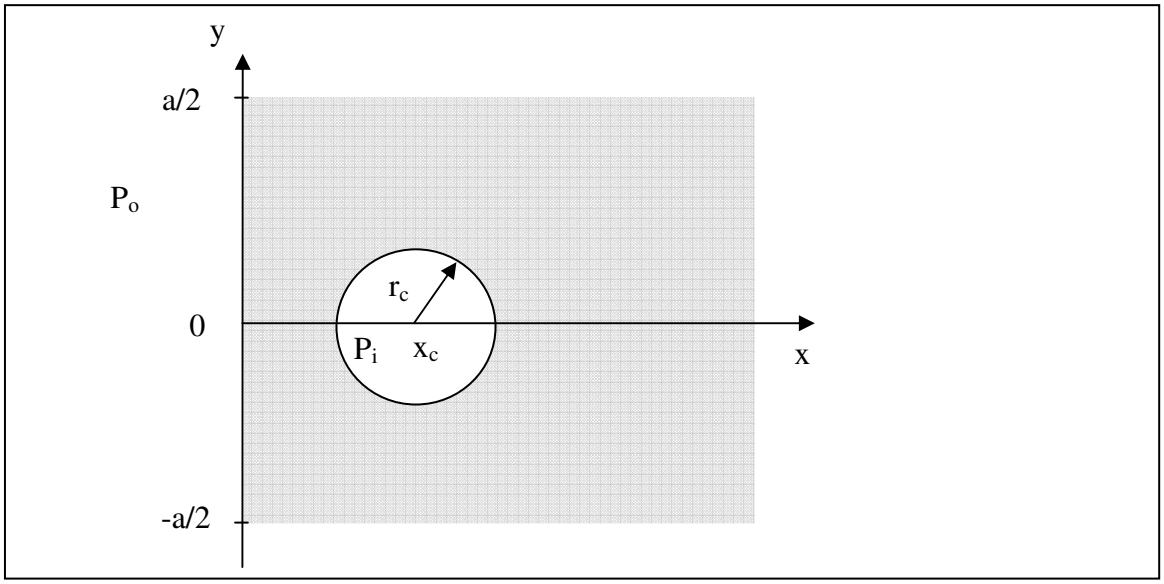

Fig. I.6 Geometry for Leakage from Circular Channel Through Thin Gap

$$w = -\frac{2}{3}\cdot\frac{\delta^3}{\upsilon}\cdot\frac{\tan^{-1}\left(\frac{a}{2\alpha}\right)}{\ln\left(\frac{x_c-\alpha}{x_c+\alpha}\right)}\,\Delta P$$

where x_c is the location of the center of the coolant channel, a is the length of the side of the periphery of the block through which the coolant flows, $\alpha = (x_c^2 - r_c^2)^{1/2}$, r_c is the radius of the coolant channel, δ is the gap thickness, and υ is kinematic viscosity. Rewriting the above equation in terms of a flow resistance K, we have

$$\Delta P = K\, w \tag{I.17}$$

where

$$K = -\frac{3}{2}\cdot\frac{\upsilon}{\delta^3}\cdot\frac{\ln\left(\frac{x_c-\alpha}{x_c+\alpha}\right)}{\tan^{-1}\left(\frac{a}{2\alpha}\right)}. \tag{I.18}$$

D. Leakage from Between Stacked Blocks Through Wedge-Shaped Gap

In the case where blocks have deformed and where their position in the core is constrained by neighboring blocks or the vessel wall, a wedge-shaped opening develops between stacked blocks. The leakage from such wedged-shaped gap was measured experimentally by Groehn [I.2] for prismatic fueled blocks representative of those in the GT-MHR. The blocks each contained 72 coolant channels, had a flat-to-flat width of 0.36 m, and a length of 0.8 m. In the experiments, the gap width was varied while the number of faces for which the gap was covered was varied from zero to five. The assumption is that the two blocks are in contact only along one of their six common edges. The *nominal gap size* is defined as the width of the gap on the opposite side of the blocks from where the two edges are contacting. Then in the experiment, if only this opening was left uncovered along the perimeter, the wedged-shaped gap is said to be covered along five faces (or along five-sixths of the block perimeter). If none of the openings along the faces were covered, then the gap is said to be uncovered along its entire perimeter (i.e five of the six faces have an opening).

A correlation relating pressure drop to coolant velocity, gap size, and the number of faces covered is developed in [I.2] from experiment data. The correlation is expressed in terms of an average velocity of the coolant in the gap defined as

$$u = u_{K0} - u_K \tag{I.19}$$

where u_K is the average velocity of the coolant in the upstream block and u_{K0} is the average velocity of the coolant in the downstream block. In the experiment $u_{K0} > u_K$ so flowrate was into the gap. The correlation is given as

$$\xi = \frac{\Delta P}{1/2 \rho u^2} = 3.58 \left(\frac{a}{D} \right)^{-2.3} 6.33 \left(\frac{A_{gap}}{a \cdot l} \right)^{-1.68} \tag{I.20}$$

where ρ is the coolant density, a is the nominal gap size, D is the coolant channel diameter, A_{gap} is the uncovered area along the perimeter of the wedge shaped gap, and l is the length along an edge of a block. Note that if none of the gap is covered then $A_{gap} = 3al$ in [I.2].

The above expression is rewritten in terms of gap mass flowrate. From Eq. (I.20)

$$\Delta P = \frac{1}{2} \xi \rho u^2 = \frac{1}{2} \xi \rho \left(u_{K0} - u_K \right)^2 = \frac{1}{2 \rho A^2} \xi \left(w_{K0} - w_K \right)^2 = K_B w^2 \tag{I.21}$$

where K_B is a loss coefficient defined by

$$K_B = \frac{1}{2 \rho A^2} \xi \tag{I.22}$$

and w is the mass flowrate through the gap and A is the cross sectional flow area of the coolant channels in the block.

I.3 Model Verification

Verification is the process of determining whether a computational model correctly implements the mathematical model of the physical process. The flow distribution code developed in this project is programmed in Compaq Visual Fortran. Two separate verification tests were performed, each involving the Base Case problem described above. The first test was performed to determine whether the programmed equations give a unique solution as they must if they have been correctly programmed. Uniqueness of solution is required on two levels. At the unit network level, Table I.1 indicates that the mathematical equations for a unit network imply a solution and that it should be unique. At the global network level, Table I.2 indicates that the mathematical equations for the collection of unit networks also imply a solution and it should be unique. The code did in fact compute a unique solution. Its uniqueness was verified by examining the rank of the Jacobian of the linearized system equations in the neighborhood of the solution. Since the system is square, a full rank Jacobian would indicate the solution found is unique. The Jacobian rank was found to be full and so the solution is unique.

The second verification test involved checking that the solution found by the Fortran code satisfies the equations that are to be solved, in this case Eqs. (I.1) through (I.12). These equations were programmed separately and independently in MATLAB. If the equations programmed in MATLAB are satisfied when the Fortran code solution is substituted in, then it is concluded the Fortran code has implemented the equations correctly. Note that the global solution to the flow allocation problem is composed of the simultaneous solution to each unit network. Thus, if the Fortran code solution when substituted into each of the unit networks as represented by the MATLAB program equations, then it can be concluded that the Fortran code correctly implements Eqs. (I.1) through (I.12). The hydraulic conditions represented by the converged Fortran code solution did in fact satisfy the MATLAB program equations indicating the equations in the Fortran code have been correctly programmed.

Table I.1 Uniqueness of Solution for Unit Flow Network: Inventory of Number of Variables, Equations, and Boundary Conditions

# of Boundary Conditions	+	# of Equations	=	# of Variables
6		7		13
	$P_{gap}^{l,k}$, $P_{chan}^{l,k}$, $P_{gap}^{l+1,k}$ $P_{gap}^{l,k+1}$, $P_{chan}^{l,k+1}$ $w_{gap\text{-}lat}^{l-1,k}$	1 - channel coolant node mass balance @ level k, Eq. (11) 1 - gap coolant node mass balance @ level k, Eq. (12) 1 – gap coolant axial momentum balance @ level k, Eq. (13) 1 - gap coolant lateral momentum balance @ level k, Eq. (14) 2 – block interface coolant momentum balance @ level k, Eqs. (15) and (16) 1 – channel coolant axial momentum balance @ level k, Eq. (17)		$w_{gap\text{-}ax}^{l,k-1}$, $w_{chan}^{l,k-1}$ $w_{leak\text{-}in}^{l,k}$, $w_{leak\text{-}out}^{l,k}$, $w_{gap\text{-}lat}^{l,k}$ $w_{gap\text{-}ax}^{l,k}$, $w_{chan}^{l,k}$, boundary condition variables

Table I.2 Uniqueness of Solution for Flow Network: Inventory of Number of Variables, Equations, and Boundary Conditions

# of Boundary Conditions	+	# of Equations	=	# of Variables [a]
Pressure at top of columns $2*n_{col}$ (i.e. $P_{gap}^{l,1}$, $P_{chan}^{l,1}$) 1 (i.e. $P_{gap}^{ncol,1}$) pressure at bottom of columns $2*n_{col}$ (i.e. $P_{gap}^{l,nlev+1}$, $P_{chan}^{l,nlev+1}$) 1 (i.e. $P_{gap}^{ncol+1,nlev+1}$) lateral flow into inner face of first column 0 [b] lateral flows at bottom of columns 0 [c]		unit network $7*n_{col}*n_{lev}$ mass balance in outboard gaps n_{lev} pressure drop in outboard gaps n_{lev}		flow into top of columns $2*n_{col}$ (i.e. $w_{gap\text{-}ax}^{l,0}$, $w_{chan}^{l,0}$) flow into top outboard gap 1 (i.e. $w_{gap\text{-}ax}^{ncol+1,0}$) unit networks $7*n_{col}*n_{lev}$ (i.e. $P_{gap}^{l,k}$, $P_{chan}^{l,k}$, $w_{leak\text{-}in}^{l,k}$, $w_{leak\text{-}out}^{l,k}$, $w_{gap\text{-}lat}^{l,k}$, $w_{gap\text{-}ax}^{l,k}$, $w_{chan}^{l,k}$) flow and pressure in outboard gaps n_{lev} (i.e. $w_{gap\text{-}ax}^{ncol+1,k}$) n_{lev} (i.e. $P_{gap}^{ncol+1,k}$) lateral flow into inner face of first column 0 [b] pressure at bottom of columns $2*n_{col}$ (i.e. $P_{gap}^{l,nlev+1}$, $P_{chan}^{l,nlev+1}$) pressure at bottom outboard gap 1 (i.e. $P_{gap}^{ncol+1,nlev+1}$) lateral flows at bottom of columns 0 [c]

[a] Unit cells are indexed l = 1,… ncol and k = 1, … nlev. For variables not in unit cells indices are l = 0, ncol+1 and k = 0, nlev+1.
[b] Assume lateral flow develops only within interior of modeled columns.
[c] Bottom unit cells serve soley to set core outlet boundary conditions; lateral flow assumed zero

References

I.1 H. Kaburaki, “Leakage Flows in High-Temperature of Seal Mechanism for HTGR Core Support Blocks”, Journal of Nuclear Science and Technology, n9, p 742-747, Sep 1987. (support_block_leaks.pdf)

I.2 H. G. Groehn, “Estimate of Cross Flow in High Temperature Gas-Cooled Reactor Fuel Blocks”, Nuclear Technology, vol 56, Feb 1982.

Nuclear Engineering Division
Argonne National Laboratory
9700 South Cass Avenue, Bldg. 208
Argonne, IL 60439-4842

www.anl.gov

A U.S. Department of Energy laboratory managed by UChicago Argonne, LLC